Title	Improving the mechanical properties of the In52Sn48 alloy by adding third elements
Author(s)	Han Le, Duy
Citation	大阪大学, 2022, 博士論文
Version Type	VoR
URL	https://doi.org/10.18910/88045
rights	
Note	

Doctoral Dissertation

Improving the mechanical properties of the In52Sn48 alloy by adding third elements

HAN LE DUY

December 2021

Graduate School of Engineering

Osaka University

Supervisor

Professor Hiroshi Nishikawa

Department of manufacturing process, Joining and Welding Research Institute

Osaka University

Doctoral Committee

Professor Hiroshi Nishikawa

Department of manufacturing process, Joining and Welding Research Institute

Osaka University

Professor Fukumoto Shinji

Division of Materials and Manufacturing Science, Graduate School of Engineering

Osaka University

Associate Professor Iwata Yoshiharu

Division of Materials and Manufacturing Science, Graduate School of Engineering

Osaka University

Contents

List of Figures

List of Tables

Abbreviations

IoT	Internet of Things
CTE	Coefficient of thermal expansions
OLED	Organic Light-Emitting Diode
R2R	Roll-to-roll
PET	Polyethylene terephthalate
PEN	Polyethylene naphthalate
PC	Polycarbonate
PES	Polyethersulfone
PI	Polyimide
PAR	Polyarylates
PCO	Polycyclic olefin
ITO	Indium tin oxide
FPCB	Flexible printed circuit board
PWA	Printed-wiring assemblies
NCA	Nonconductive adhesive
ACA	Anisotropic conductive adhesive
ICA	Isotropic conductive adhesive
ECA	Electrically conductive adhesive
ECT	Electrically conductive tapes
SMD	Surface-mounted devices
PCB	Printed circuit board
SMT	Surface mount technology

PTH	Plated-through holes
P-QFP	Plastic encapsulated quad-flat packs
TSOP	Thin small outline packages
I/O	Input/ Output
BGA	Ball-grid arrays
CSP	Chip-scale package
KGD	Known good die
DCA	Direct chip attach
IC	Integrated circuits
3D	Three dimensional
TSV	Through-silicon-vias
WEEE	Waste Electrical and Electronic Equipment
RoHS	Restriction of Hazardous Substances
UTS	Ultimate tensile strength
EL	Elongation
T_m	Melting temperature
T_h	Homologous temperature
T_g	Glass transition temperature
H_μ	Microhardness
β	In_3Sn
γ	$InSn_4$
η	$Cu_6(In,Sn)_5$
τ	$Cu(In,Sn)_2$
IMC	Intermetallic Compound

PoP	Package on package
JIS	Japanese Industrial Standards
AWS	American Welding Society
SAC	Sn-Ag-Cu
BSA	Bi-Sn-Ag
IS48	In52Sn48
ISA	In-Sn-Ag
ISC	In-Sn-Cu
ISA4805	In52Sn48-0.5Ag
ISA4810	In52Sn48-1.0Ag
ISA4815	In52Sn48-1.5Ag
ISC481	In52Sn48-1.0Cu
ISC482	In52Sn48-2.0Cu
ISC488	In52Sn48-8.0Cu
SEM	Scanning electron microscopy
BSE	Backscattered Electrons
ICP	Inductively coupled plasma
DSC	Differential scanning calorimetry
EDS/ EDX	Energy dispersive X-ray spectroscopy
EPMA	Field-emission electron-probe microanalysis
XRD	X-ray diffractometry
LCIA	Life-cycle impact assessment

Chapter 1

Research background

1.1 Flexible electronic devices

1.1.1 Introduction

The era of the internet of things (IoT) emerged with the advent of wearable and implantable technologies. Electronic devices are developing and becoming increasingly popular in almost all fields of life. Flexible electronic devices are integrated into and on the human body for a variety of purposes, from communication, to health monitoring and treatment [1]. Flexible electronics are a class of electronic devices that are fabricated on bendable or stretchable substrates, such as plastic, synthetic materials, and thin metal foil [2,3]. Devices such as rollable displays, e-paper, smart flexible sensors, health monitoring devices, and implantable devices, have recently attracted a lot of attention owing to their low cost of manufacturing and inexpensive flexible substrates [4,5]. Given these advantages, flexible electronics are regarded as a future trend in the development of next-generation electronic devices that require lightweight, bendable, portable, and cost-efficient solutions [3,5,6]. In addition, flexible hybrid electronics fabricated by integrating surface-mounted components onto/into printed stretchable conductive circuits and flexible substrates, also have the potential to revolutionise the electronic assemblies used for large-area applications, such as wearable devices and automotive, medical, and aerospace components [7,8].

Flexible electronics have a long history. The first flexible devices were solar cell arrays made in the 1960s on a plastic substrate using thin, single-crystal silicon wafer cells (∼100 μm) [9]. Since then, scientists have sought to improve technology and materials; the timeline of the development and application of flexible electronics is shown in **Figure 1.1** [3]. Future electronic systems need better mechanical integrity and electrical connectivity between electrical components and substrates to fulfil the requirements of markets for multiform application [3,4]. Recently, many researchers have paid attention to the development of new materials [10-12] and manufacturing technologies [13–15] to fabricate high-performance flexible electronic devices. While there have been significant advances in research, many challenges need to be overcome before flexible devices can be used widely in practice. Thus, there is an opportunity for researchers to continue to develop and improve technology and materials in this field [3].
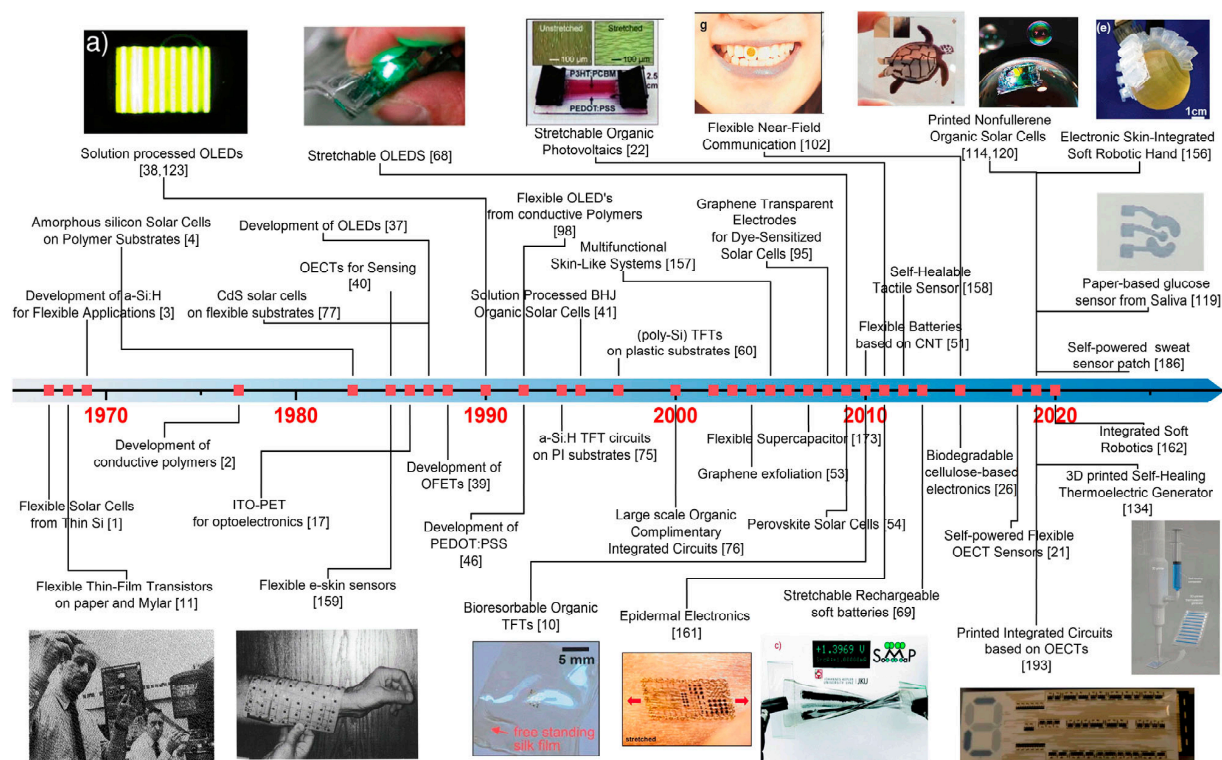
Figure 1.1 Timeline of developments in materials, processing and application for flexible electronics [3].

In this chapter, the materials used for flexible devices and packaging technologies are discussed. The technological challenges that need to be solved are also described, and solutions are discussed in this thesis.

1.1.2 Substrate materials

The biggest difference between flexible electronic devices and conventional electronic devices are the advantages offered by the substrate material; low cost, stretchable, and flexible. However, the substrate material also needs to have appropriate physical and mechanical properties so that it is not damaged during either manufacture or operation. The construction of flexible electronic devices includes at least four main parts: flexible substrates, backplane electronics, frontplane, and encapsulation (**Figure 1.2**) [9]. To make the structure flexible, the adhesive layer used to link the parts must have sufficient mechanical strength, must be flexible, and also temperature and chemically stable [2].
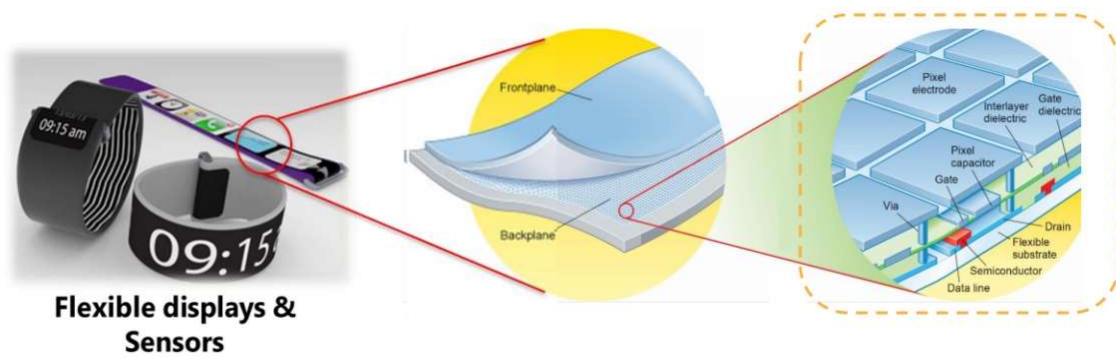
Figure 1.2 Schematically typical design of flexible display & sensors [16].

However, the selection of an adhesive must take into account the manufacturing process and materials. Thus, understanding the material properties of the flexible substrate will help provide technological solutions and enable the best coupling material to be selected. Below are the main properties that flexible substrates need to possess in order to replace rigid glass substrates [9,10,17,18]:

- Mechanical properties: A highly elastic modulus and hard-surface substrate are desired to support the device layers under impact.

- Thermal properties: Dimensional stability and a low coefficient of thermal expansion (CTE) are important factors. The working temperature is also a concern with plastic substrates. The glass transition temperature (T_g) of a flexible substrate must be compatible with the maximum processing temperature (T_{max}) to avoid thermal damage of the substrate during fabrication. Polymer substrates with a CTE below 20 ppm/°C are preferred as substrates for silicon-based device materials.

- Optical transmission properties: Sufficient optical transparency and low birefringence are the most important indicators of substrates for advanced optoelectronic devices.

- Surface quality: The absence of surface roughness is beneficial for the substrate of the thin-film devices (such as display backplanes, OLED lighting, and photovoltaic systems); with thinner film, the more sensitive the electrical function is to surface roughness.

Generally, the substrate materials used for flexible electronic devices can be divided into three main groups: thin glass foils, metal foils, and organic polymer (plastics) foils. Different applications may emphasise flexibility, high transparency, surface smoothness, low thermal expansion, low cost, thinness, or light weight. Therefore, the selection of the substrate material will depend on the specific technical requirements and the scope of the application. The first group, thin glass foil, with a thickness under 100 μm, is a candidate flexible substrate for some applications (e.g., displays, touch sensors, photovoltaic systems, and lighting). The advantages of thin glass foil include low-stress birefringence, high optical transmittance (>90% in the visible), smooth surface, and high dimensional stability [9,17,19]. However, flexible glass is fragile and difficult to handle, limiting its application as a flexible substrate. The metal foil group, with a thickness of less than ~125 μm, is attractive for emissive or reflective displays, which do not need transparent substrates. For example, stainless steel foil is commonly used in amorphous silicon solar cells owing to its excellent conductivity and high corrosion resistance. The plastics foil group is extremely attractive, given that it is lightweight, inexpensive, and permits roll-to-roll (R2R) processing. Plastic foils can be made with glass-like transparency, an essential property required for photovoltaic applications or display devices where light has to either enter or exit the device. Moreover, these polymer foils have a high degree of mechanical flexibility and conformability. Therefore, thin plastic substrates are being studied and increasingly used in flexible electronic devices [5,20,21]. A summary of the advantages and disadvantages of the three groups of flexible substrates is given in **Table 1.1** [22].

To date, many commercial polymer foils have been used as flexible substrates, including thermoplastic semicrystalline polymers (e.g., heat-stabilised polyethylene terephthalate (PET) and heat-stabilised polyethylene naphthalate (PEN)); thermoplastic non-crystalline polymers (e.g., polycarbonate (PC) and polyethersulfone (PES)); and high-T_g polymers (e.g., polyarylates (PAR), polycyclic olefin (PCO), and polyimide (PI)). Of these polymer foils, PI, PET, and PEN have been the subject of most research because of their comparatively low CTE (16, 15, and 13 ppm/ºC, respectively), relatively high elastic moduli, and acceptable resistance to process chemicals.

Table 1.1 Advantages and disadvantages of the three groups of flexible substrate [22].

Flexible substrate	Advantages	Disadvantages
Plastic/ polymeric foil	Rugged Bendable, rollable Transparent	Poor dimension stability Low process temperature High H_2O and O_2 permeation Low chemical resistance
Glass foil	Conformable Transparent Low H_2O and O_2 permeation	Low mechanical stability Low process temperature
Metal foil	Rugged, conformable Low H_2O and O_2 permeation High process temperature Good dimension stability	Opaque Rough surface Capacitive effect

Although PI has a high glass transition temperature of approximately 250°C, it is yellow because it absorbs blue light, and it also absorbs as much as 1.8% moisture. The drawbacks of the yellow colour and poor processability seriously limit application in the modern optoelectronics field, especially in flexible electronic devices and display technology [23]. In contrast, both PET and PEN are optically clear (transmittance of > 85% in the visible spectrum) and absorb relatively little water (~0.14%). Moreover, they provide good resistance to solvents and a tolerance to temperature. Also, their transparency when coated with indium tin oxide (ITO) make them suitable for optoelectronics, which require the transmission of light and electrical conductivity. Therefore, PET and PEN are becoming the two main transparent flexible substrates used today for the development of flexible electronics. The properties of some popular flexible substrates are shown in **Table 1.2** [19,21,24].

1.2   Interconnection technology in flexible electronic packaging

1.2.1 Introduction

To produce flexible devices simply and efficiently, and to meet the needs of different markets, production technologies must be accessible, easy to use, and inexpensive.

Table 1.2 Properties of substrates for flexible backplanes [19,21,24,25].

Property	Unit	Glass	Heat stabilized PET (Melinex ST506)	Heat stabilized PEN (Teonex Q65FA)	PI (Kinel)	Stainless steel
CTE ($\times 10^{-6}$)	K^{-1}	4	10	13	17-44	18
Transparency	%	90	91	85	yellow	None
Young modulus	GPa	70	2-4	5-5.5	2-3	190-210
Tensile strength	MPa	-	207	138	231	505
Glass transition temperature	°C	140-370	80-110	120-155	250	-
Upper working temperature	°C	600	115–170	155-180	250-320	1000
Melting temperature	°C	1400-1600	255	270	375 - 401	1400-1450

While conventional electronics are batch fabricated through film deposition and nanofabrication, including photolithography and etching, flexible electronics are often incorporated by pattern transfer, solution printing processes, R2R capabilities, and additive manufacturing technologies [3]. **Figure 1.3** is an example of a flexible printed circuit board (FPCB) process using an R2R gravure printing system [25]. The flexible aspect of flexible electronics is not only about the workability of the substrate material, but also about the bonding strength as well as the ability to transmit electrical signals between the components and the substrate material. To make the structure flexible, all parts need to be able to bend to some degree without losing their function [20]. Interconnection technologies for flexible electronics focusing on foil-based flexible systems are referred to as a system-in-foil (SiF).
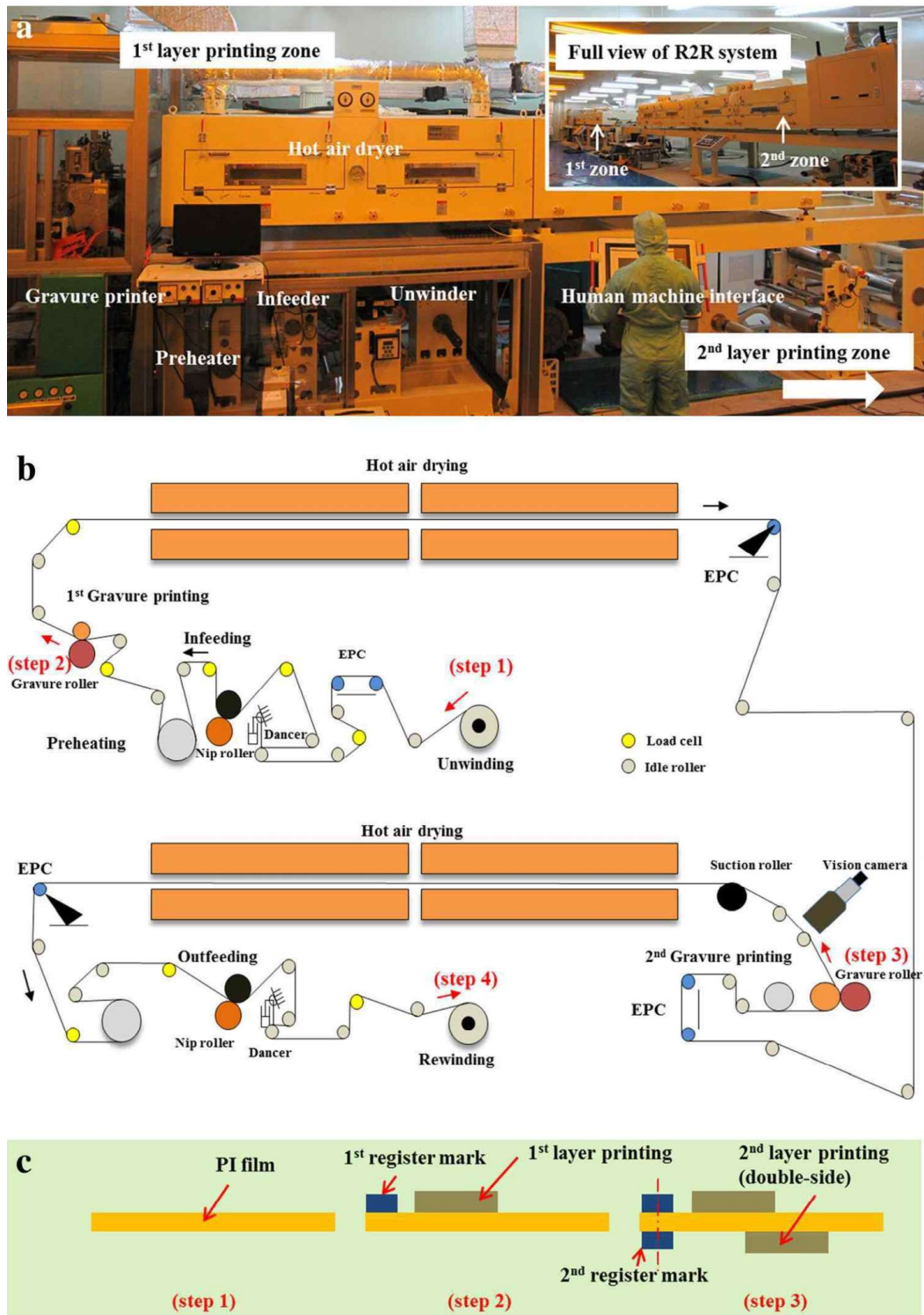
Figure 1.3 Flexible printed circuit board process using R2R gravure printing system; (a) industrial-scale R2R gravure printing module, (b) schematic diagram of the R2R system, (c) cross-sectional view of the FPCB at each position in (b) [26].

SiF is a composite structure comprising substrates, components and electrical interconnections that are mechanically and electrically networked to each other, as shown in **Figure 1.4** [18]. To bond the electronic components and parts, metallurgical solder, eutectic alloys, or organic polymer adhesives may be used. Below is a brief introduction to the main advantages and disadvantages of two common bonding methods for flexible electronics: the use of adhesives, and soldering.

1.2.2 Adhesives

Adhesives are widely used in the mass production of electronic hardware, including for the assembly and packaging of electronic devices, such as semiconductor dies, single-chip packages, and multi-chip assemblies. Adhesives come in paste form, as well as in film for high-density laminated bonding substrates, flexible circuits, and a host of other new applications including optoelectronics, flexible sensors, and smart cards. The advantages of adhesives are their low cost, ease of rework, and low processing temperature. As a result, polymeric adhesives have replaced many traditional connection materials, such as solder, eutectic alloys, and wires in most commercial consumer electronics [27]. Adhesion serves four main functions in the assembly of electronic circuits: mechanically attaching parts (such as semiconductor dies, components, substrates, packages, and heat sinks); electrically interconnecting components on a substrate or in a package; dissipating heat from components and circuits; and dissipating stress.
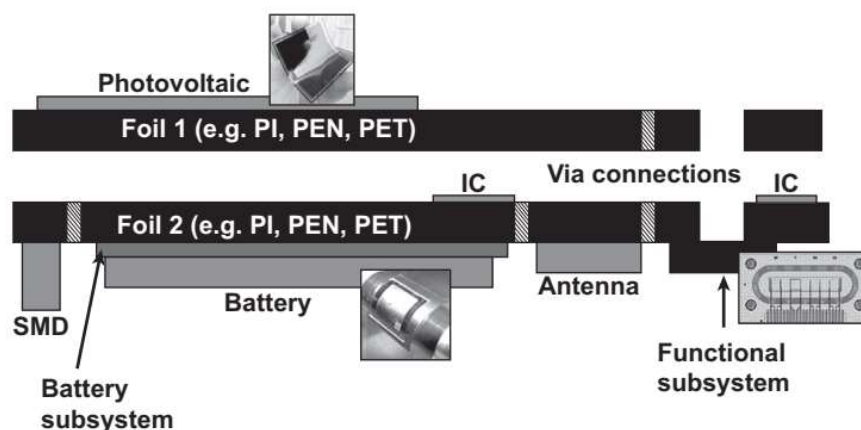
Figure 1.4 Schematic representation of a system-in-foil structure comprising various of components and sub systems [18].

In flexible electronics, flex circuits are used, which are analogous to rigid printed circuit boards except that they are fabricated from a thin flexible dielectric film to which a thin copper foil is bonded by adhesive. The copper is then optically treated to form a circuit pattern using a conventional photolithography process. A plastic film (or coverlay) is then adhesively bonded to the etched copper circuit, except for open areas that are left in order to attach components later. The coverlay protects against moisture and contaminants and acts as a protective coating to printed wire assemblies (PWAs). The most widely used dielectric films are made from PI or PET/PEN. A wide variety of adhesives can also be used, including acrylics, epoxides, and epoxides modified with plastics such as phenolic butyral. Adhesives for flex circuits must meet several requirements, including [27]:

- Maintain adhesion while the circuit is flexed
- Have good wetting and bonding on both polymer film and copper foil
- Have low moisture absorption
- Have good dielectric properties
- Have low or no-flow characteristics
- Be thermally resistant to solder-reflow temperatures

Nonconductive adhesive (NCA), anisotropic conductive adhesive (ACA), and isotropic conductive adhesive (ICA) are among the most common adhesive application processes. Adhesive (such as NCA) is applied in paste or film form on the substrate or wafer using conventional delivery, screen/jet printing or lamination. **Figure 1.5** shows electrical interconnections formed by jetting ICA between a foil component and the system foil. This process involves the simultaneous application of pressure and temperature by a die bonder, and the applied pressure ensures contact between pillars/bumps on the chip bonding pads and the foil pad. Application heat, usually provided by the die bonder or ultraviolet (UV) radiation applied across the substrate, cures the adhesive during chip assembly. Shrinkage of the NCA provides mechanical integrity to the assembly, maintaining electrical connections by compressing force reaching resistance values comparable to soldered contacts.
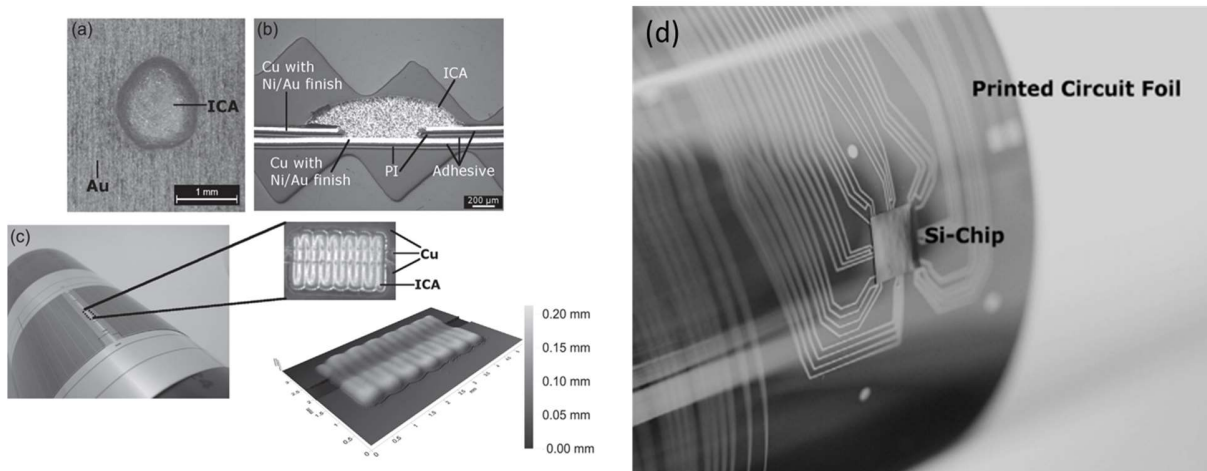
Figure 1.5 Electrical interconnections formed by jetted isotropic conductive adhesive (ICA) between a foil component and the system foil. (a) Top; (b) cross-sectional view of a via-filling; and (c) top view of mounted flexible PV cells (left) and microscopic view & 3-D topography of an isotropic conductive adhesive (ICA) bridge. (d) 20 mm thick Si-chip (5x5 mm^2) mounted on a 50 mm polyimide (PI) printed circuit foil in a nonconductive adhesive (NCA) flip chip process and bent to 30 mm bending radius [18,20]

However, the shrinkage of NCA during curing has to withstand elastic deformation in the system and possible expansion of the adhesive due to moisture uptake in the field. Extensive care must be taken to prevent NCA contact with tools, especially in the case of very small die sizes. The temperature and duration of this process provide a high throughput based on materials that cure within seconds (quick-curing) at moderate temperatures, allowing less expensive substrates to be used [20]. Adhesive and bonding materials need to meet certain expectations regarding electrical bonding as well as chemical and mechanical resistance. Interconnections are typically subjected to bending and other types of deformation during temperature and humidity cycles in the manufacturing processes, as well as during storage and service. For these reasons, the connecting materials must also be sturdy and at the same time compatible with the primary raw materials used. However, to date, no commercially available electrically conductive adhesive (ECA) or tape (ECT) has been found that can replace Sn-based alloys in all applications. Some challenges need to be overcome: lower electrical conductivity; fatigue conductivity in reliability tests, such as decreased conductivity at elevated temperature and humidity with ageing or in normal use conditions; limited current-carrying capability; and poor impact strength. Therefore, electronic chips,

bar dies, and surface-mounted devices (SMDs), are assembled using both Sn-based soldering and adhesive bonding. However, to prevent the integrity of bonding pads from being harmed by flux residues and oxidation, the attachment of the SMDs by soldering involves additional steps for cleaning and protection. The use of conductive adhesives for chip mounting results in the lowest possible number of process steps on the production line [18].

1.2.3 Soldering

According to the American Welding Society (AWS) A3.0 Standard, soldering is a group of joining processes that produce coalescence of materials by heating them to the soldering temperature and by using a filler metal with a liquidus temperature not exceeding 450°C (840°F) and below the solidus temperature of the base metals. The filler metal (solder) is distributed between closely fitted faying surfaces of the joint by capillary action or by wetting the surfaces of the workpieces.

In electronic packaging, the performance and quality of the solder are crucial to the integrity of the alloy joint, which in turn is vital to the overall functioning of the assembly [28]. When thin devices are attached to flexible substrates, the interconnects need to be compliant to be able to accommodate the differential displacement due to CTE mismatch or to facilitate stretching, twisting, or bending of the flexible substrates. Integration has two components: mechanical integrity, and electrical connection. While the latter ensures signal transmission through electrical interconnections, mechanical integrity is the basis for the reliability and integration of the electronic system into its physical environment [20]. The interconnection technology of conventional printed circuit boards (PCB) is mostly based on soldering, including surface mount technology (SMT) and through-hole technology (THT) processes [20,29]. **Figure 1.6** shows the evolution of packaging technology from the solder joint perspective and schematics of alloy joints in single-chip and multichip packaging [29,30]. Leaded components with pin-in-hole joints dominated assembly technology for many years until the emergence of SMT in the mid-1970s. SMT is now widely used in a wide variety of applications because of the ease of automated assembly and machine soldering by the wave soldering process, providing a means of reducing the

size of the PCB. SMT has the advantage of using smaller components, thus allowing an increase in lead quantity in semiconductor devices. SMT also eliminates the PCB regions necessary for inserting lead components into plated holes (PTHs). Moreover, surface-mounted devices, including plastic encapsulated quad-flat packs (P-QFP) and thin small-outline packages (TSOP), are among the lowest cost and widely used semiconductor packages [30]. The need for improved performance, higher I/O, and size reduction, especially in flexible electronic devices, has resulted in the emergence of area-array packages. Ball-grid arrays (BGA) are in widespread use, and their smaller counterparts, chip-scale packages (CSP) are being introduced for use in many types of assemblies. In the 2020s, flip-chips are likely to emerge as a dominant architecture, as they solve the problems with handling bare semiconductors by standardisation to achieve the goal of the *known good die* – KGD (Tsukada, 1999). KGDs are defect-free semiconductors or chips, unpackaged and ready for assembly. Encapsulation and packaging technology has evolved with the development of semiconductor technology in both memory and microprocessors. Specifically, chip size has increased steadily, and clock speed and transistor density on the chip have also increased significantly. Flip-chip components are directly attached to the printed wiring board; direct chip attach (DCA) is the most advanced joint configuration, as shown in **Figure 1.6**.
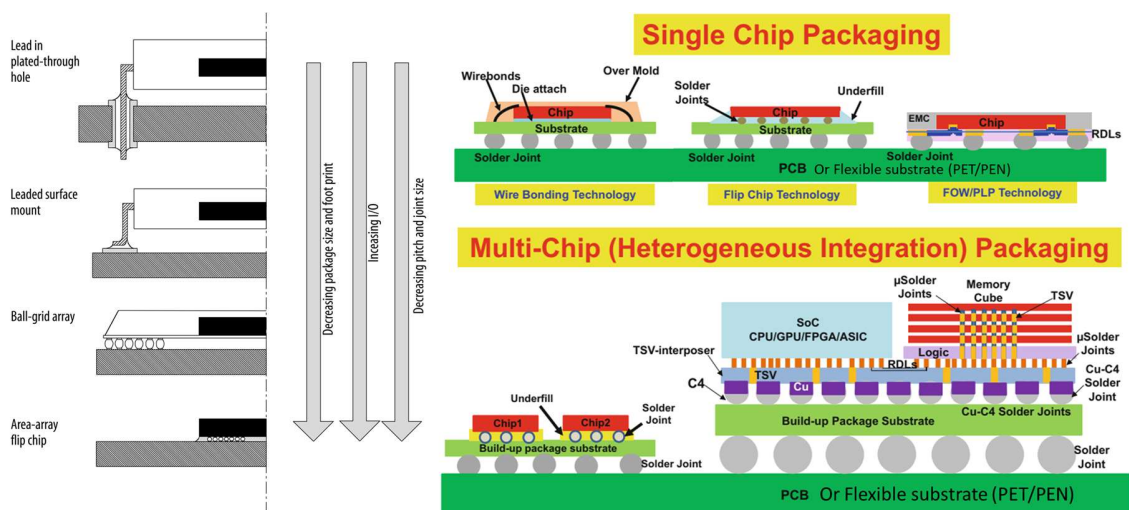
Figure 1.6 A schematic of the evolution of the alloy joint in relation to packaging architecture for semiconductor components (left), and schematic of alloy joints in single chip and multichip packaging (right) [29,30].

Packaged flip-chips have been used in many specialised cases by major electronics firms. DCA and/or encapsulation/packaging will become the main interconnection technology in the industry in general, as wire bonding reaches the I/O supply limits required for advanced chips [30]. Packaged SMD has been successfully integrated onto PI foils, and the high cost of the PI foils can be offset by the flexibility of the device being compatible with the soldering process. Foil-based technology with integrated circuits and auxiliary electronics integrated directly onto/into flexible substrates, such as PI and inexpensive PET/PEN foils, can be used for organic/inorganic (ultra-thin) components. This technology is still in its infancy, but foil-based technologies will significantly increase packaging density and provide decisive advantages over traditional PCBs for certain applications [20]. Adhesives and soldering have advantages and disadvantages; a comparison of metallurgical soldering and polymeric adhesive methods is given in **Table 1.3**. Changes in technology will place greater demands on the mechanical performance of alloy joints and, in turn, will generate the need of joint designs and manufacturing processes, as new architectures and alloy systems emerge in the market. The next section provides an overview of lead-free solder in electronic packaging.

1.3   Lead-free solder in electronic packaging

1.3.1 Lead-free alloys

In electronic packaging, solder alloys are the most important joining materials in different stages of the electronic assembly sequence and interconnection of the silicon chip (or die). Alloy not only contributes to the mechanical properties of the connection, but also helps transmit electrical signals between parts. For many years, tin-lead (SnPb) alloys were the most widely used solders in electronic assemblies, for applications ranging from consumer products to space communications systems [30]. However, Pb is a toxic element and has adverse effects on the environment. Therefore, in the early 1990s, a series of regulations were proposed to ban the use of lead in electronic applications. Subsequently, the European Union directives on Waste Electrical and Electronic Equipment (WEEE) and Restriction of Hazardous Substances (RoHS) dictated that consumer electronics sold in the EU must be Pb-free from July 1, 2006.

Table 1.3 Comparison of metallurgical soldering and polymeric adhesive methods [27].

Interconnection method	Advantages	Disadvantages
Soldering	• Batch process • Automated dispensing or screen-printing • Long history of use/ mature • Easy rework • Good electrical connections • Good thermal conduction	• Requires flux • Risk of flux residues and corrosion • Corrosion of solder in humidity, if not over coated. • Risk of voids under large components • Stress due to large CTE mismatches • High-temperature exposure during reflow (conventional 200-240 ˚C) • Limited wetting and adhesion to some surface
Adhesive	• Easy rework • Low cost • Low-processing temperature (< 165 ˚C) • Automated dispensing or screen-printing • Wide variety of commercially available products to choose from • Ability to relieve stresses • Excellent adhesion to most surfaces • Snap-cure types cure in seconds (120-160 ˚C) • Directional conductivity with anisotropic forms	• Risk of outgassing in enclosed packages and for space hardware • Most require moderate to long cures (1-2 h) • Limited thermal stabilities • Fine absorption of water presents delamination and cracking problem during reflow soldering

This issue led to an increase in research and development on new alloys to reduce and eliminate lead (Pb-free solder) in many centres and research institutes, such as the National Center for Manufacturing Science in the U.S., the Japan Institute of Electronics Packaging, and the Japan Electronics Industries Development Association. The new Pb-free alloys

used in the electronics industry need to be environmentally friendly and have various properties, such as good wettability, low soldering temperature, low cost, adequate strength, and good thermal fatigue resistance [28]. To date, several Pb-free alloy systems have emerged as replacements for SnPb alloys, including binary alloy systems (e.g., SnAu, SnCu, SnAg, SnZn, SnBi, SnIn, and InBi) and ternary alloy systems (e.g SnAgCu) [28,30,32]. **Table 1.4** summarises the classification of the most popular Pb-free solder candidates in three groups (low, medium, and high-temperature alloys) as their solidus temperature (T_s) according to the ISO 9453:2014 and JIS Z3282:2017 standards.

Table 1.4 Classification of some Pb-free solders.

Group	Alloy designation	Melting temperature (T_m) or solidus temperature (T_s), °C	Liquidus temperature (T_l), °C	Tensile strength (MPa)	Elongation (%)	Reference
High temperature alloys ($T_s \geq$ 217 °C)	Sn95Sb5	235	240	31	25	[28]
	Sn99.3Cu0.7	227	227	28	44	[33]
	Sn96.5Ag3.5	221	221	30-35	25-38	[34]
	Sn98.5Ag1Cu0.5	217	227	27	21	[35]
	Sn96.5Ag3Cu0.5	216	221	25	20	[36]
Medium temperature alloys (217 °C > $T_s \geq$ 150 °C)	Sn91Zn9	198	203	42	20	[37]
	Sn89.9Zn9Cr0.1	198	203	43	30	[37]
Low temperature alloys ($T_s <$ 150 °C)	Bi58Sn42	139	139	50	31	[38]
	In52Sn48	118	118	10	38	[39–43]
	In60Bi40	72	83	13	43	[32]

Among Pb-free alloys, binary eutectic alloys SnCu, SnAg, and ternary SnAgCu (SAC) are some good candidates to replace SnPb alloy in major soldering applications (such as SMT card assembly) owing to their good performance and suitable mechanical properties [44]. However, they have a higher melting temperature (~217ºC) than eutectic SnPb alloy (T_m = 183°C), resulting in a higher reflow temperature, which introduces the necessity for board designs and component technology to be compatible. Thus, the near-ternary SAC compositions are not appropriate for Pb-free alloy joints requiring a high ductility, low modulus, or enhanced impact resistance [44]. The Sn91Zn9 alloy appears to be an attractive alternative given its excellent mechanical properties with ultimate tensile strength (UTS) of approximately 61 MPa [45]. However, its poor wettability on a Cu substrate, and corrosion in humidity, are the two main concerns about this alloy [46,47]. Although its melting temperature (T_m = 199°C) is lower than that of SAC solder, it is still relatively high for some flexible organic substrates.

Moreover, three-dimensional (3D) integrated circuit (IC) technology is a promising way to maintain Moore's law of miniaturization, and solves the challenges of the semiconductor industry such as: heterogeneous integration, reduced power, and cost reduction [48]. In 3D integration packaging, a stack of several device layers are electrically interconnected by through-silicon-vias (TSVs) and micro-bumps in a vertical fashion [49,50]. When the chips become more functionalized, the packaging structures become more integrated. In this way, the chip size increases, and warpage issue during reflow is serious [51]. Especially, with the trend for increasingly compact and flexible electronic devices, polymeric substrate materials such as PET and PEN will be widely used. With these groups of flexible substrate materials, the maximum heating temperature does not exceed 180 °C because high-temperature processing would damage the mechanical properties of the substrate. Therefore, alloys belonging to the medium- and high-temperature alloy groups, as shown in **Table 1.4,** are not suitable for this application.

In flexible electronic devices and 3D IC packaging, thinner components with high-density I/Os and smaller solder bumps are needed to connect ICs with the substrates. For example, in a package-on-package (PoP) structure, which is widely used in mobile devices,

since two or more packages are assembled on top of each other, several reflows will be required to do so. It means that low, medium, and high melting temperature alloys will work together so that the different components can be integrated. Therefore, the melting point of solder alloys is of concern. This is because the first level of solder joints should have the highest melting point (~ 300 °C), so during the processing of the second-level solder joints, the former will not melt. Furthermore, thermal warpage is a serious issue during reflow because of CTE mismatch between parts. The application of low melting point solder is the most effective way of resolving the warpage issue because the reflow temperature can be reduced. Thus, research and development of solder materials with low melting temperatures has become essential in the era of the IoT [30].

1.3.2 Low-temperature alloys

According to the JIS Z3282:2017 standard, the solidus temperature of low melting temperature alloys is less than 150 °C. From **Table 1.4**, it can be seen that the Bi58Sn42, In60Bi40, and In52Sn48 alloys are the prime candidates for low-temperature applications and flexible electronic devices using flexible substrate requiring an operating temperature below 180°C [50]. The eutectic Bi58Sn42 alloy has good strength (UTS ~56 MPa [52]) but poor wettability [53], ductility, and fatigue resistance [52]. The microstructure of the as-solidified eutectic Bi58Sn42 alloy is composed of the Sn phase and Bi phase [54]. However, coarsening of the microstructure during thermal ageing and the intrinsic brittleness of the Bi phase are disadvantages of this alloy [38]. Many researchers have studied adding alloying elements such as Cu [55], In [56], Ag [57], Zn [38], and Sb [58], in different concentrations in order to improve the properties of the Bi58Sn42 alloy. For example, 0.5 and 1 wt.% Zn effectively refines the eutectic Sn58Bi alloy microstructure and improves elongation and tensile strength, both before and after thermal ageing [38]. The wettability of Sn-58Bi solder can be enhanced by adding 0.5 wt.% Ag or 0.1 wt.% rare earth (RE) [59]. Although some added elements can improve the mechanical properties of the SnBi alloy, most do not change the melting point, which limits the use of the alloy as a low-temperature solder for flexible substrates that require a low operating temperature, such as heat-

stabilised PEN and heat-stabilised PET. To achieve a wider low-temperature packaging window, a lower soldering temperature is needed.

In the other hand, the In60Bi40 alloy exhibits a good elongation (43%) and tensile strength (13 MPa) [32]. However, it has been reported that even at room temperature most solder alloys exhibit a homologous temperature (T_h) greater than 0.6, this leads to the solder joint can be susceptible to creep deformation and fatigue failure [28]. Therefore, In60Bi40 alloy with a very low melting temperature of approximately 72 °C ($T_h = T/T_m = 298K/345K = 0.86$), will be susceptible to creep deformation and fatigue failure even under normal operating conditions. In addition, the large In content increases the cost leading to limited use of this alloy. Besides, the binary InSn alloy has a eutectic composition of 51.7 at.% In and 48.3 at.% Sn (known as In52Sn48 alloy commercially), which has a single melting point of 118°C. The phase diagram of a binary InSn system is shown in **Figure 1.7** [60]. The equilibrium phases are two intermediate phases β-(In-rich, tetragonal crystal structure) and γ-(Sn-rich, hexagonal crystal structure).
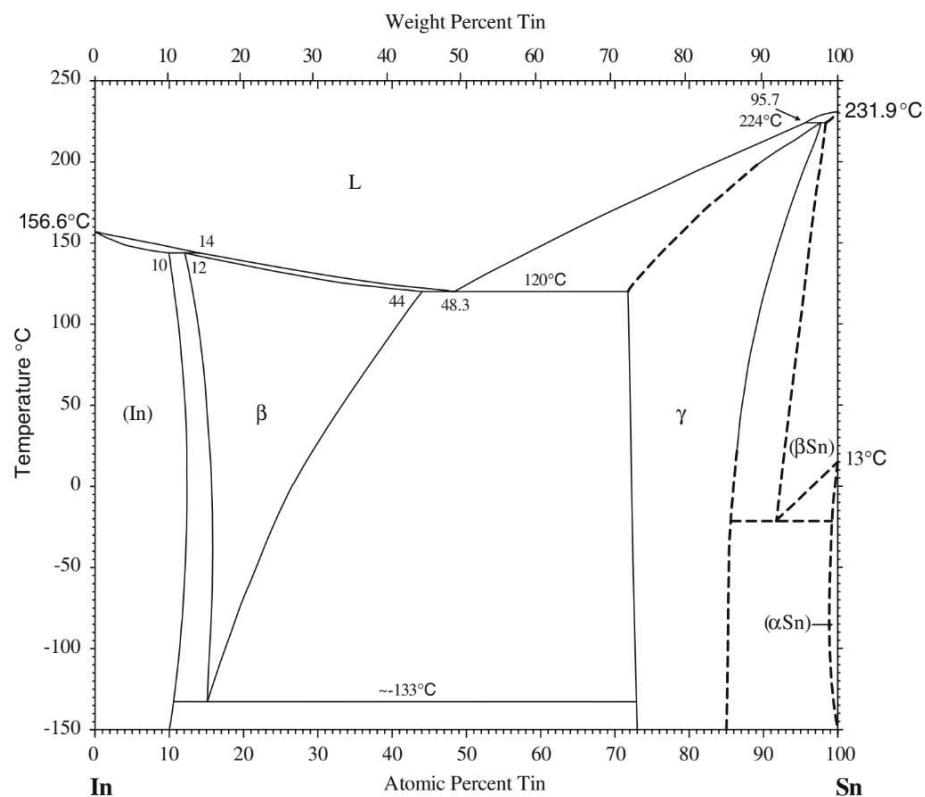
Figure 1.7 The phase diagram of a binary InSn system [60].

Both of the β and γ intermetallic compounds have large compositional homogeneity ranges [60,61]. Shepelevich reported that the microhardness ($H\mu$) of InSn alloy depends on the chemical composition of the alloy, and the microhardness is at a minimum with the eutectic composition. The microhardness of the β phase increases as the content of Sn (in β phase) increases ($H\mu$ = 30-40 MPa), and that of the γ phase increases as the In content (in γ phase) increases ($H\mu$ = 126-137 MPa), based on the solid-solution hardening mechanism [62,63]. Although the γ-phase is harder than the β-phase [43,62,64], both the β and γ phases are relatively soft and ductile, which explains the high ductility performance of the InSn alloy [50,61,65]. It has been reported that the InSn alloy exhibits good wettability [61,66–68], meaning that it can be used for many kinds of substrate, which can be either metal or non-metal, such as Cu, glass, ceramic materials, and flexible polymer [69–73]. The two intermediate γ and β phases occupy a wide composition range, making it an ideal system to investigate the nanoscale phase and phase transition [70]. The eutectic composition of InSn solder, which has an intrinsically low electrical resistivity of (10.0−15.0) μΩ.cm [42], is much lower than that of the Sn58Bi alloy (72.3 μΩ.cm [74]). Therefore, InSn solder can facilitate the rapid transfer of electronic/electrical signals between microchips and within conductive patterns on a substrate [72]. **Table 1.5** summarises the main properties of In52Sn48 in comparison with Bi58Sn42.

Table 1.5 The main properties of In52Sn48 and Bi58Sn42 alloys.

Property	In52Sn48 alloy	Bi48Sn42 alloy	Remark
Melting temperature (°C, Kenvin)	118, 391	139, 412	[28], [54]
Tensile strength (MPa)	8-11	52-72	[39–42], [52]
Elongation (%)	36-38	23-31	[43], [54]
Electrical resistivity (μΩ.cm)	10-15	72	[42], [74]
Elastic modulus (GPa)	24	42	[75], [28]
Coefficients of thermal expansion (CTE, $\times 10^{-6}$ /°C)	20 at 20 °C	15 at 20 °C	[42]
Thermal conductivity (W/mK)	34 at 85 °C	21 at 85 °C	[28]

The most significant difference under operating conditions for conventional electronics and flexible electronic devices is that repetitive mechanical strains, such as bending or folding, which result in direct mechanical stress on flexible electronics [76]. Thus, the reliability issue of flexible electronic devices are mainly caused by bending fatigue or thermo-mechanically dynamic operations [77,78]. Therefore, flexible electronic devices requires characterizing thermo-mechanical properties, including both strength, stiffness, and ductility of the constituent materials [78]. As the polymer substrates (e.g., PEN, PET) are considerably less thermally stable compared to conventional rigid substrate such as Si and glass, the low-melting temperature is the first selection criterion of solder alloys for flexible electronic applications [79]. Next, a high ductility alloy can absorb the thermal stress between the chip and its substrate and enhances the low cycle fatigue resistance of solder joints [42,50]. So, elongation is the second important property of solder alloys need to be considered. Moreover, the flexible electronics circuitry will experience deformation during operation and application, a low elastic modulus is the third important selection criterion for the joining material because the stress induced in the solder joint will be lower for a given strain, based on Hooke's law [28,80]. Besides, a high tensile strength of solder alloy will help improve the thermal fatigue resistance and service life of the solder joint. As mentioned in **Table 1.5**, the InSn-based alloy has a lower melting temperature (118 °C), lower elastic modulus (24 GPa), lower electrical resistivity (10-15 $\mu\Omega$.cm), higher thermal conductivity (34 W/mK), and higher elongation (36-38 %) than Sn58Bi42 alloy. Thus, this alloy is a good candidate for low melting temperature applications using a flexible substrate.

1.4 Reliability concerns for In52Sn48 interconnection

1.4.1 Microstructural coarsening

The microstructure of a material is composed of different phases and their defects, morphology, and distribution in a material. The composition and microstructure of an alloy determine the electrical, thermal, and mechanical properties of the material [42]. Generally, the microstructure of a material is described by the grain size, type of phases, and the structure present.

Figure 1.8 A typical microstructure of the eutectic In52Sn48 alloy.

Figure 1.8 presents a typical microstructure of the eutectic In52Sn48 alloy. It has been reported that the eutectic InSn solder has an irregular microstructure with lamellar features and equiaxed grains of the γ and β phases [28,41,65]. When expressed in Kelvins, the homologous temperature of the In52Sn48 alloy at room temperature (T~25°C~298 K) is approximately 0.76 ($T_h = T/T_m = 298K/391K = 0.76$), which results in an exponentially higher rate of diffusion-dependent deformation [30]. Seyyedi observed a significant microstructural coarsening in alloy joints on a Cu substrate after 174 days of ageing at ambient temperature [28,41]; the phase coarsening and uneven microstructure are factors that reduce strength and adversely affect the long-term reliability of the alloy joint.

1.4.2 Mechanical limitations

As discussed, InSn-based alloys exhibit better ductility compared to BiSn alloys; elongation of the In-48Sn alloy is approximately four times greater than that of the Sn-37Pb alloy at very low temperatures (-196°C) [81]. Moreover, the InSn alloy exhibits a more diffusive deformation pattern than SnBi samples, and the microstructure of SnIn remains the same after testing because of the softness of the alloy [50].

However, the tensile strength of the InSn alloy is low (8.0-11.0 MPa), and it decreases further with an increasing proportion of the soft β (In-rich) phase. Elongation is an important property because the high ductility of solder enhances the low-cycle fatigue resistance of an alloy joint. It should be noted that if mechanical strength could be improved, the InSn-based alloy would be a good candidate for solder material for flexible devices [42]. The ratio of the soft β (In-rich) phase in the alloy matrix is the main factor leading to the poor strength of the InSn alloy. Reducing the β phase ratio is expected to improve the mechanical properties of the In52Sn48 alloy. **Table 1.6** summarises the advantages and disadvantages of the In52Sn48 alloy.

1.4.3 Improvement of alloy properties by microalloying

It has been reported that minor alloy additions to Pb-free (SnCu-based, SnBi-based, and SAC) solders can improve the physical, electrical, mechanical or metallurgical properties of alloys [44]. This modification acts to reduce reliability issues affecting alloy joints, such as excessive Cu consumption from the substrate, fatigue crack growth from large intermetallic compounds (IMCs), and void formation during the soldering process [44,82–84]. The effects of minor alloying elements additions to Pb-free solders using Zn, Co, Fe, Cu, Al, Ni, Ag and others have been investigated [84–90]. Of these, Zn is the most promising and frequently evaluated addition to Sn-rich solders because of benefits that include suppression of large Ag_3Sn plate and IMC growth, especially Cu_3Sn at the Cu/solder interface; reduction in void formation at the Cu/Sn IMC interface; reduction in Cu consumption during reflow and ageing; promotion of a uniform Sn dendrite microstructure; and improved drop impact resistance [44].

Table 1.6 Advantages and disadvantages of the eutectic In52Sn48 alloy.

Advantages	Disadvantages
Very low melting temperature (118 °C) High ductility Low electrical resistivity Good wettability	Microstructural coarsening Low tensile strength

Wang et al. studied the effect of 1.0-6.0 wt.% Zn addition on the properties of an InSn alloy, and the results revealed that the addition reduces the melting temperature; however, the InSn-xZn alloys exhibit a low UTS of approximately 6 MPa and an average elongation of 17-31% [91]. On the other hand, Ag and Cu are two elements with good electrical conductivity [92]. Many studies have shown that adding a certain amount of Ag or Cu can improve mechanical properties as well as the fatigue resistance of alloys and joints when working at high temperatures [30,44,85,93,94]. Moreover, Ohnuma pointed out that adding an InSn alloy with a content of less than 2 wt.% Ag helps this alloy to maintain a low-temperature range [74]. Therefore, Cu and Ag are two good candidates that can be added to the In52Sn48 alloy with the expectation of improving the mechanical properties and solderability of the alloy.

It has been reported that Sn-In alloys with added Ag exhibit enhanced elongation and creep resistance [43,95,96], but lower electrical resistance has also been investigated [95]. These studies have shown that amounts of Ag greater than 2.5% result in a higher melting temperature of the InSn alloy. Furthermore, several studies have investigated the effect of Cu on InSn alloys [97,98]. For example, Susan et al. investigated the solidification and microstructures of InSn-Cu (ISC) alloys with 0.35 to 1.5 wt.% Cu [97]. They found that the melting behaviour of ISC alloys is similar to eutectic InSn alloys, and a ternary IMC of Cu_2In_3Sn was observed in the as-solidified alloy. Several studies have also reported phase equilibria and solidification of InSn-Cu ternary alloys [99–101]. However, the effect of the addition of Cu and Ag on the mechanical properties of eutectic InSn alloys has not been fully investigated to date, especially the relationship between the microstructure and mechanical properties of both alloy and joint. Therefore, these shortcomings will be addressed in this thesis.

1.5 Research motivation

In recent years, flexible electronics have attracted considerable attention because of their excellent flexibility and stretchability while maintaining electrical properties. According to research by IDTechEx, flexible device market sales are growing by more than 30% annually and will reach $301 billion by 2028, which is more than double the sales of

the current conventional integrated circuits industry [2,21]. Unsurprisingly, therefore, the number of studies and publications on flexible electronic devices is increasing rapidly. **Figure 1.9** shows the number of publications with the keyword "flexible electronics" according to statistics from the Web of Science website [3,21]. To meet the requirements of new flexible electronic devices, research on alternative mounting and bonding materials, such as lower temperature alloys or conductive adhesives, is essential. The selection of material for the most flexible plastic circuits depends on a combination of performance, processing, and cost. Heat-stabilised PEN/PET are mostly used as substrate materials for flexible electronics because of advantages that include: low cost, transparency almost like glass, low water absorption and moisture contamination, and competitive mechanical properties [19,24]. However, the low melting temperature of heat-stabilised PET/PEN is not compatible with conventional solder temperatures. Therefore, adhesives or low-temperature solders must be considered for attaching components.
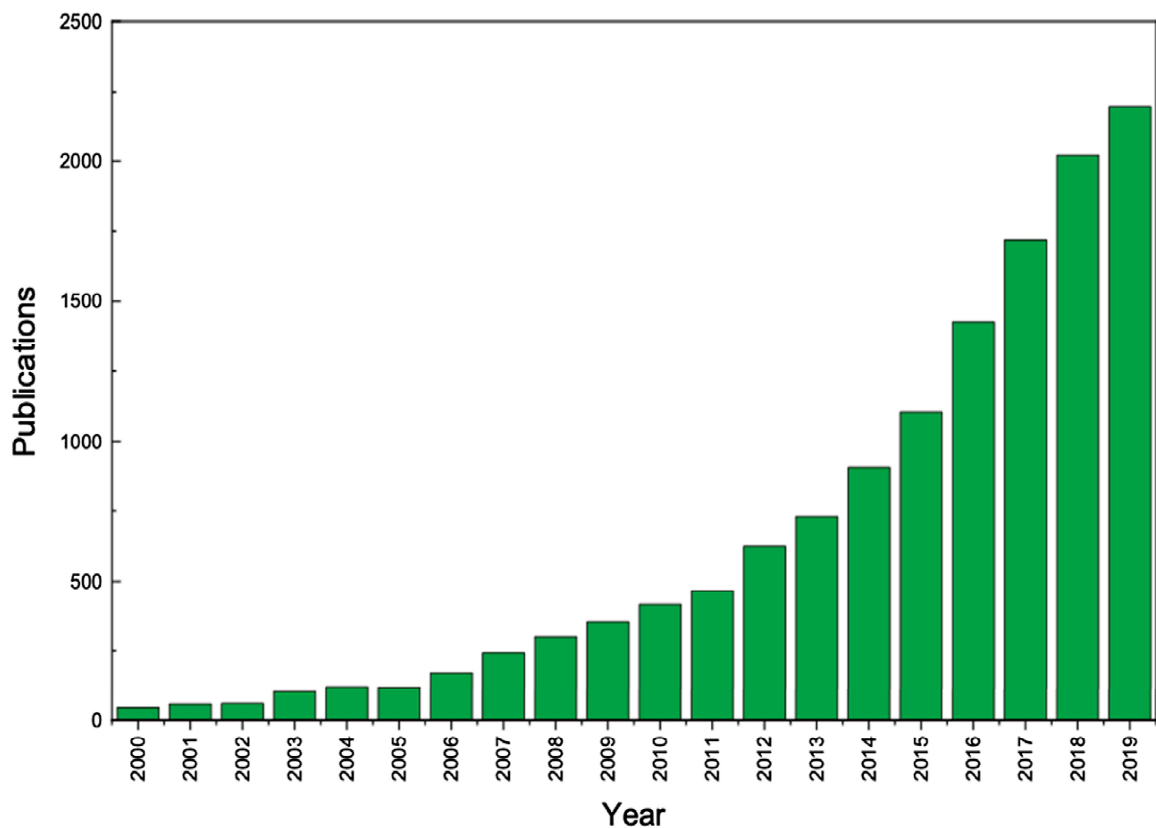
Figure 1.9 Research publications per year obtained for the term "flexible electronics" on web of science [3].

As previously discussed, the medium to high melting point solders group (such as SAC105, SAC305, Sn91Zn9) has two undesirable effects on packaging technology: warpage of the intermediate layer, and thermal stability of the polymer substrate [50]. Among low-temperature alloys, the In52Sn48 alloy has a very low melting temperature, high ductility, and low electrical resistivity, and could become a good candidate for joining material in flexible electronics. However, phase coarsening and low tensile strength are disadvantages of this alloy. The motivation for this study is therefore focused on solving and overcoming the limitations of the eutectic In52Sn48 alloy.

1.6 Research purpose and outline

1.6.1 Research purpose

The main purpose of this study is to solve two main problems of the In52Sn48 alloy, namely, microstructural coarsening and low tensile strength while maintaining or reducing the melting temperature of the alloy. In this thesis, the effects of 0.5-1.5 wt.% Ag, and 1.0-8.0 wt.% Cu additions on the microstructure and mechanical properties of the eutectic In52Sn48 alloy were investigated. Then, the InSn-based alloys were selected to make the alloy joint on a Cu substrate. The wettability of the new alloys on the Cu substrate, the microstructure evolution, interfacial reaction, and mechanical properties of the alloy joints, were studied. The joint reliability was also examined using a thermal ageing test.

Since flexible electronics technology is in the infancy of development, and the requirements for solder alloys depend on many different factors such as: scope of application, working conditions, life requirements, etc [20,102]. Therefore, there is not yet a general regulation for joining materials applied in flexible electronic devices. However, based on the above discussed, the thermomechanical properties including tensile strength and elongation of solder should be considered. When compared with common solder materials in Table 1.4, the mechanical properties of In60Bi40 alloy are taken as the basis for comparison and evaluation for the research results in this thesis.

1.6.2 Outline

Chapter 1 gives a brief introduction of flexible electronic devices and the interconnection technologies used in flexible electronic devices, including Pb-free and low-temperature alloys. Reliability concerns about the eutectic In52Sn48 alloy are discussed and solutions proposed to address these concerns.

Chapter 2 describes the effects of Ag addition to the eutectic In52Sn48 alloy. The microstructure refinement mechanism and mechanical properties of the new alloy are investigated. The fracture surface of tensile test samples is examined.

Chapter 3 details the effects of Cu addition to the eutectic In52Sn48 alloy. Microstructure refinement in relationship with the mechanical properties of the new alloy is discussed. The fracture surface of tensile test samples was also examined.

Chapter 4 explains the selection of the new alloys described in Chapter 3 to create an alloy joint on a Cu substrate. The wettability of the new alloy on the Cu substrate is investigated. The evolution of the microstructure, interfacial reaction, and shear strength of the alloy joints are investigated.

Chapter 5 describes the results of isothermal ageing to examine the reliability of the new alloy bars (Chapter 3) and alloy joints (Chapter 4). For alloys, the microstructure changes after thermal ageing are studied, and the mechanical properties are also investigated. For the alloy joints, the microstructure evolution, interfacial reaction and shear strength alloy joints are investigated.

Chapter 6 summarises the results obtained in each chapter and suggests future work.

Reference

1. Bonnassieux, Y.; Brabec, C.J.; Cao, Y.; Carmichael, T.B.; Chabinyc, M.L.; Cheng, K.; Cho, G.; Chung, A.; Cobb, C.L.; Distler, A. The 2021 flexible and printed electronics roadmap. *Flex. Print. Electron.* **2022**, *6*, 1–49.

2. Wang, Z.; Sun, L.; Ni, Y.; Liu, L.; Xu, W. Flexible Electronics and Healthcare Applications. *Front. Nanotechnol.* **2021**, *3*, 1–16, doi:10.3389/fnano.2021.625989.

3. Corzo, D.; Tostado-Blázquez, G.; Baran, D. Flexible Electronics: Status, Challenges and Opportunities. *Front. Electron.* **2020**, *1*, 1–13, doi:10.3389/felec.2020.594003.

4. Wang, P.; Hu, M.; Wang, H.; Chen, Z.; Feng, Y.; Wang, J.; Ling, W.; Huang, Y. The Evolution of Flexible Electronics: From Nature, Beyond Nature, and To Nature. *Adv. Sci.* **2020**, *7*, 1–29, doi:10.1002/advs.202001116.

5. Peng, H.; Sun, X.; Weng, W.; Fang, X.; Peng, H.; Sun, X.; Weng, W.; Fang, X. Flexible Electronic Devices Based on Polymers. In *Polymer Materials for Energy and Electronic Applications*; 2017; pp. 325–354 ISBN 978-0-12-811091-1.

6. Kwang-Ting (Tim) Cheng; Huang, T.-C. What is Flexible Electronics 2009, *39*, 5–6.

7. Liu, W.; Uy, W.; Chan, A.; Shangguan, D.; Behr, A.; Abe, T.; Tomohiro, F. Development of flexible hybrid electronics using reflow assembly with stretchable film. *Proc. - Electron. Components Technol. Conf.* **2019**, *2019-May*, 1272–1278, doi:10.1109/ECTC.2019.00197.

8. Davila-Frias, A.; Yadav, O.P.; Marinov, V. A Review of Methods for the Reliability Testing of Flexible Hybrid Electronics. *IEEE Trans. Components, Packag. Manuf. Technol.* **2020**, *10*, 1902–1912, doi:10.1109/TCPMT.2020.3029250.

9. S.Wong, W.; Salleo, A.; Tuller, H.L. *Flexible Electronics: Materials and Applications*; 2009; ISBN 9780387743622.

10. Fu, M.C.; Ueda, M.; Ando, S.; Higashihara, T. Development of Novel Triazine-Based Poly(phenylene sulfide)s with High Refractive Index and Low Birefringence. *ACS Appl. Mater. Interfaces* **2020**, doi:10.1021/acsomega.9b04152.

11. Koh, W.S. Nano-Graphene And Its Derivatives For Fabrication Of Flexible Electronic Devices: A Quick Review. *Adv. Mater. Lett.* **2019**, *10*, 676–681, doi:10.5185/amlett.2019.0050.

12. Wang, S.Q.; Chinnasamy, T.; Lifson, M.A.; Inci, F.; Demirci, U. Flexible Substrate-Based Devices for Point-of-Care Diagnostics. *Trends Biotechnol.* **2016**, *34*, 909–921, doi:10.1016/j.tibtech.2016.05.009.

13. Joo, J.; Eom, Y.S.; Jang, K.S.; Choi, G.M.; Choi, K.S. Development of bonding process for flexible devices with fine-pitch interconnection using Anisotropic Solder Paste and Laser-Assisted Bonding Technology. *Proc. - Electron. Components Technol. Conf.* **2020**, *2020-June*, 1309–1314, doi:10.1109/ECTC32862.2020.00207.

14. Linghu, C.; Zhang, S.; Wang, C.; Song, J. Transfer printing techniques for flexible and stretchable inorganic electronics. *npj Flex. Electron.* **2018**, *2*, doi:10.1038/s41528-018-0037-x.

15. Arrese, J.; Vescio, G.; Xuriguera, E.; Medina-Rodriguez, B.; Cornet, A.; Cirera, A. Flexible hybrid circuit fully inkjet-printed: Surface mount devices assembled by silver nanoparticles-based inkjet ink. *J. Appl. Phys.* **2017**, *121*, doi:10.1063/1.4977961.

16. Banach, M. A Low Cost OTFT Platform for Truly Flexible Electronics. In Proceedings of the FlexEnable; 2016.

17. Garner, S.; Glaesemann, S.; Li, X. Ultra-slim flexible glass for roll-to-roll electronic device fabrication. *Appl. Phys. A Mater. Sci. Process.* **2014**, *116*, 403–407, doi:10.1007/s00339-014-8468-

2.

18. Logothetidis, S. *Handbook of Flexible Organic Electronics: Materials, Manufacturing and Applications*; Woodhead Publishing, Elsevier Ltd., 2015; Vol. 68; ISBN 978-1-78242-035-4.

19. Wiklund, J.; Karakoç, A.; Palko, T.; Yiğitler, H.; Ruttik, K.; Jäntti, R.; Paltakari, J. A Review on Printed Electronics: Fabrication Methods, Inks, Substrates, Applications and Environmental Impacts. *J. Manuf. Mater. Process.* **2021**, *5*, 89, doi:10.3390/jmmp5030089.

20. Koyuncu, M.; Lorenz, E.; Zimmermann, A. *Advanced interconnection technologies for flexible organic electronic systems*; Elsevier Ltd, 2015; ISBN 9781782420439.

21. Zhou, Z.; Zhang, H.; Liu, J.; Huang, W. Flexible electronics from intrinsically soft materials. *Giant* **2021**, *6*, 100051, doi:10.1016/j.giant.2021.100051.

22. Lu, Q.H.; Zheng, F. *Polyimides for electronic applications*; Elsevier Inc., 2018; ISBN 9780128126400.

23. Wu, X.; Shu, C.; He, X.; Wang, S.; Fan, X.; Yu, Z.; Yan, D.; Huang, W. Optically Transparent and Thermal-Stable Polyimide Films Derived from a Semi-Aliphatic Diamine: Synthesis and Properties. *Macromol. Chem. Phys.* **2020**, *221*, 1–7, doi:10.1002/macp.201900506.

24. Zardetto, V.; Brown, T.M.; Reale, A.; Di Carlo, A. Substrates for flexible electronics: A practical investigation on the electrical, film flexibility, optical, temperature, and solvent resistance properties. *J. Polym. Sci. Part B Polym. Phys.* **2011**, *49*, 638–648, doi:10.1002/polb.22227.

25. MacDonald, W.A.; Looney, M.K.; MacKerron, D.; Eveson, R.; Adam, R.; Hashimoto, K.; Rakos, K. Latest advances in substrates for flexible electronics. *J. Soc. Inf. Disp.* **2007**, *15*, 1075, doi:10.1889/1.2825093.

26. Park, J.; Lee, J.; Park, S.; Shin, K.H.; Lee, D. Development of hybrid process for double-side flexible printed circuit boards using roll-to-roll gravure printing, via-hole printing, and electroless plating. *Int. J. Adv. Manuf. Technol.* **2016**, *82*, 1921–1931, doi:10.1007/s00170-015-7507-2.

27. Rofifah, D. *Adhesives Technology for Electronic Applications: Materials, Processing, Reliability*; 2011; ISBN 9781437778892.

28. Abtew, M.; Selvaduray, G. Lead-free solders in microelectronics. *Mater. Sci. Eng. R Reports* **2000**, *27*, 95–141, doi:10.1016/S0927-796X(00)00010-3.

29. Harper, C.A. Electronic Materials and Processes Handbook. *Electron. Mater. Process. Handb.* **2004**, 726.

30. Evans, J.W. *A Guide to Lead-free Solders - Physical Metallurgy and Reliability*; Engelmaier, W., Ed.; Springer London, 2007; ISBN 9781846283093.

31. Lau, J.H.; Lee, N.-C. *Assembly and Reliability of Lead-Free Solder Joints*; 2020; ISBN 9789811539190.

32. Jin, S.; Kim, M.S.; Kanayama, S.; Nishikawa, H. Microstructure and mechanical properties of indium–bismuth alloys for low melting-temperature solder. *J. Mater. Sci. Mater. Electron.* **2018**, *29*, 16460–16468, doi:10.1007/s10854-018-9738-0.

33. El-Daly, A.A.; Hammad, A.E. Development of high strength Sn-0.7Cu solders with the addition of small amount of Ag and in. *J. Alloys Compd.* **2011**, *509*, 8554–8560, doi:10.1016/j.jallcom.2011.05.119.

34. Osório, W.R.; Leiva, D.R.; Peixoto, L.C.; Garcia, L.R.; Garcia, A. Mechanical properties of Sn-Ag lead-free solder alloys based on the dendritic array and Ag3Sn morphology. *J. Alloys Compd.* 2013, *562*, 194–204.

35. Huo, F.; Jin, Z.; Le Han, D.; Zhang, K.; Nishikawa, H. Interface design and the strengthening-

ductility behavior of tetra-needle-like ZnO whisker reinforced Sn1.0Ag0.5Cu composite solders prepared with ultrasonic agitation. *Mater. Des.* **2021**, *210*, 110038, doi:10.1016/j.matdes.2021.110038.

36.   Lu, T.; Yi, D.; Wang, H.; Tu, X.; Wang, B. Microstructure, mechanical properties, and interfacial reaction with Cu substrate of Zr-modified SAC305 solder alloy. *J. Alloys Compd.* **2019**, *781*, 633–643, doi:10.1016/j.jallcom.2018.12.098.

37.   Chen, X.; Hu, A.; Li, M.; Mao, D. Study on the properties of Sn-9Zn-xCr lead-free solder. *J. Alloys Compd.* 2008, *460*, 478–484.

38.   Zhou, S.; Mokhtari, O.; Rafique, M.G.; Shunmugasamy, V.C.; Mansoor, B.; Nishikawa, H. Improvement in the mechanical properties of eutectic Sn58Bi alloy by 0.5 and 1 wt% Zn addition before and after thermal aging. *J. Alloys Compd.* **2018**, *765*, 1243–1252, doi:10.1016/j.jallcom.2018.06.121.

39.   Shu, Y.; Gheybi Hashemabad, S.; Ando, T.; Gu, Z. Ultrasonic powder consolidation of Sn/In nanosolder particles and their application to low temperature Cu-Cu joining. *Mater. Des.* **2016**, *111*, 631–639, doi:10.1016/j.matdes.2016.09.013.

40.   Cheong, J.; Goyal, A.; Tadigadapa, S.; Rahn, C. Reliable bonding using indium-based solders. *Reliab. Testing, Charact. MEMS/MOEMS III* **2004**, *5343*, 114, doi:10.1117/12.524823.

41.   Seyyedi, J. Thermal Fatigue Behaviour of Low Melting Point Solder Joints. *Solder. Surf. Mt. Technol.* **1993**, *5*, 26–32, doi:10.1108/eb037812.

42.   Glazer, J. Microstructure and mechanical properties of Pb-free solder alloys for low-cost electronic assembly: A review. *J. Electron. Mater.* **1994**, *23*, 693–700, doi:10.1007/BF02651361.

43.   Glazer, J. Metallurgy of low temperature Pb-free solders for electronic assembly. *Int. Mater. Rev.* **1995**, *40*, 65–93, doi:10.1179/imr.1995.40.2.65.

44.   Subramanian, K.N. *Lead-free Solders: Materials Reliability for Electronics*; 2012; ISBN 9780470971826.

45.   Hammam, M.; Allah, F.S.; Gouda, E.S.; Gendy, Y. El; Aziz, H.A. Structure and Properties of Sn-9Zn Lead-Free Solder Alloy with Heat Treatment. *Engineering* **2010**, *02*, 172–178, doi:10.4236/eng.2010.23024.

46.   Suganuma, K.K.N.; Nakamura, S.Y. Wetting and interface microstructure between Sn–Zn binary alloys and Cu 1997.

47.   Liu, S.; Xue, S.; Xue, P.; Luo, D. Present status of Sn–Zn lead-free solders bearing alloying elements.

48.   Tan, C.S.; Gutmann, R.J.; Reif, L.R. *Wafer Level 3-D ICs Process Technology*; Tan, C.S., Gutmann, R.J., Reif, L.R., Eds.; Springer Science+Business Media, LLC, 2008; ISBN 2013206534.

49.   Sakuma, K. *3D integration in VLSI Circuits: implementation technologies and applications*; Iniewski, K., Sakuma, K., Eds.; Taylor & Francis Group, LLC, 2018; ISBN 9781138710399.

50.   Liu, Y.; Tu, K.N. Low melting point solders based on Sn, Bi, and In elements. *Mater. Today Adv.* **2020**, *8*, doi:10.1016/j.mtadv.2020.100115.

51.   Tu, K.N. Reliability challenges in 3D IC packaging technology. *Microelectron. Reliab.* **2011**, *51*, 517–523, doi:10.1016/j.microrel.2010.09.031.

52.   Yang, F.; Zhang, L.; Liu, Z.; Zhong, S.; Ma, J.; Bao, L. Properties and Microstructures of Sn-Bi-X Lead-Free Solders. **2016**, *2016*.

53.   Lee, C.; Jung, S.; Shin, Y.-E.; Shur, C. The effect of Bi concentration on wettability of Cu substrate by Sn-Bi Solders. *Mater. Trans.* **2001**, *42*, 751–755.

54. Jiang, N.; Zhang, L.; Gao, L.-L.; Song, X.-G.; He, P. Recent advances on SnBi low-temperature solder for electronic interconnections. *J. Mater. Sci. Mater. Electron.* **2021**, *32*, 22731–22759, doi:10.1007/s10854-021-06820-7.

55. TAKAO, H.; YAMADA, A.; HASEGAWA, H.; MATSUI, M. Mechanical Properties and Solder Joint Reliability of Low-Melting Sn-Bi-Cu Lead Free Solder Alloy. *J. Japan Inst. Electron. Packag.* **2011**, *5*, 152–158, doi:10.5104/jiep.5.152.

56. Omid, M.; Hiroshi, N. Effects of Indium Content on the Tensile Properties of Sn-Bi-In. **2015**, *44*, 19–22.

57. Li, Y.; Chan, Y.C. Effect of silver (Ag) nanoparticle size on the microstructure and mechanical properties of Sn58Bi-Ag composite solders. *J. Alloys Compd.* **2015**, *645*, 566–576, doi:10.1016/j.jallcom.2015.05.023.

58. Sakuyama, S.; Akamatsu, T.; Uenishi, K.; Sato, T. Effects of a Third Element on Microstructure and Mechanical Properties of Eutectic Sn-Bi Solder. *Trans. Japan Inst. Electron. Packag.* **2009**, *2*, 98–103, doi:10.5104/jiepeng.2.98.

59. Dong, W.; Shi, Y.; Xia, Z.; Lei, Y.; Guo, F. Effects of trace amounts of rare earth additions on microstructure and properties of Sn-Bi-based solder alloy. *J. Electron. Mater.* 2008, *37*, 982–991.

60. Chen, S.W.; Wang, C.H.; Lin, S.K.; Chiu, C.N. Phase diagrams of Pb-free solders and their related materials systems. *J. Mater. Sci. Mater. Electron.* **2007**, *18*, 19–37, doi:10.1007/s10854-006-9010-x.

61. Goldstein, J.L.F.; Morris, J.W. The Effect of Substrate on the Microstructure and Mechanical Behavior of Eutectic Indium-Tin. *MRS Proc.* **1994**, *323*, doi:10.1557/proc-323-159.

62. Shepelevich, V.G.; Wang, J. Structure and microhardness of rapidly solidified In-Sn foils. *Inorg. Mater.* **2012**, *48*, 577–581, doi:10.1134/S0020168512050184.

63. Shalaby, R.M.; El-Sayed, M. Effect of heat treatment on the fracture and structure of tin-indium solder alloy. *Radiat. Eff. Defects Solids* **2005**, *160*, 23–31, doi:10.1080/10420150500032473.

64. Wang, J.Z.; Liu, M.L.; Li, D.Y. Structure and property stability of rapidly solidified In-Sn γ-phase alloy. *Adv. Mater. Res.* **2014**, *981*, 918–922, doi:10.4028/www.scientific.net/AMR.981.918.

65. Morris, J.W.; Goldstein, J.L.F.; Mei, Z. Microstructure and Mechanical Properties of Sn-In and Sn-Bi Solders. **1993**, 25–27.

66. Kim, D.-G.; Jung, S.-B. Interfacial reactions and growth kinetics for intermetallic compound layer between In–48Sn solder and bare Cu substrate. *J. Alloys Compd.* **2005**, *386*, 151–156.

67. Chuang, T.H.; Yu, C.L.; Chang, S.Y.; Wang, S.S. Phase identification and growth kinetics of the intermetallic compounds formed during In-49Sn/Cu soldering reactions. *J. Electron. Mater.* **2002**, *31*, 640–645, doi:10.1007/s11664-002-0136-1.

68. Koo, J.A.M.; Jung, S.B. Reliability of in-48Sn solder/Au/Ni/Cu BGA packages during reflow process. *J. Electron. Mater.* **2005**, *34*, 1565–1572, doi:10.1007/s11664-005-0166-6.

69. Yu, D.Q.; Lee, C.; Yan, L.L.; Thew, M.L.; Lau, J.H. Characterization and reliability study of low temperature hermetic wafer level bonding using In/Sn interlayer and Cu/Ni/Au metallization. *J. Alloys Compd.* **2009**, *485*, 444–450, doi:10.1016/j.jallcom.2009.05.136.

70. Shua, Y.; Andob, T.; Yinc, Q.; Zhouc, G.; Gua, Z. Phase Diagram and Structural Evolution of Tin/Indium (Sn/In) Nanosolder particles: From Non-Equilibrium state to Equilibrium state. *Nanoscale* **2017**, 1–12, doi:https://doi.org/10.1039/C7NR01402C.

71. Koo, J.M.; Jung, S.B. Effect of surface finish of substrate on mechanical reliability of In-48Sn solder joints in MOEMS package. *Microsyst. Technol.* **2007**, *13*, 1567–1573, doi:10.1007/s00542-006-

0344-3.

72. Kim, S.H.; Yeon, S.-M.; Kim, J.H.; Park, S.J.; Lee, J.E.; Park, S.-H.; Choi, J.-P.; Aranas, C.J.; Son, Y. Fine Microstructured In−Sn−Bi Solder for Adhesion on a Flexible PET Substrate: Its Effect on Superplasticity and Toughness. *ACS Appl. Mater. Interfaces* **2019**, A-J, doi:dx.doi.org/10.1021/acsami.9b04159.

73. Choi, J.-H.; Lee, K.-Y.; Jun, S.-W.; Kim, Y.-H.; Oh, T.-S. Contact resistance of the chip-on-glass bonded 48Sn-52In solder joint. *Mater. Trans.* **2005**, *46*, 1042–1046.

74. Zhou, S.; Yang, C. han; Lin, S. kang; AlHazaa, A.N.; Mokhtari, O.; Liu, X.; Nishikawa, H. Effects of Ti addition on the microstructure, mechanical properties and electrical resistivity of eutectic Sn58Bi alloy. *Mater. Sci. Eng. A* **2019**, *744*, 560–569, doi:10.1016/j.msea.2018.12.012.

75. Kim, J.W.; Jung, S.B. Characterization of the shear test method with low melting point In-48Sn solder joints. *Mater. Sci. Eng. A* 2005, *397*, 145–152.

76. Aftab M. Hussain *Introduction to Flexible Electronics*; Taylor & Francis Group, LLC, 2022; ISBN 9780367439668.

77. Yi, S.M.; Choi, I.S.; Kim, B.J.; Joo, Y.C. Reliability Issues and Solutions in Flexible Electronics Under Mechanical Fatigue. *Electron. Mater. Lett.* **2018**, *14*, 387–404, doi:10.1007/s13391-018-0043-0.

78. Kim, J.H.; Lee, I.; Kim, T.S.; Rolston, N.; Watson, B.L.; Dauskardt, R.H. Understanding mechanical behavior and reliability of organic electronic materials. *MRS Bull.* **2017**, *42*, 115–123, doi:10.1557/mrs.2017.3.

79. Kim, S.H.; Sangsun Yang Low Melting Temperature Solder Materials for Use in Flexible Microelectronic Packaging Applications. In *Recent Progress in Soldering Materials*; Intech, 2017; Vol. i, pp. 8–37.

80. van den Brand, J.; de Baets, J.; van Mol, T.; Dietzel, A. Systems-in-foil Devices, fabrication processes and reliability issues. *Microelectron. Reliab.* **2008**, *48*, 1123–1128, doi:10.1016/j.microrel.2008.06.030.

81. Shimizu, K.; Nakanishi, T.; Karasawa, K.; Hashimoto, K.; Niwa, K. Solder joint reliability of indium-alloy interconnection. *J. Electron. Mater.* **1995**, *24*, 39–45, doi:10.1007/BF02659725.

82. Xiong, M. yue; Zhang, L. Interface reaction and intermetallic compound growth behavior of Sn-Ag-Cu lead-free solder joints on different substrates in electronic packaging. *J. Mater. Sci.* **2019**, *54*, 1741–1768, doi:10.1007/s10853-018-2907-y.

83. Kang, S.K.; Shih, D.Y.; Leonard, D.; Henderson, D.W.; Gosselin, T.; Cho, S. il; Yu, J.; Choi, W.K. Controlling Ag3Sn plate formation in near-ternary-eutectic Sn-Ag-Cu solder by minor Zn alloying. *Jom* **2004**, *56*, 34–38, doi:10.1007/s11837-004-0108-4.

84. Zhao, J.; Miyashita, Y.; Mutoh, Y. Fatigue crack growth behavior of 96.5Sn-3.5Ag lead-free solder. *Int. J. Fatigue* **2001**, *23*, 723–731, doi:10.1016/S0142-1123(01)00034-2.

85. Liu, Y.; Ren, B.; Xue, Y.; Zhou, M.; Cao, R.; Zeng, X. Improvement on the mechanical properties of eutectic Sn58Bi alloy with porous Cu addition during isothermal aging. *Mater. Res. Express* **2021**, *8*, doi:10.1088/2053-1591/ac10d5.

86. Wang, C. hong; Kuo, C. yi; Guo, Y. bin Effects of Minor Cu, Ni and Ag Additions on the Reactions Between Sn-Based Solders and Co Substrate. *Jom* **2019**, *71*, 3023–3030, doi:10.1007/s11837-019-03573-x.

87. Li, J.F.; Agyakwa, P.A.; Johnson, C.M. Effect of trace Al on growth rates of intermetallic compound layers between Sn-based solders and Cu substrate. *J. Alloys Compd.* **2012**, *545*, 70–79, doi:10.1016/j.jallcom.2012.08.023.

88.   Qin, W.; Li, J.; Zhang, Q.; Jiang, S.; Feng, J.; Yang, W.; Zhan, Y. Effect of addition of Al and Cu on the properties of Sn–20Bi solder alloy. *J. Mater. Sci. Mater. Electron.* **2021**, doi:10.1007/s10854-021-07283-6.

89.   Kang, H.M.T.S.-B.S.: E. of A. and; Rajendran, S.H.; Jung, J.P. Low Melting Temperature Sn-Bi Solder: Effect of Alloying and Nanoparticle Addition on the Microstructural, Thermal, Interfacial Bonding, and Mechanical Characteristics. *Metals (Basel).* **2021**, *364*, 1–25.

90.   Wei, Y.; Liu, Y.; Zhang, L.; Zhao, X. Effects of endogenous Al and Zn phases on mechanical properties of Sn58Bi eutectic alloy. *Mater. Charact.* **2021**, *175*, 111089, doi:10.1016/j.matchar.2021.111089.

91.   Wang, J.; Mao, D.; Shi, L.; Zhang, W.; Zhang, X. Effect of Zinc Addition on the Microstructure, Thermal and Mechanical Properties of Indium-Tin-xZinc Alloys. *J. Electron. Mater.* **2019**, *48*, 817–826, doi:10.1007/s11664-018-6768-6.

92.   Bardeen, J. Electrical conductivity of metals. *Phys. Status Solidi* **1968**, *26*, 133–138, doi:https://doi.org/10.1063/1.1712751.

93.   Ohnuma, I.; Cui, Y.; Liu, X.J.; Inohana, Y.; Ishihara, S. Phase Equilibria of Sn-In Based Micro-Soldering Alloys. *J. Electron. Mater.* **2000**, *29*, 1113–1121, doi:https://doi.org/10.1007/s11664-000-0002-y.

94.   Jeong, G.; Yu, D.-Y.; Baek, S.; Kim, J.; Ko, Y.-H. Interfacial Reactions and Mechanical Properties of Sn–58Bi Solder Joints with Ag Nanoparticles Prepared Using Ultra-Fast Laser Bonding. *Materials (Basel).* **2021**, *14*, 1–16, doi:https://doi.org/10.3390/ma14020335.

95.   El-Bediwi, A.B.; El-Bahay, M.M. Influence of silver on structural, electrical, mechanical and soldering properties of tin-indium based alloys. *Radiat. Eff. Defects Solids* **2004**, *159*, 133–140, doi:10.1080/10420150410001670288.

96.   Jones, W.K.; Liu, Y.; Shah, M.; Clarke, R. Mechanical properties of Pb/Sn Pb/In and Sn-In solders. *Solder. Surf. Mt. Technol.* **1997**, 37–41.

97.   Susan, D.F.; Rejent, J.A.; Grant, R.P.; Vianco, P.T. The Solidification Behavior and Microstructure of In-Sn-Cu Solder Alloys with Low Cu. *4th Int. Brazing Solder. Conf.* **2009**, 1–6.

98.   Uemura, T.; Sakai, T.; Sakuyama, S. Improvement of mechanical properties of In-48mass%Sn solder by Ag and Cu addition. *Proc. 2016 IEEE 18th Electron. Packag. Technol. Conf. EPTC 2016* **2016**, 181–184, doi:10.1109/EPTC.2016.7861467.

99.   LIU, X.J.; LIU, H.S.; OHNUMA, I.; KAINUMA, R.; ISHIDA, K.; ITABASHI, S.; KAMEDA, K.; YAMAGUCHI, and K. Experimental determination and thermodynamic calculation of the phase equilibria in the Cu-In-Sn system. *J. Electron. Mater.* **2001**, *30*, 1093–1103, doi:10.3139/146.111135.

100. Lin, S.K.; Yang, C.F.; Wu, S.H.; Chen, S.W. Liquidus projection and solidification of the Sn-In-Cu ternary alloys. *J. Electron. Mater.* **2008**, *37*, 498–506, doi:10.1007/s11664-008-0380-0.

101. Riania, P.; Gabriele Cacciamania, Nadia Parodia, Gabriella Borzonea, Rinaldo Marazzaa, Francesca Nannib, G.G. Phase equilibria in the In–Sn-rich part of the Cu–In–Sn ternary system. *J. Alloys Compd.* **2009**, *487*, 90–97.

102. Karnaushenko, D.; Kang, T.; Bandari, V.K.; Zhu, F.; Schmidt, O.G. 3D Self-Assembled Microelectronic Devices: Concepts, Materials, Applications. *Adv. Mater.* **2020**, *32*, doi:10.1002/adma.201902994.

Chapter 2

Effect of the addition of Ag on the properties of the In52Sn48 alloy

2.1 Introduction

As mentioned in Chapter 1, Ag and Cu are the two elements selected to be added to the In52Sn48 alloy to overcome the limitations of this alloy, namely, uneven microstructure and phase coarsening. Generally, the chemical composition, thermal properties, mechanical properties and failure behaviour are the basic properties to be considered when studying the performance of a solder alloy [1,2]. Studies have reported that a small amount of Ag can reduce the melting point, improve the mechanical properties, and reduce the grain size of some lead-free alloys [3–5]. With the aim of maintaining or reducing the melting temperature and improving the mechanical properties of the In52Sn48 alloy, the author investigated the effect of the addition of x = 0.5, 1.0, and 1.5 wt.% of Ag on fusion start temperatures, microstructures, and mechanical properties of the In52Sn48-xAg (ISA) alloys. The fracture behaviour of the new alloys under the tensile test was also investigated.

2.2 Experimental procedure

2.2.1 Fabrication

We fabricated ISA alloys consisting of commercial In52Sn48 eutectic alloy and 0.5, 1.0, and 1.5 wt.% Ag from pure silver wire (99.99%; Nilaco Corporation, Japan). These elements were alloyed at 700ºC for 5 h in an alumina crucible inside an electric furnace (HPM-ON, AS ONE) in a nitrogen atmosphere. The chemical composition of the new alloys was analysed using a wet chemical titrimetric method (for Sn analysis) and an inductively coupled plasma (ICP) for other elements. The results are summarised in **Table 2.1**. Alloy bars (50 × 10 × 5 mm) were shaped using a casting mould, and then further shaped into dumbbells by wire electric discharge machining (Soldick AG 360L, Japan). **Figure 2.1** presents a schematic of the experimental procedure and the dimension of the dumbbells and the actual tensile specimen for a tensile test.

2.2.2. Characterisation methods

The melting behaviour of each ISA alloy was examined by differential scanning calorimetry (DSC; 7020, Hitachi, Japan) under a constant flow of N_2 in the range 50-250°C at a rate of approximately 10°C/min.
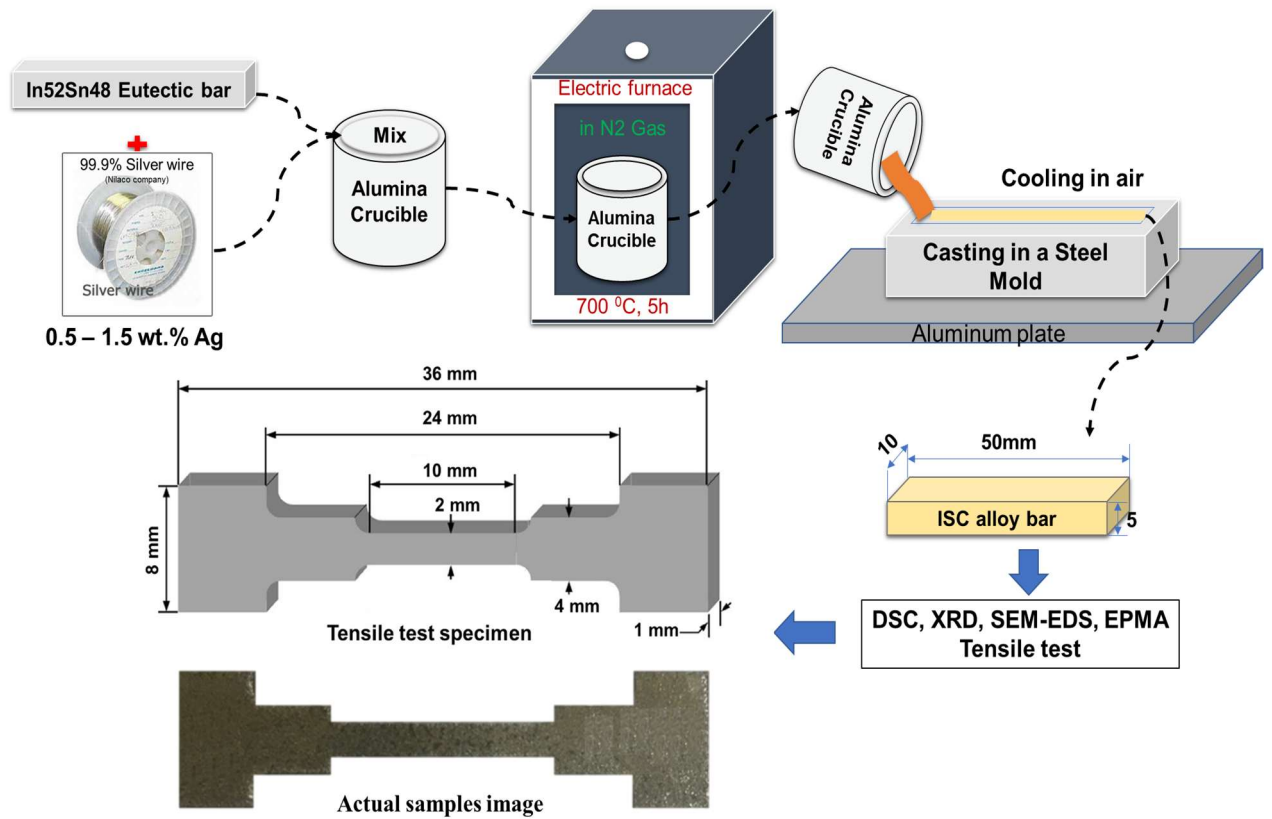
Figure 2.1 Schematic of the experimental procedure.

Table 2.1 Chemical composition of the eutectic In52Sn48 alloy and In52Sn48-xAg alloys.

Element	In52Sn48-0.5Ag (ISA4805), *wt. %*	In52Sn48-1.0Ag (ISA4810), *wt. %*	In52Sn48-1.5Ag (ISA4815), *wt. %*	In52Sn48 (IS48), *wt. %*
Sn	47.710	47.840	47.550	47.910
In	Balance	Balance	Balance	Balance
Ag	0.515	0.997	1.502	-
Cu	0.010	0.041	0.009	0.003
Bi	0.001	-	-	0.006
Zn	0.005	0.011	0.006	-
Pb	-	-	-	0.001

The fusion start temperature (T_f) was determined as required by the JIS Z 3198-1 standard. The microscopic specimens were carefully polished. First, the samples were ground flat with SiC grit paper #150 for 1-2 minutes. Then, the sample was further

ground with finer SiC grit papers #400, #800, #1200, and #2000 until the surface was shiny. Next, the samples were polished automatically for approximately 20-30 minutes using an alumina suspension (Buehler, USA, in the following order: 1.0 and 0.3 μm). Any alumina powders remaining on the surface of the sample after polishing were cleaned by an ultrasonic cleaner. To show the phases clearly, the sample surface was then etched with a solution of HCl 4% + ethanol in the ratio of 1:1 for 15-30s. The microstructures of the ISAs were then examined using scanning electron microscopy (SEM; SU-70, Hitachi, Japan). The crystal structures of the ISA alloys were determined by X-ray diffractometry (XRD; Ultima IV, Rigaku, Japan) in the 30-80° 2θ range at a scan rate of 1°/min. The microstructures and elemental distribution of the ISAs were determined by field-emission electron probe microanalysis (FE-EPMA; JXA-8530F JEOL). ImageJ software was used to calculate phase sizes and numbers. A total of 50 phases for each alloy were measured and used for calculating the average phase size. Tensile testing was conducted under a strain rate of 5×10^{-4} s^{-1} using a universal tensile machine (Autograph AG-X, Shimadzu, Japan). The average elongation (EL) and UTS were determined from tensile stress-strain curves and calculated based on the tensile results of eight test pieces for each alloy. The fracture surface of each tensile specimen was examined by SEM.

2.3 Results and discussion

2.3.1 Melting behaviour

The DSC curves for all the alloys are shown in **Figure 2.2**. In accordance with the JIS Z 3198-1 standard, the fusion start temperatures of the In52Sn48-0.5Ag (ISA4805), In52Sn48-1.0Ag (ISA4810), and In52Sn48-1.5Ag (ISA4815) alloys are defined by the extrapolated beginning of the DSC curve, determined by the point of intersection of the tangent with the point of maximum slope, on the principal side of the peak with the base line extrapolated. The values are 112.6, 112.7, and 113.2°C, respectively, which are all lower than that of the eutectic In52Sn48 (IS48) alloy (117.2°C). The addition of Ag slightly decreases the fusion start temperature of the eutectic IS48 alloy, which is attributable to the ternary eutectic reaction and was calculated by Ohnuma et al. to be 114°C for Sn-52.2In-0.9Ag (eq. (1)).

$$L \leftrightarrow \beta + \gamma + Ag_2In \qquad\qquad (1)$$
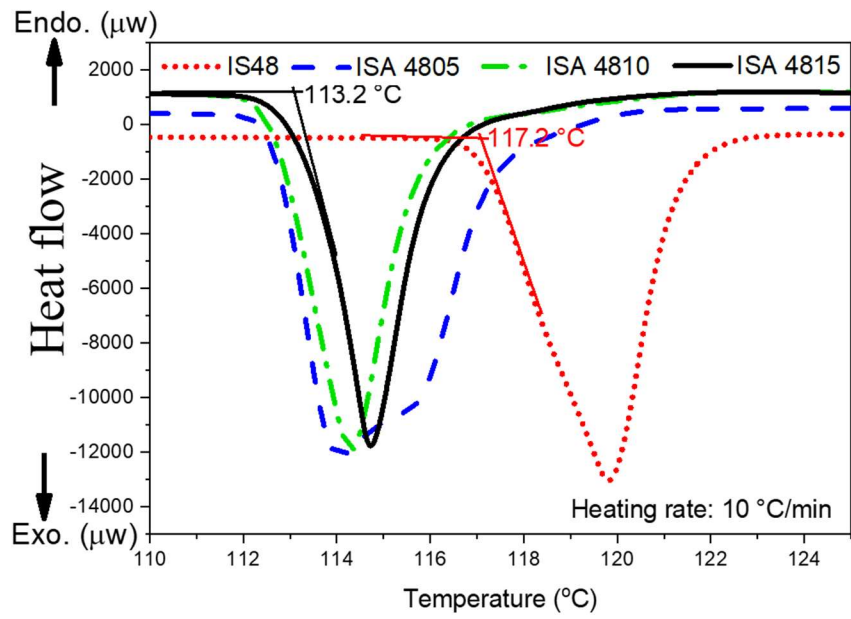
Figure 2.2 DSC curves of the various alloys: IS48, ISA4815, ISA4810 and ISA4805.
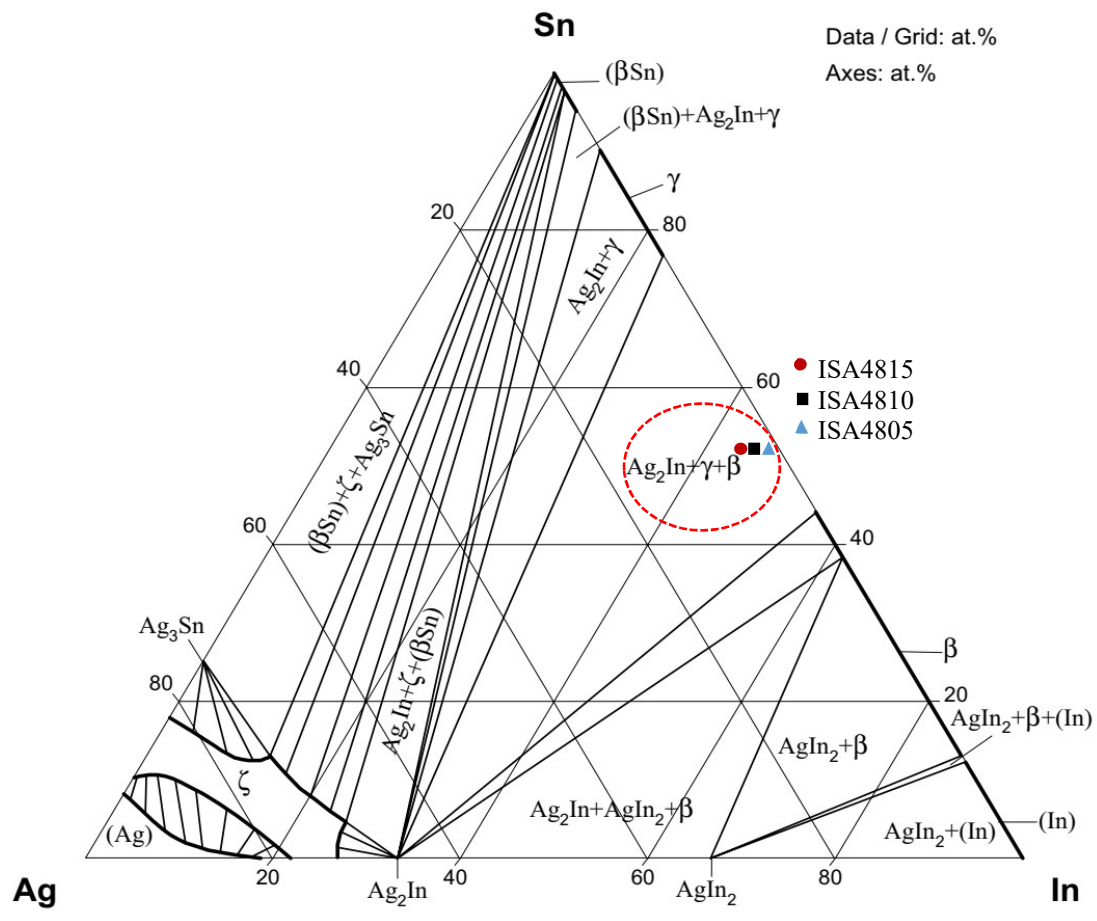
Figure 2.3 Calculated isothermal section of Ag-In-Sn ternary system at 113 °C [9].

This result is consistent with calculated isothermal section of Ag-In-Sn ternary system at 113 °C, as shown in **Figure 2.3** [9]. In which, the ISA4815, ISA4810, and ISA4805 alloys (in circle zone) exhibit three phases included $Ag_2In+\gamma+\beta$ phases as ternary

reaction (1). Moreover, the melting temperature of Sn-51.7In with 1.0-5.0 wt.% added Ag were predicted to increase with increasing silver content [6], in agreement with the results in this study.

2.3.2 Phase constitution

The XRD patterns for all alloys are displayed in **Figure 2.4**, which reveals the presence of ε-AgIn$_2$ in the new ISA alloys, as observed in other In-Sn-Ag alloys [19]. Although few studies have reported the presence of the Ag$_2$In IMC in ISA alloys [5,7], Chuang et al. [8] found that Ag$_2$In and AgIn$_2$ compete in In-49Sn/Ag alloyed specimens during ageing. At temperatures under 75°C, the dominant reaction is:

$$Ag_2In + 3In \rightarrow 2AgIn_2 \tag{2}$$

Hence, Ag-In IMC is transformed from Ag$_2$In to AgIn$_2$ by Eq. (2) in ISA alloys during slow cooling. In addition, EMPA maps of the alloys are shown in **Figure 2.5**, with EMPA point analyses providing the elemental content of all phases, as summarised in **Table 2.2.** AgIn$_2$, which is circular, exists in the In$_3$Sn phase in ISA alloys because the In-rich phase is required to transform according to Eq. (2). The diameter of the AgIn$_2$ phase becomes larger with the addition of more Ag, from 0.5-2.0 μm in ISA 4805 and 4810 alloys to 2.0-4.0 μm in ISA 4815 alloy.
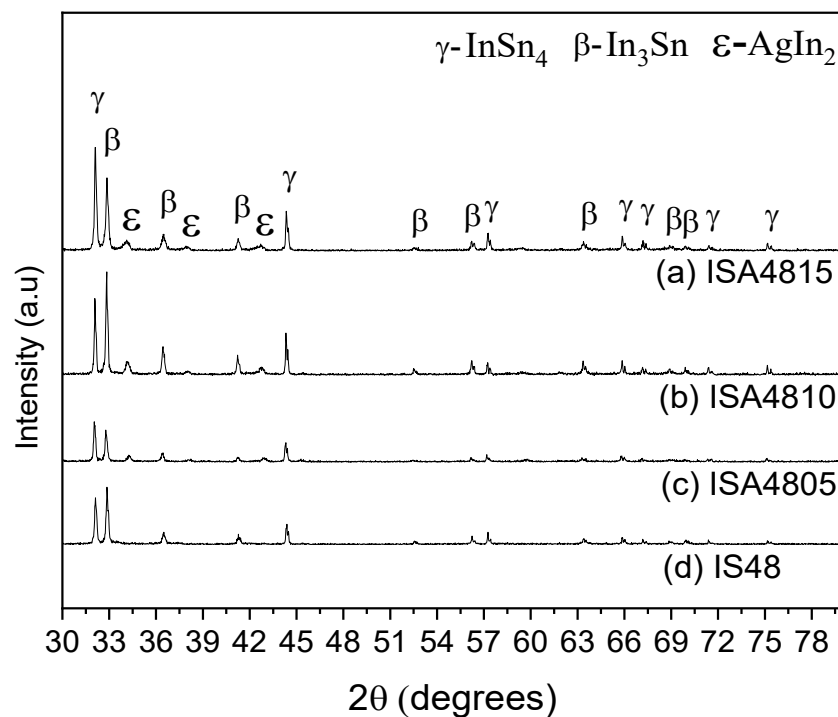
Figure 2.4 XRD Patterns of the various alloys: IS48, ISA4815, ISA4810 and ISA4805.
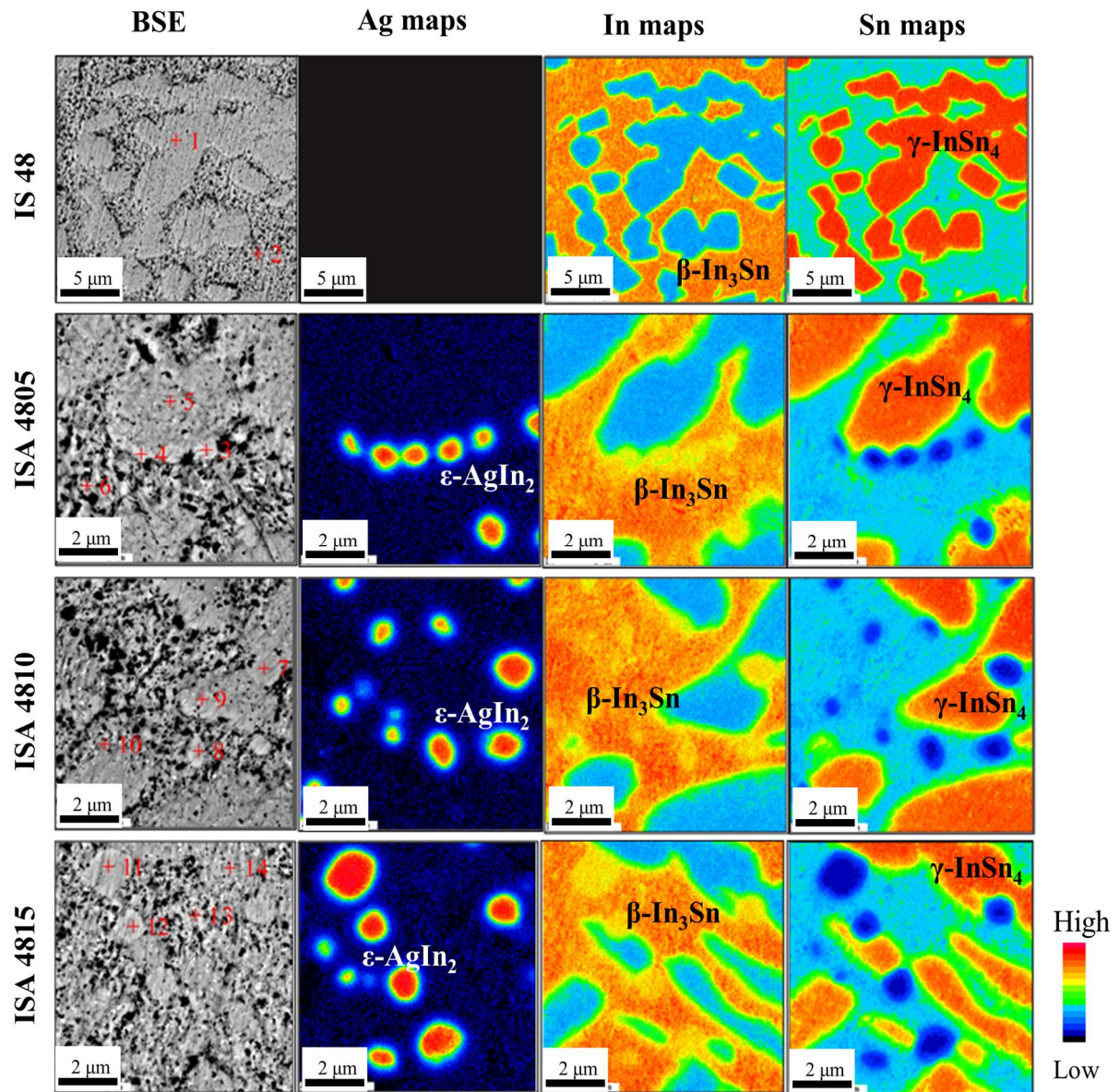
Figure 2.5 EMPA mappings of the In52Sn48, ISA4805, ISA4810, ISA4815 alloys and the locations of EPMA points in **Table 2.2.**

2.3.3 Microstructure

The microstructures of the eutectic In52Sn48 and ISA alloys are displayed in **Figure 2.6**, which shows the two main In-rich β-In$_3$Sn and γ-InSn$_4$ phases in both alloys [5,10]. We measured 50 phases for each alloy then calculated the average phase size. As shown in **Figure 2.7**, the β-In$_3$Sn + ϵ-AgIn$_2$ phases in ISA4815 (135 µm2) are smaller than the β-In$_3$Sn in the eutectic In52Sn48 (270 µm2). Moreover, the average γ-InSn$_4$ phase in the eutectic In52Sn48 is 215 µm2 in size; ISA4805 and ISA4810 have a similar γ-phase of approximately 120 µm2 in size, while the average γ-InSn$_4$ phase in ISA4815 was found to be 300% smaller (65 µm2).

Table 2.2 Elemental compositions of the points in **Figure. 2.5**

Alloys	Point	Ag (at. %)	In (at. %)	Sn (at. %)	Estimated IMC
IS48	1	-	22.73	77.27	γ-InSn$_4$
	2	-	77.40	22.60	β-In$_3$Sn
ISA4805	3	34.45	61.29	4.26	ε-AgIn$_2$
	4	35.88	59.18	4.94	ε-AgIn$_2$
	5	0.49	24.82	74.69	γ-InSn$_4$
	6	0.51	74.62	24.47	β-In$_3$Sn
ISA4810	7	34.83	61.33	3.84	ε-AgIn$_2$
	8	33.91	62.48	3.61	ε-AgIn$_2$
	9	0.74	25.52	73.74	γ-InSn$_4$
	10	1.18	76.80	22.02	β-In$_3$Sn
ISA4815	11	36.91	60.76	2.32	ε-AgIn$_2$
	12	34.79	59.42	5.79	ε-AgIn$_2$
	13	1.60	76.12	22.28	β-In$_3$Sn
	14	1.70	25.12	73.18	γ-InSn$_4$

The β-In$_3$Sn/γ-InSn$_4$ ratio is lowest in alloy IS48 (1.3) and highest in alloy ISA4805 (1.8), followed by alloys ISA4815 (1.65) and ISA4810 (1.59). The sizes of the grains or phases in alloys are usually determined by the number of nucleation sites during solidification. When Ag was added into the eutectic In52Sn48 alloy, the formation of ε-AgIn2 along the phase boundaries created more sites for nucleation during cooling. Therefore, the addition of Ag reduces the sizes of the β and γ-phases, thereby it is expected to effect on the mechanical properties of the ISA alloys.
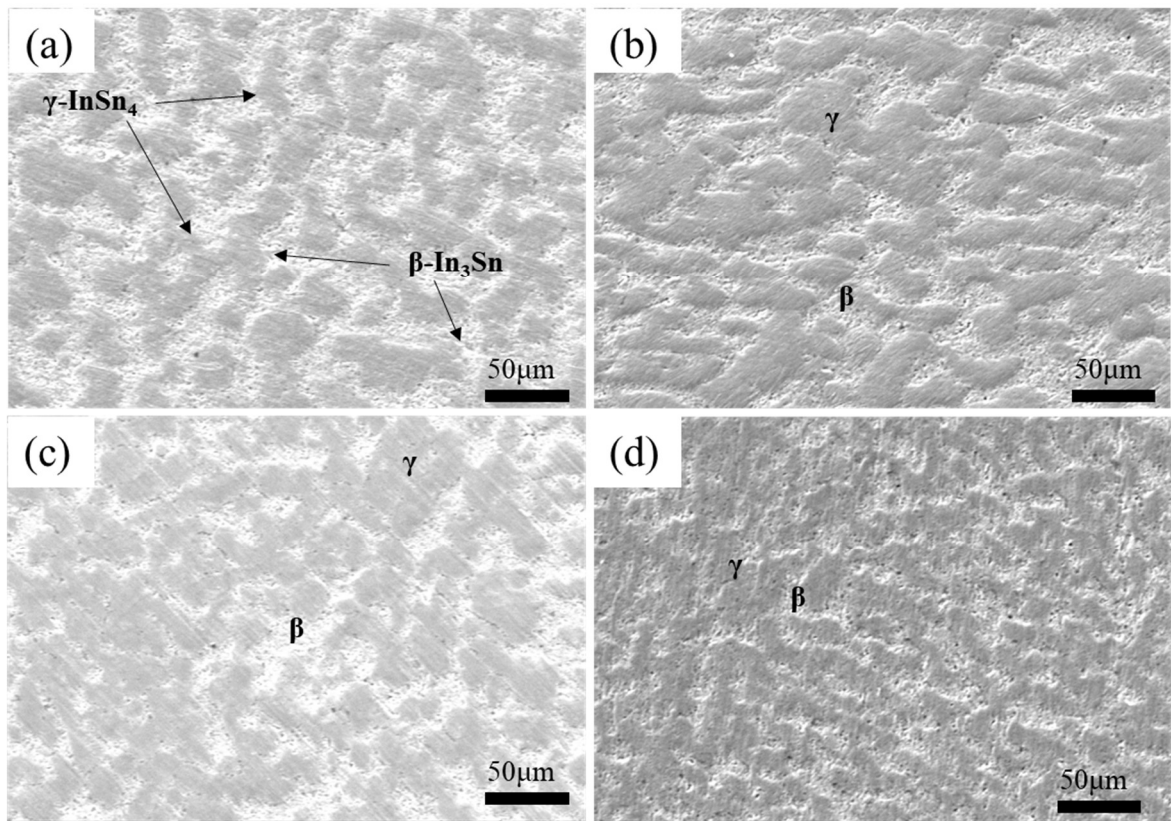
Figure 2.6 SEM image of various alloys: (a) In52Sn48, (b) In52Sn48-0.5Ag, (c) In52Sn48-1Ag, (d) In52Sn48-1.5Ag.
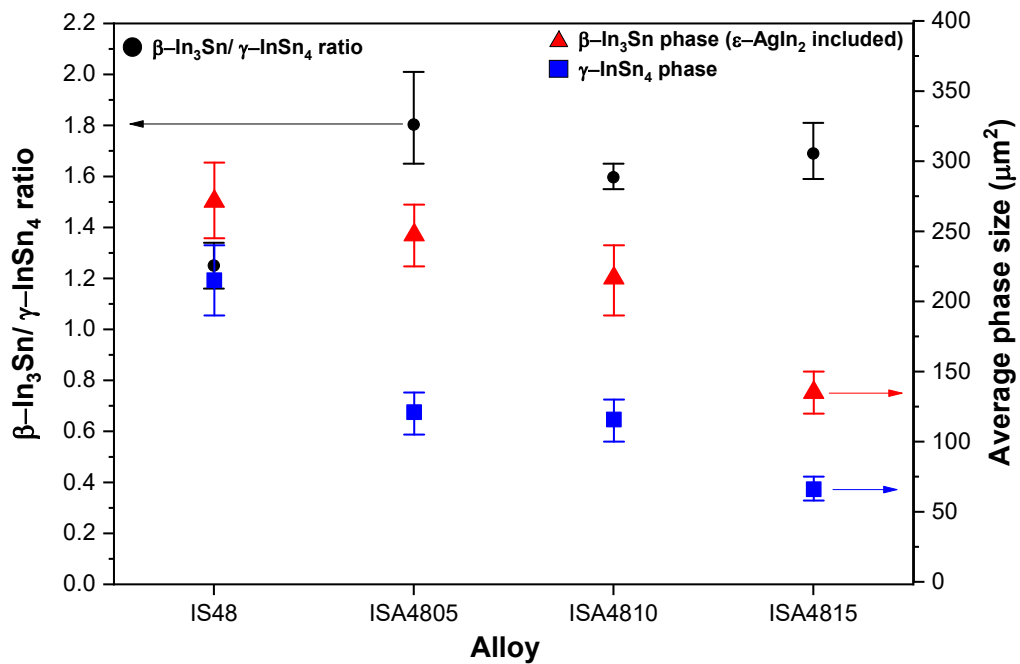
Figure 2.7 Phase calculation and the β-In$_3$Sn/γ-InSn$_4$ ratio in each alloy.

2.3.4 Mechanical properties

Figure 2.8 presents the tensile strength and elongation of IS48, ISA4805, ISA4810, and ISA4815 alloys; the error bar shows the maximum and minimum values, and the dots

are the tensile test values of eight samples for each alloy. The results reveal that the eutectic IS48 and ISA4810 alloys exhibit the same average tensile strength of approximately 10.5 MPa, while ISA4805 exhibits a lower tensile strength of 9.3 MPa, and the ISA4815 alloy exhibits the highest average tensile strength at 12.5 MPa, as shown in **Figure 2.8a**. In addition, the elongation of the new alloys improved with the addition of Ag, as is evident in **Figure 2.8b**, which shows that the ISA4805 alloy has the longest average elongation of 64%, which is twice that of the eutectic In52Sn48 alloy (32%), followed by ISA4810 (52%) and ISA4815 (46%). The new alloys exhibit greater elongation but lower tensile strength compared to the 37.5% and 48.0 MPa, respectively, of the eutectic Sn-58Bi alloy [11]. However, the tensile strength and elongation of IS48 and ISA alloys in this study are both higher than those of near-eutectic In-Sn alloy when adding 1.0-6.0 wt.% Zn (UTS = 4.0-6.0 MPa, EL = 17.0-30.9%) [12].
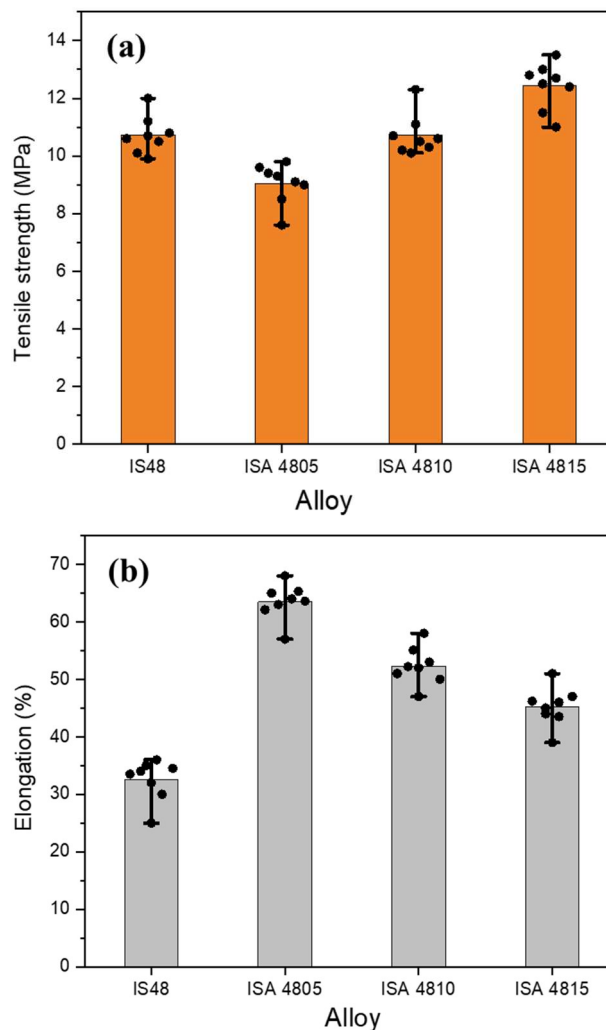
Figure 2.8 Tensile strength (a), and elongation (b) of In52Sn48, ISA4805, ISA4810, ISA4815 alloys.

Generally, the mechanical properties of alloys are determined by the phase composition and microstructure of the alloy [13,14]. The ability of a metal to deform plastically depends on the ability of dislocations to move; by reducing the mobility of dislocations the mechanical strength may be enhanced [15]. The decrease in grain size could affect the dislocation density. A fine microstructure material with a higher total grain boundary area will prevent dislocation motion, and will be stronger than one that is coarse-grained [15,16]. In this study, after the addition of Ag to the IS48 alloy, the microstructure was observed to be smaller in the ISA alloys; in particular, the β and γ phases are smallest in the ISA4815 alloy (with 1.5 wt.% Ag addition), which leads to an increase in the number of grain boundaries. Therefore, the tensile strength of ISA4815 may be enhanced by its significantly smaller phases.

2.3.5 Fracture mode and fracture surface

Figure 2.9 shows typical stress-strain curves of alloys, and images of tensile specimens before and after tensile testing at different magnifications; the maximum stress point and maximum strain in each curve determine the tensile strength and elongation of the alloy, respectively. The stress-strain curve of In52Sn48 is consistent with a typical ductile mode with little plastic deformation; the curve tends to bulge before dropping significantly (**Figure 2.9a**), while the specimen shows a typical brittle mode with planar stress fractures on inclined planes (**Figure 2.9b,c**). We note that the eutectic In52Sn48 exhibits a moderately ductile fracture [5] or semi-ductile behaviour. Conversely, the ISA samples exhibit ductile behaviour with superior strain; the curves transit smoothly and fall slightly with extensional tailing (**Figure 2.9a**). This behaviour is in agreement with the macroscopic fracture morphologies of ISA samples, in which ISA4805 shows extreme elongation with the longest necking region, followed by the ISA4810 and ISA4815 alloys (**Figure 2.9b, d-f**). This alloy behaviour is consistent with the elongation values, as shown in **Figure 2.8b**. Mechanical strength depends on dislocation capacity during plastic deformation [15], and the dislocations that pile up at grain or phase boundaries induce grain boundary strengthening in metals [17]. **Figure 2.10** presents a schematic illustration of dislocation density gradients in large grains and small grains. The grain boundary is weakened in a large grain when a considerable dislocation density gradient exists between the grain interior and the grain boundary, as

shown in **Figure 2.10a** [15]. An intergranular fracture usually occurs in crystals with larger grains because dislocation pileups propagate cracks at the grain boundaries during tensile testing [17]. Conversely, as shown in **Figure 2.10b**, the grain boundaries are not the weakest regions during tensile testing in smaller grains with more uniform dislocation distributions; transgranular fracturing, as opposed to intergranular fracturing, is observed.
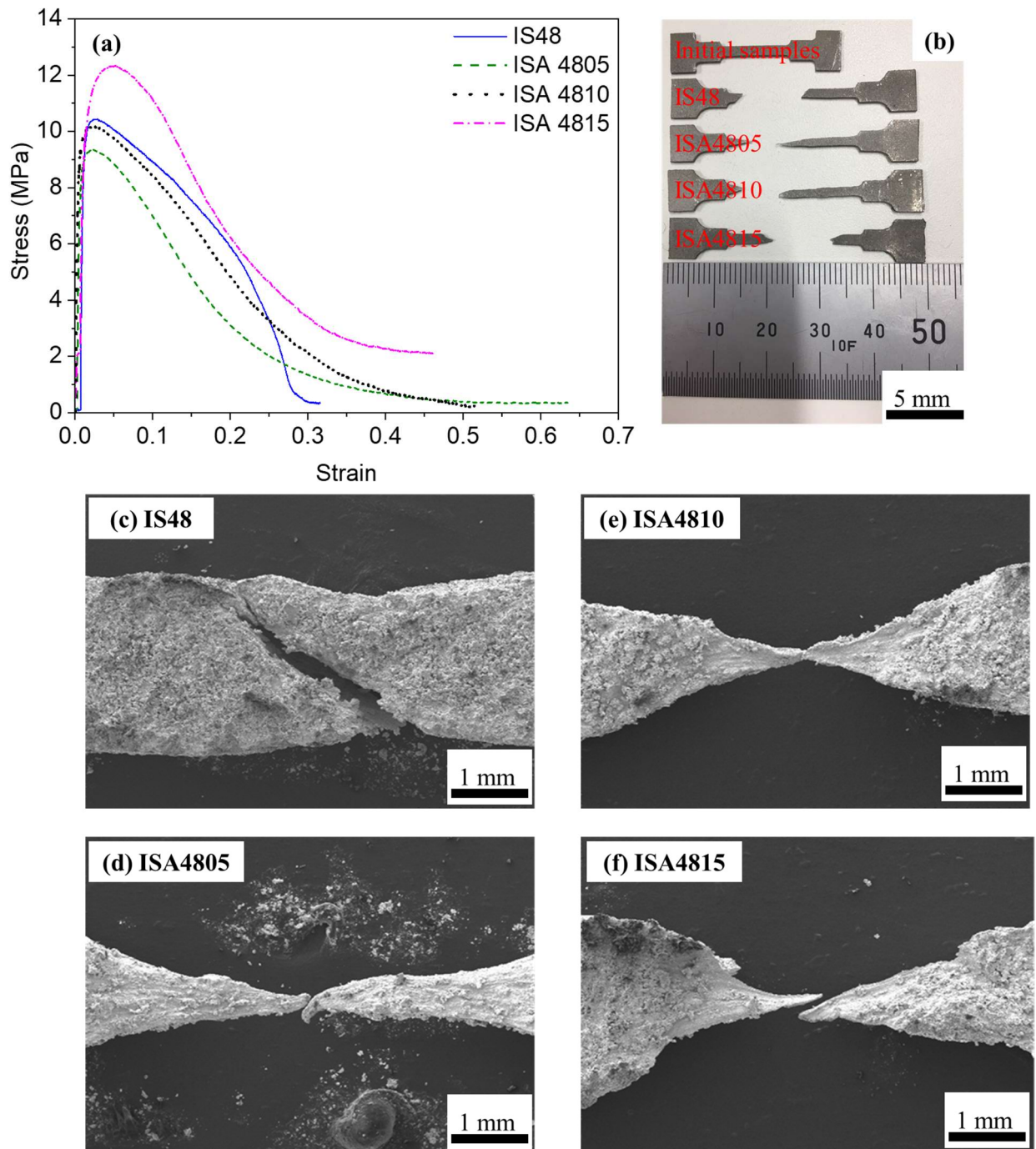
Figure 2.9 Typical stress-strain curves of alloys (a), and (b-f) images of tensile specimens before and after tensile testing at different magnifications.
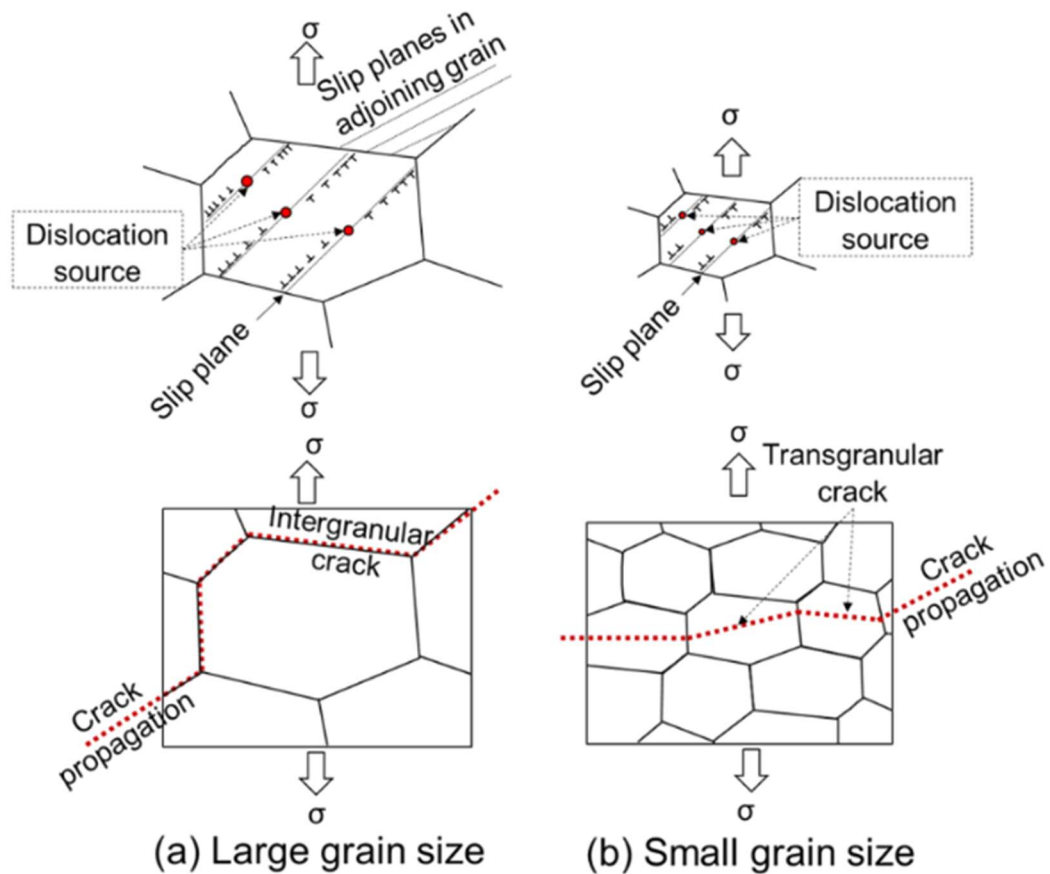
Figure 2.10 Schematic illustration of dislocation-density gradients in (a) large grains and (b) small grains [15].

Fracture images at different magnifications following tensile testing are shown in **Figure 2.11**, with phases determined by energy-dispersive X-ray spectroscopy (EDS); the results are shown in **Table 2.3**. **Figure 2.11d** reveals that the eutectic In52Sn48, with the largest phases, exhibits intergranular fracturing through cleavage along the grain boundaries. Each cracked grain is oriented differently to give a crystalline structure that resembles fractured rock candy [18,19]. The SEM images in **Figure 2.11g-h** and **k-l** reveal that the phases in ISA4805 and ISA4810 are elongated through the grain boundary sliding motion along their tensile axes, as well as by cleavages that lead to grain cracking inside the phase [15]. On the other hand, the ISA4815 alloy, with the smallest phase size (**Figure 2.7**), has the most transgranular fractures with collision areas (**Figure 2.11p-q**) and the highest tensile strength, as shown in **Figure 2.8a.** Moreover, the ISA samples all exhibit better elongation than the eutectic In52Sn48 alloy. In the ISA4805 alloy, the hard γ-InSn$_4$ phase [20] experiences a significant decrease in phase area, while the soft β-In$_3$Sn phase [20] shows a slight size reduction, leading to

the highest β-In$_3$Sn/γ-InSn$_4$ ratio among ISA alloys, as shown in **Figure 2.7**. Further, the ISA4805 alloy, with the smallest Ag content, exhibits the largest grains, while ISA4815, with the highest Ag content, shows the smallest grains among the ISA alloys. In addition, as shown in the EPMA maps in **Figure 2.5**, fewer hard γ-InSn$_4$ regions are observed in ISA alloys; when ε-AgIn$_2$ is formed in β-In$_3$Sn phases due to the consumption of some of the In atoms and near β-In$_3$Sn/γ-InSn$_4$ phase boundaries.
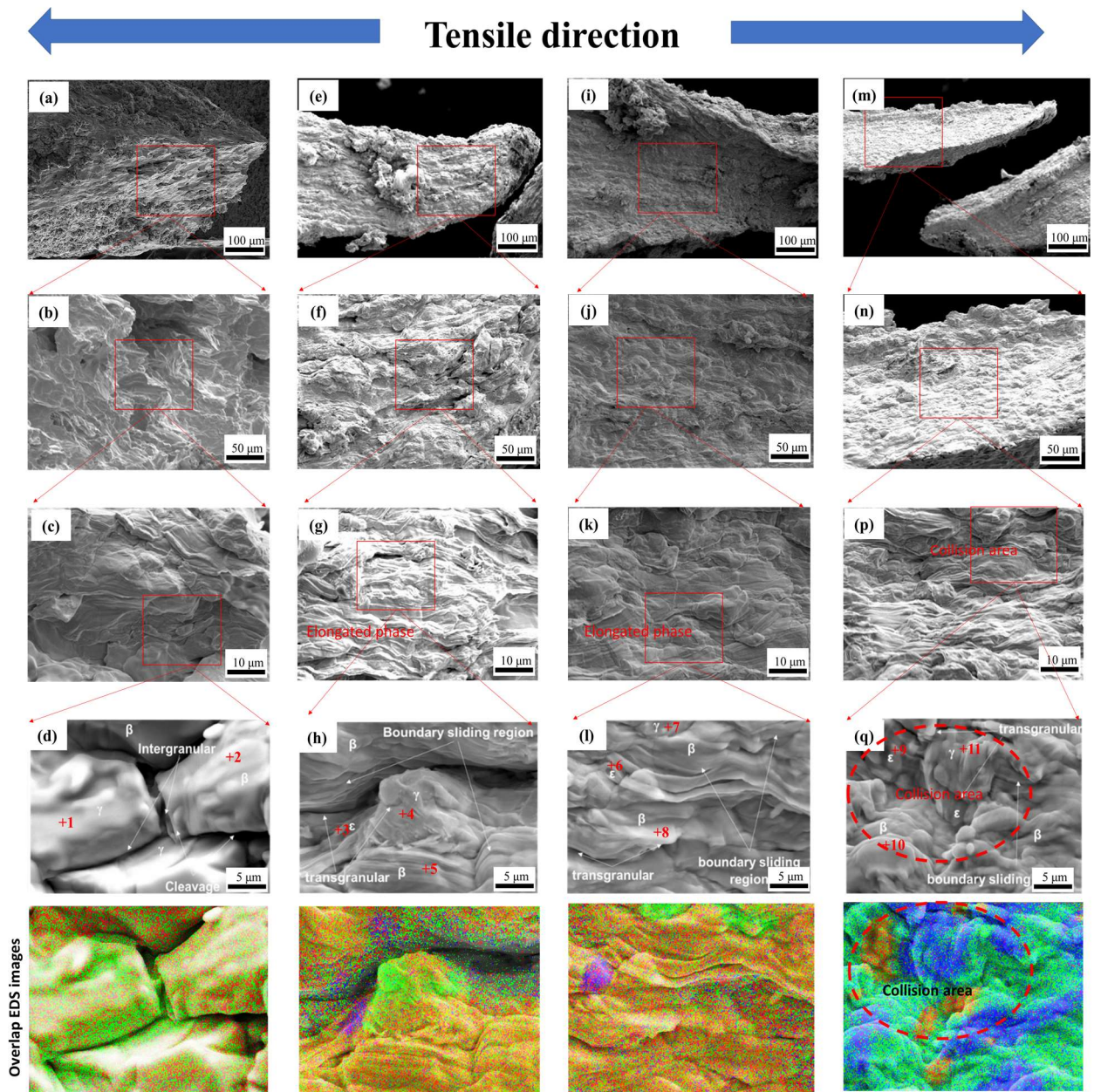
Figure 2.11 Fracture images of (a-d) IS48, (e-h) ISA4805, (i-l) ISA4810 and (m-q) ISA4815 alloys after tensile testing at different magnifications.

Table 2.3 Elemental compositions of the points in **Figure. 2.11.**

Alloys	Point	Ag (at. %)	In (at. %)	Sn (at. %)	Estimated IMC
IS48	1	-	24.69	75.31	γ-InSn$_4$
	2	-	75.25	24.75	β-In$_3$Sn
ISA4805	3	33.47	61.33	5.20	ε-AgIn$_2$
	4	0.26	24.84	74.90	γ-InSn$_4$
	5	0.31	75.30	24.39	β-In$_3$Sn
ISA4810	6	32.63	60.33	7.04	ε-AgIn$_2$
	7	0.95	21.57	77.48	γ-InSn$_4$
	8	1.04	74.64	24.32	β-In$_3$Sn
ISA4815	9	31.80	62.40	5.80	ε-AgIn$_2$
	10	1.43	75.12	23.45	β-In$_3$Sn
	11	1.52	23.27	75.21	γ-InSn$_4$

Although the β-In$_3$Sn regions in the ISA alloys include ε-AgIn$_2$ formation, hardness is mostly dominated by the soft β-In$_3$Sn phases. As mentioned in Chapter 1, the microhardness ($H\mu$) of the β phase ($H\mu$ = 30-40 MPa) is only approximately 1/4 that of the γ phase ($H\mu$ = 126-137 MPa) [20,21]. Accordingly, it is reasonable that ISA4805, with the highest ratio of β-In$_3$Sn/γ-InSn$_4$ and without a large number of small grains or phases for grain boundary strengthening, is the softest of the alloys. Therefore, this study reveals that the addition of Ag not only affects tensile strength, but also elongation of the eutectic In52Sn48 alloy.

2.4 Conclusions

In this chapter, the addition of 0.5-1.5 wt.% Ag not only reduces the melting temperature but also refines the microstructure of the In52Sn48 alloy and affects its mechanical properties. The results may be summarised as follows:

- Due to the ternary eutectic reaction, the fusion start temperature of all the ISA alloys is around 113°C, which is lower than that of the eutectic In52Sn48 alloy (117°C).

- The ε-AgIn$_2$ forms in the β-In$_3$Sn phases and near β-In$_3$Sn/γ-InSn$_4$ boundaries in the ISA alloys following the addition of Ag, which reduces the average area of both β-In$_3$Sn phases and γ-InSn$_4$ phases; these smaller phases enhance tensile strength and alter the fractured mode.

- ISA4815, with the smallest phases, is the strongest of the alloys, with a tensile strength of 12.5 MPa; this alloy fractures in transgranular mode, as commonly seen in crystals with small grains.

- In addition, all the ISA alloys exhibit better elongation than the eutectic In52Sn48 alloy, which is attributable to smaller hard γ-InSn$_4$ regions. Among the alloys, ISA4805, with the highest soft-β-In$_3$Sn/hard-γ-InSn$_4$ ratio and devoid of very small phase sizes, is the softest, with an elongation of 64%.

Therefore, the addition of Ag influences the melting behaviour, microstructures, tensile strength, and elongation of the eutectic In52Sn48 alloy. **Table 2.4** below summarises the results for this chapter.

Table 2.4 Summarized results of chapter 2.

Alloy	Melting temperature (˚C)	Microstructure (β-In$_3$Sn averaged size)	Averages elongation (%)	Averages tensile strength (MPa)
IS48	117.2	270 μm^2	32	10.5
ISA4805	*Reduced* (112.6)	*Refined* (248 μm^2)	*Better* (64)	Slight reduced (9.3)
ISA4810	*Reduced* (112.7)	*Refined* (220 μm^2)	*Better* (52)	Equal (10.5)
ISA4815	*Reduced* (113.2)	*Refined* (135 μm^2)	*Better* (46)	*Better* (12.5)

Reference

1. Kang, H.M.T.S.-B.S.: E. of A. and; Rajendran, S.H.; Jung, J.P. Low Melting Temperature Sn-Bi Solder: Effect of Alloying and Nanoparticle Addition on the Microstructural, Thermal, Interfacial Bonding, and Mechanical Characteristics. *Metals (Basel).* **2021**, *364*, 1–25.

2. Subramanian, K.N. *Lead-free Solders: Materials Reliability for Electronics*; 2012; ISBN 9780470971826.

3. Glazer, J. Metallurgy of low temperature Pb-free solders for electronic assembly. *Int. Mater. Rev.* **1995**, *40*, 65–93, doi:10.1179/imr.1995.40.2.65.

4. El-Bediwi, A.B.; El-Bahay, M.M. Influence of silver on structural, electrical, mechanical and soldering properties of tin-indium based alloys. *Radiat. Eff. Defects Solids* **2004**, *159*, 133–140, doi:10.1080/10420150410001670288.

5. Jones, W.K.; Liu, Y.; Shah, M.; Clarke, R. Mechanical properties of Pb/Sn Pb/In and Sn-In solders. *Solder. Surf. Mt. Technol.* **1997**, 37–41.

6. Ohnuma, I.; Cui, Y.; Liu, X.J.; Inohana, Y.; Ishihara, S. Phase Equilibria of Sn-In Based Micro-Soldering Alloys. *J. Electron. Mater.* **2000**, *29*, 1113–1121, doi:https://doi.org/10.1007/s11664-000-0002-y.

7. Korhonen, T.M.; Kivilahti, J.K. Thermodynamics of the Sn-In-Ag solder system. *J. Electron. Mater.* **1998**, *27*, 149–158, doi:10.1007/s11664-998-0205-1.

8. CHUANG, T.H.; HUANG, Y.T.; L.C.TSAO AgIn2/Ag2In Transformations in an In-49Sn/Ag Soldered Joint under Thermal Aging. *J. Electron. Mater.* **2001**, *30*, 945–950.

9. Meigh, H.J. *Ternary Alloy Systems*; 2019; Vol. 11; ISBN 9783540257776.

10. GOLDSTEIN, J.L.F.; J.W. MORRIS, J. The Effect of Substrate on Microstructure and Creep of Eutectic In-Sn. *Metall. Mater. Trans. Trans. A* **1994**, *323*, 2715–2722, doi:10.1557/PROC-323-159.

11. Zhou, S.; Shen, Y.A.; Uresti, T.; Shunmugasamy, V.C.; Mansoor, B.; Nishikawa, H. Improved mechanical properties induced by In and In & Zn double additions to eutectic Sn58Bi alloy. *J. Mater. Sci. Mater. Electron.* **2019**, *30*, 7423–7434, doi:10.1007/s10854-019-01056-y.

12. Wang, J.; Mao, D.; Shi, L.; Zhang, W.; Zhang, X. Effect of Zinc Addition on the Microstructure, Thermal and Mechanical Properties of Indium-Tin-xZinc Alloys. *J. Electron. Mater.* **2019**, *48*, 817–826, doi:10.1007/s11664-018-6768-6.

13. Cao, H.; Wessén, M. Effect of Microstructure on Mechanical Properties of As-Cast Mg-Al Alloys. *Metall. Mater. Trans. A Phys. Metall. Mater. Sci.* **2004**, *35 A*, 309–319, doi:10.1007/s11661-004-0132-6.

14. Zhang, Z.; Liu, X.; Wang, Z.; Le, Q.; Hu, W.; Bao, L.; Cui, J. Effects of phase composition and content on the microstructures and mechanical properties of high strength Mg-Y-Zn-Zr alloys. *Mater. Des.* **2015**, *88*, 915–923, doi:10.1016/j.matdes.2015.09.087.

15. WILLIAM D. CALLISTER, J.; DAVID G. RETHWISCH *Fundamentals Materials science and Engineering : An Integrated Approach*; 5th ed.; John Wiley & Sons, Inc, 2015; ISBN 978-1-119-17548-3.

16. Sadeghi, B.; Cavaliere, P.; Balog, M.; Pruncu, C.I.; Shabani, A. Microstructure dependent dislocation density evolution in micro-macro rolled Al2O3/Al laminated composite. *Mater. Sci. Eng. A* **2022**, *830*, 142317, doi:10.1016/j.msea.2021.142317.

17. Lu, K.; Lu, L.; Suresh, S. Strengthening materials by boundaries at the nanoscale. *Science (80-.).* **2009**, *349*, 349–353, doi:10.1126/science.1159610.

18. Askeland, D.R.; Fulay, P.P. *Essentials of Materials Science and Engineering*; Gowans, H., Daly, P., Eds.; second.; Cengage Learning: Toronto ON M1K 5G4 Canada, 2009; ISBN 9780495244462.

19. Li, C.; Guangying, Z. Intergranular fracture of low-alloy cast steel. *Mater. Charact.* **1996**, *36*, 65–72, doi:10.1016/1044-5803(95)00255-3.

20. Shepelevich, V.G.; Wang, J. Structure and microhardness of rapidly solidified In-Sn foils. *Inorg. Mater.* **2012**, *48*, 577–581, doi:10.1134/S0020168512050184.

21. Shalaby, R.M.; El-Sayed, M. Effect of heat treatment on the fracture and structure of tin-indium solder alloy. *Radiat. Eff. Defects Solids* **2005**, *160*, 23–31, doi:10.1080/10420150500032473.

Chapter 3

Effect of the addition of Cu on the properties of the In52Sn48 alloy

3.1 Introduction

In Chapter 2, the effect of Ag addition on the elongation of the eutectic In-Sn alloy was discussed, and the results revealed that the addition of 0.5-1.5 wt.% Ag enhances elongation of the In-Sn eutectic alloy; furthermore, tensile strength was improved with 1.5 wt.% Ag. As mentioned, Cu is the second element selected to be added to the In52Sn48 eutectic alloy to improve its properties. Despite several previous studies [1–5], the effect of Cu on the mechanical properties of the eutectic In-Sn alloy is not fully understood, especially the relationship between the microstructure of the alloy and its mechanical properties. Therefore, this chapter demonstrates the effects of various Cu concentrations (1.0 wt.%, 2.0 wt.%, and 8.0 wt.%) on the melting behaviour, microstructure, tensile strength, and elongation of the eutectic In52Sn48 alloy. The mechanisms, and relationship between microstructure, fracture mode, and mechanical properties, are also discussed.

3.2 Experimental procedure

3.2.1 Fabrication

In-Sn-Cu (ISC) alloys comprising eutectic In52Sn48 solder and 1.0, 2.0, and 8.0 wt.% Cu (99.8%; Nilaco Corporation, Japan) were alloyed in an electric furnace (HPM-ON, AS ONE) under nitrogen atmosphere at 700ºC for 5 h. The experimental procedure was the same as shown in **Figure 2.1** in Chapter 2. The alloy bar was cast in a steel mould and naturally cooled in air. The chemical composition of the In-Sn eutectic and new ISC alloys was analysed using a wet chemical titrimetric method (for Sn analysis) and an ICP for the other elements; the results are summarised in **Table 3.1.** Subsequently, for the tensile test, the bars were machined into a dog-bone shape by wire electric discharge machining (Soldick AG 360L, Japan); the dimensions of the samples are shown in **Figure 3.1.**

3.2.2 Characterisation methods

DSC (DSC7020, Hitachi, Japan) was used to investigate the melting behaviour of the ISC alloys during heating and cooling in the range of 50 to 550ºC at a heating and cooling rate of 5ºC/min under a constant flow of N_2 atmosphere. The crystal structure of each phase in the alloys was determined by XRD (Ultima IV, Rigaku, Japan) in the 2θ range of 30-80º
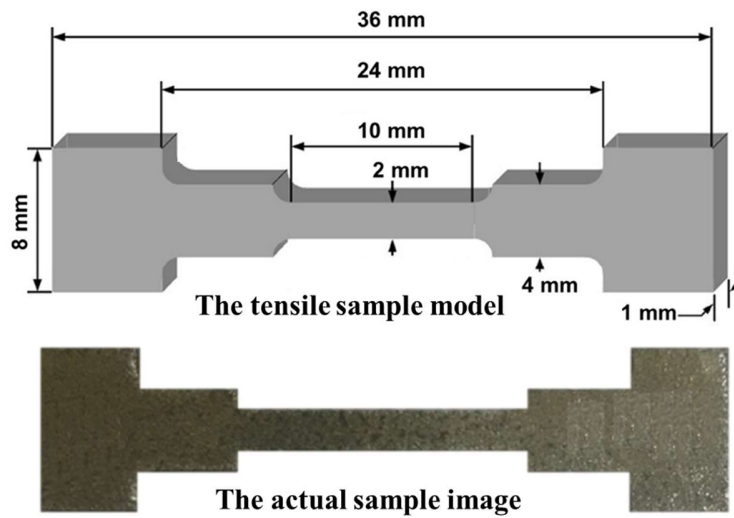
Figure 3.1 Tensile test specimen.

at a scan rate of 1°/min. The tensile strength of the ISC alloys was measured using a universal tensile machine (Autograph AG-X, Shimadzu, Japan) at a strain rate of 5×10^{-4} s^{-1}. The average elongation (EL) and UTS were determined from tensile stress-strain curves and calculated based on the tensile results of eight test pieces for each alloy. SEM (SU-70, Hitachi, Japan) was used to examine the fracture surfaces of the alloys after the tensile test. To investigate the microstructure of the alloys, the samples were polished with SiC grit papers #150, #400, #800, #1200, and #2000, after which fine polishing was performed with a 1.0 μm alumina suspension (Buehler, USA). The surface polishing process was carried out as described in detail in Section 2.2.2 of Chapter 2. Then, the samples were analysed by SEM. Field-emission electron probe microanalysis (FE-EPMA; JXA-8530F JEOL, Japan) was used to identify the elemental distributions of the alloys. ImageJ software was used to measure the fractions of the phases shown in EPMA images for each alloy. A total of 50 phases for each alloy were measured and used to calculate the average phase size.

3.3 Results and discussion

3.3.1 Melting behaviour and solidification process

Figure 3.2 shows the DSC curves of the In52Sn48 (IS48), In52Sn48-1.0Cu (ISC481), In52Sn48-2.0Cu (ISC482), and In52Sn48-8.0Cu (ISC488) alloys. **Figure 3.2a** displays the DSC curves of the eutectic In-Sn and ICS alloys, demonstrating the melting

Table 3.1 Chemical compositions of the eutectic In52Sn48 and In-Sn-xCu alloys (x =1.0, 2.0, 8.0 wt.%).

Element	In52Sn48-1.0Cu (ISC481), *wt. %*	In52Sn48-2.0Cu (ISC482), *wt. %*	In52Sn48-8.0Cu (ISC488), *wt. %*	In52Sn48 (IS48), *wt. %*
Sn	47.970	47.720	45.000	48.200
In	Balance	Balance	Balance	Balance
Cu	0.803	1.530	7.370	0.003
Ni	0.001	0.001	0.001	0.001
Bi	-	-	-	0.02
Pb	0.001	0.001	0.001	0.001

behaviours of the alloys during the heating process at a heating rate of 5ºC/min. As shown in the inset representing an enlarged image of region A, although the onset melting temperatures ($T_{onset-endo}$) of the ISC481 (114.6ºC), ISC482 (114.7ºC), and ISC488 (114.8ºC) alloys were slightly higher than that of the In52Sn48 alloy (114.4ºC), they were all close to 115ºC, indicating that the addition of Cu has no significant effect on the melting temperature of the eutectic In-Sn alloy. **Figure 3.2b** shows the main solidification and crystallisation of the phases in the eutectic In52Sn48 and ISC alloys during the cooling process at a cooling rate of 5ºC/min. In the large-scale B region, small peaks were observed in the DSC curves of the ISC488 (390ºC), ISC482 (310ºC), and ISC481 (280ºC) alloys, which can be ascribed to the phase precipitation of η-(Cu,In,Sn). These results are consistent with the calculation of Liu et al. [3] and the experiment of Riani et al. [5]. Furthermore, the solidification of the precipitated phases increases with an increase in Cu content. Therefore, phase precipitation did not occur in the In52Sn48 alloy. Moreover, the eutectic solidification of the β-(In,Sn) and γ-(In,Sn) phases occurred in the eutectic In-Sn alloy between 113ºC and 115ºC, whereas solidification occurred between 111ºC and 114ºC in the ISC alloys.
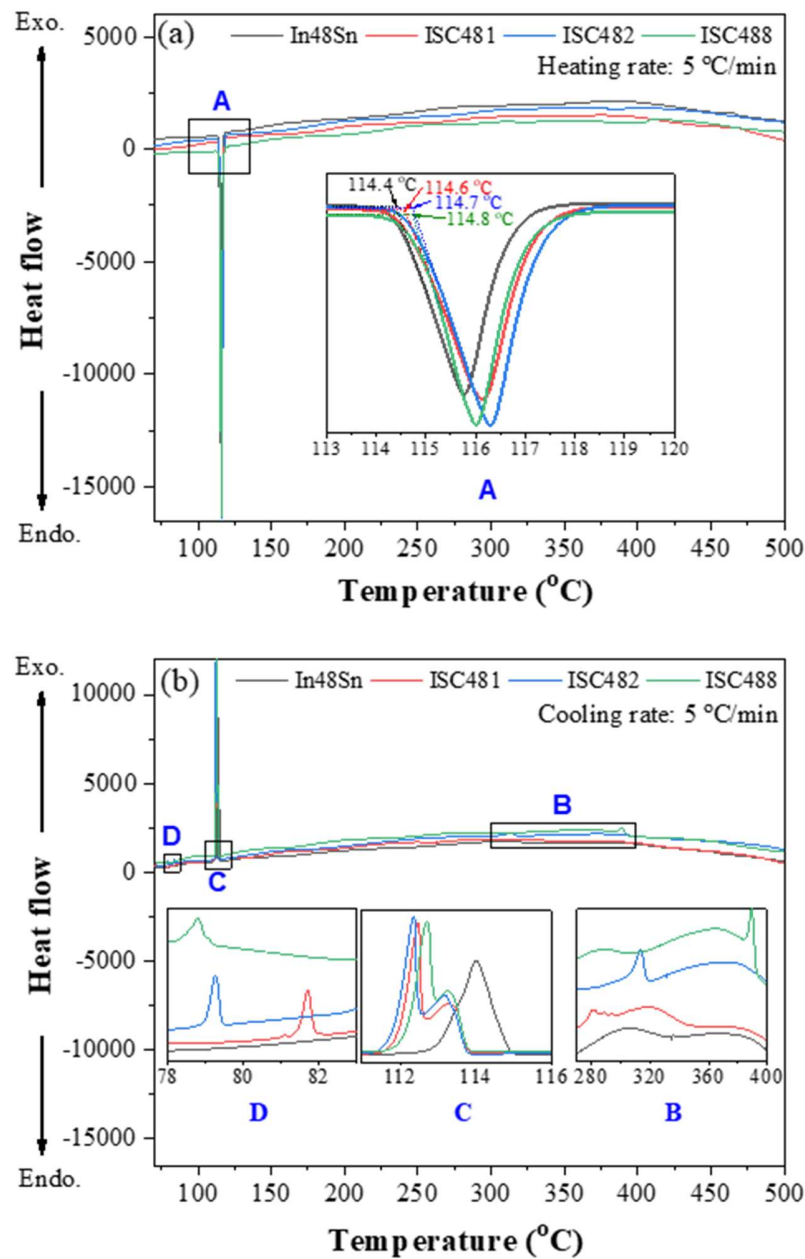
Figure 3.2 DSC curves of the (a) heating process and (b) the cooling process of the IS48, ISC481, ISC482, and ISC488 alloys.

The difference in the solidification temperature can be attributed to the occurrence of a ternary reaction in the ISC alloy between 111ºC and 116.8ºC, which can be represented using Equation (1) [5]. Additionally, a mushy zone was observed in the enlarged image of the C region of the DSC curves (**Figure 3.2b**) of the ISC alloys, as evidenced by the two

peaks in the curve, which can be attributed to the reduction in the In content in the alloys due to the addition of Cu.

$$L \leftrightarrow \gamma \text{ (In,Sn)} + \beta \text{ (In,Sn)} + \eta \text{ (Cu,In,Sn)} \tag{1}$$
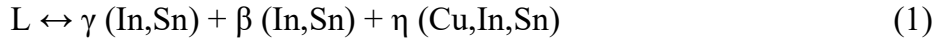
Finally, in the 78ºC to 83ºC region, the DSC curves of the ISC alloys exhibit third peaks, as shown in the enlarged image of the D region in **Figure 3.2b**. This can be attributed to the solid state phase transformation of the η-(Cu,In,Sn) into τ-Cu(In,Sn)$_2$ phase [1,5] through invariant equilibria, as shown in Equation (2).

$$\eta \text{ (Cu,In,Sn)} + \beta \text{ (In,Sn)} \leftrightarrow \gamma \text{ (In,Sn)} + \tau\text{-Cu(In,Sn)}_2 \tag{2}$$
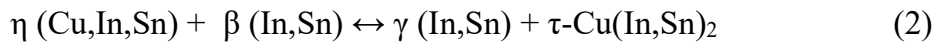
In this study, although the Cu content in Cu-In-Sn alloys is 1.0-8.0 mass.%, the solidification of ISC481, ISC482, and ISC488 alloys during cooling is consistent with vertical section at 10 mass% Cu of Cu-In-Sn ternary system, as shown in **Figure 3.3** [6].
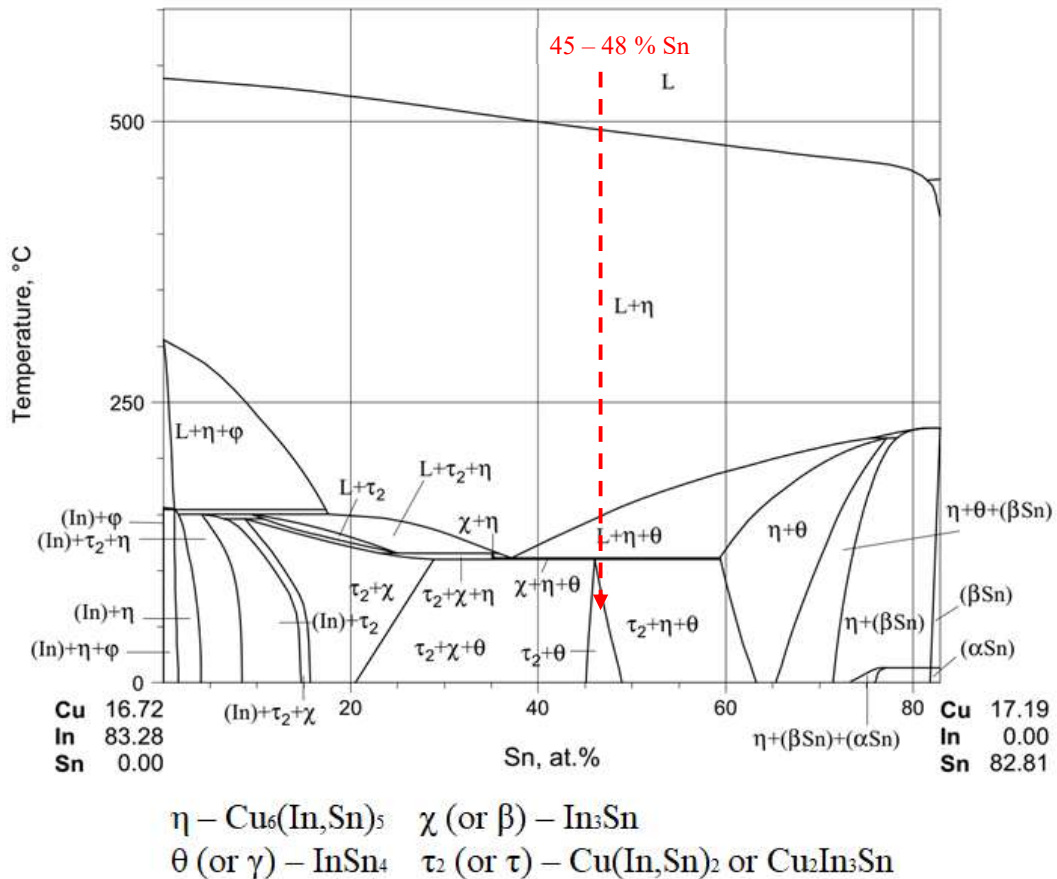
Figure 3.3 Vertical section at 10 mass% Cu of Cu-In-Sn ternary system, plotted in at.% [6].

3.3.2 Microstructure

Figure 3.4 shows the SEM images of the microstructures of the In52Sn48 and ISC alloys. Here, the SEM samples were selected from the middle section of the alloyed bars, and the eutectic spacing in each alloy was measured using ImageJ software. In this chapter, eutectic spacing is the distance between two consecutive lamellae of the γ-InSn4 phase [7], and the average values are calculated based on the measured results of 60 eutectic spacings for each alloy. The rough and smooth regions in the SEM image of the In52Sn48 alloy represent the soft β-In3Sn phase and the hard γ-InSn4 phase in the In52Sn48 alloy [8–10], respectively (**Figure 3.4**). As shown in **Figure 3.4(b-d)**, the β-matrix of the ISC alloys is composed of continuous regions comprising the η-(Cu,In,Sn) and τ-Cu(In,Sn)$_2$ phases [1]. We note that the grain size in the β and γ matrix in the ISC alloys is smaller than that of the eutectic alloys. In other words, the microstructure of ISC alloys is refined, and the refinement degree is specified by the eutectic spacing [11], as shown in **Figure 3.5**.
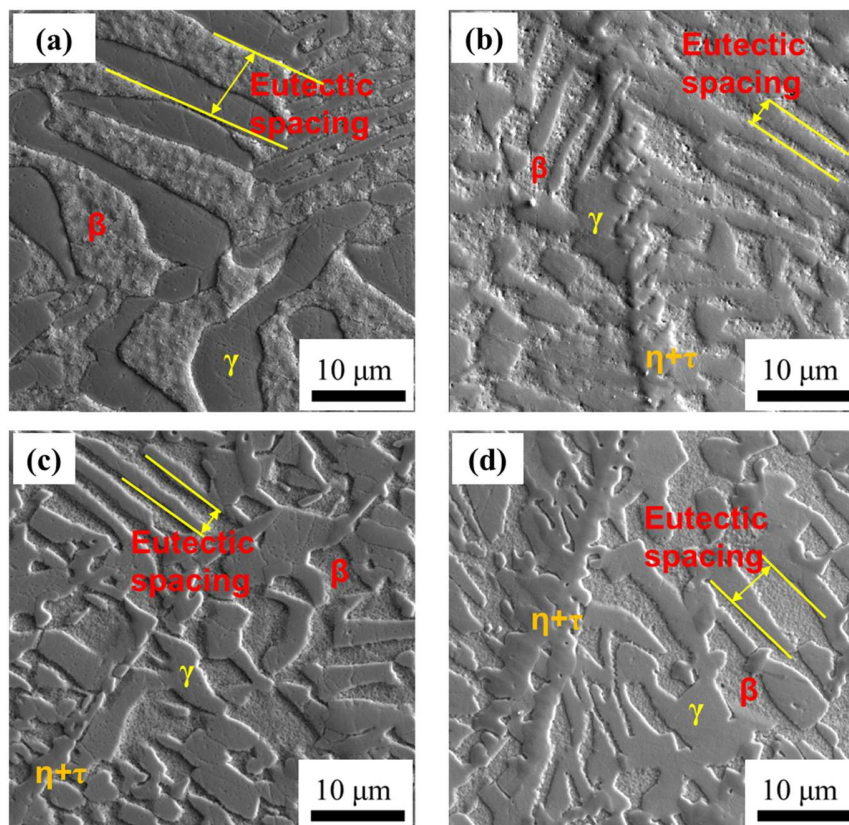
Figure 3.4 SEM images of the various alloys: (a) In52Sn48, (b) In-Sn-1.0Cu, (c) In-Sn-2.0Cu, (d) In-Sn-8.0Cu.
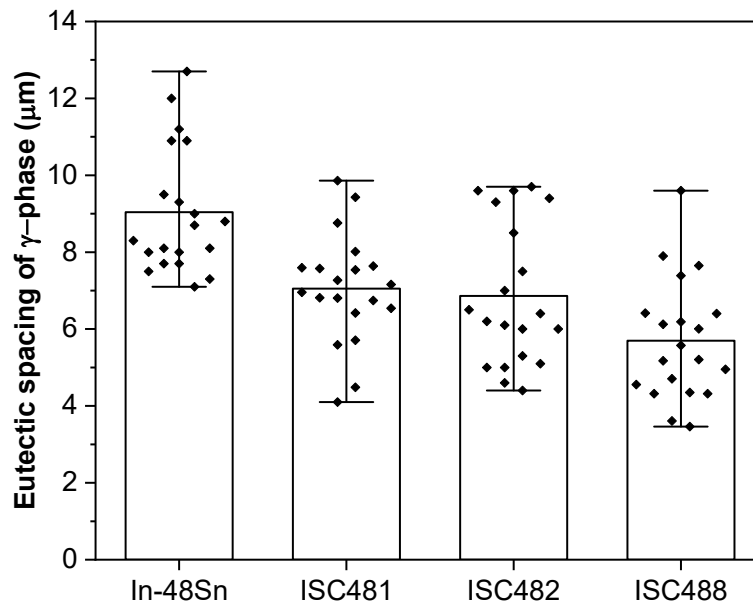
Figure 3.5 Eutectic spacing of IS48, ISC481, ISC482, and ISC488 alloys.

The ISC481 alloy with the smallest amount of Cu added has the highest eutectic spacing (7.1 μm), which is smaller than that of the In52Sn48 eutectic alloy (9.1 μm), followed by the ISC482 (6.8 μm) and ISC488 (5.6 μm) alloys. The finer microstructure in ISC alloys can be attributed to the presence of Cu atoms in molten alloys. As Cu has a higher melting temperature than In and Sn, it could act as a heterogeneous nucleation site during the solidification process. Thus, with increasing Cu doping, the numbers of grains and grain boundaries increase, leading to a more refined microstructure in the ISC alloys.

Although the boundaries between the η-(Cu,In,Sn) and τ-Cu(In,Sn)$_2$ phases could barely be distinguished in the SEM images, these phases could be identified by EPMA mapping, as shown in **Figure 3.6**. Herein, **Figure 3.6a-b** displays the EPMA maps of the In52Sn48 alloy with only In and Sn elemental distributions. A significant distribution of the η-(Cu,In,Sn) and τ-Cu(In,Sn)$_2$ phases in the ISC alloys is distinguished by the Cu elemental distributions in the ISC alloys, as shown in **Figures 3.6g,k,o**. Due to a partial phase transformation of the η-(Cu,In,Sn) phase into the τ-Cu(In,Sn)$_2$ phase, the latter (In-rich) surrounds the former (Cu-rich), with both phases embedded in the β-In$_3$Sn matrix, owing to the consumption of Cu diffusion [12] by the neighbouring β-phase [4] during cooling below 90°C, as described by Equation (2). **Table 3.2** lists the elemental

compositions at each marked point on the EPMA maps in **Figure 3.6**. The IMC η-$Cu_6(In,Sn)_5$ and τ-$Cu(In,Sn)_2$ phases observed by the EPMA mapping are consistent with the aforementioned DSC results. Additionally, **Figure 3.7** presents the XRD patterns of the In52Sn48 and ISC alloys. The γ-$InSn_4$ and β-In_3Sn phases were detected in the In52Sn48 and ISC alloys [9,13], whereas the ternary IMC phases were only observed in the ISC alloys, which is consistent with the findings of previous studies [14,15].
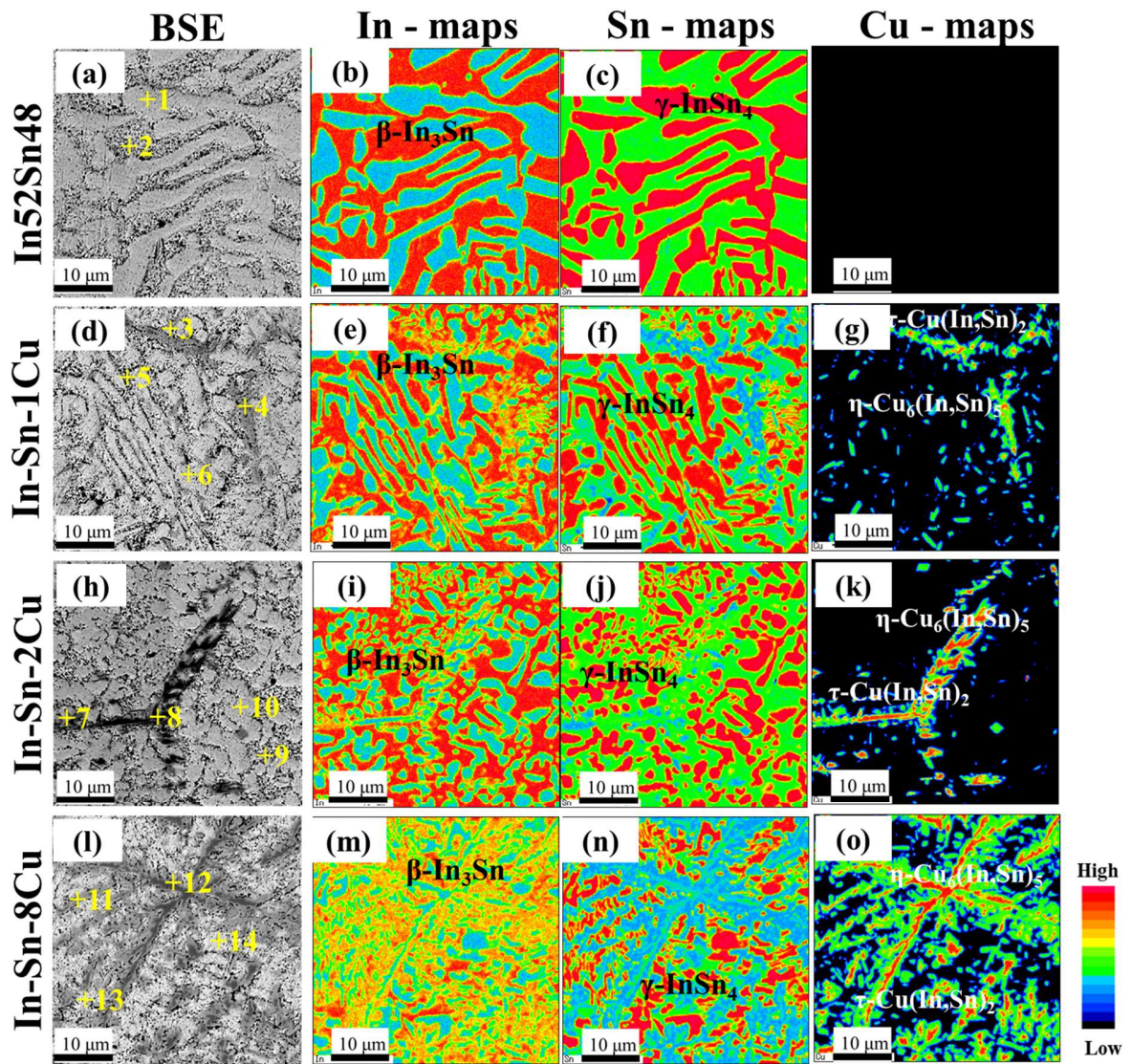
Figure 3.6 EPMA maps of the (a-c) In52Sn48, (d-g) In-Sn-1.0Cu, (h-k) In-Sn-2.0Cu, and (l-o) In-Sn-8.0Cu alloys and the locations of the EPMA points listed in **Table 3.2.**

Table 3.2 Elemental composition of the points highlighted in **Figure 3.6.**

Alloys	Point	Cu (at. %)	In (at. %)	Sn (at. %)	Estimated IMC
IS48	1	-	24.79	75.21	γ-InSn$_4$
	2	-	77.38	22.62	β-In$_3$Sn
ISC481	3	30.90	54.68	14.42	τ-Cu(In,Sn)$_2$
	4	53.53	21.60	24.87	η-Cu$_6$(In,Sn)$_5$
	5	0.04	76.80	23.16	β-In$_3$Sn
	6	0.85	27.53	71.62	γ-InSn$_4$
ISC482	7	27.76	56.83	15.41	τ-Cu(In,Sn)$_2$
	8	54.89	19.39	25.72	η-Cu$_6$(In,Sn)$_5$
	9	0.58	76.71	22.71	β-In$_3$Sn
	10	0.10	25.03	74.87	γ-InSn$_4$
ISC488	11	31.91	53.93	14.15	τ-Cu(In,Sn)$_2$
	12	59.19	21.74	19.07	η-Cu$_6$(In,Sn)$_5$
	13	0.13	74.58	25.28	β-In$_3$Sn
	14	0.63	25.64	73.73	γ-InSn$_4$

Furthermore, the peak intensity of the η-Cu$_6$(In,Sn)$_5$ and τ-Cu(In,Sn)$_2$ phases is weak in the ISC481 alloy and increases with the addition of 8 wt.% Cu, which is consistent with the distribution of these phases in the EPMA Cu-maps shown in **Figures 3.6g,k,o**. This indicates that the precipitation of the η-Cu$_6$(In,Sn)$_5$ and τ-Cu(In,Sn)$_2$ phases increases with an increase in the Cu concentration. **Figure 3.8** displays the phase fraction in the In52Sn48 and ISC alloys. The size of the minimum measured area from EPMA images using ImageJ software is 1.2 μm^2. Remarkably, the soft β-In$_3$Sn phase was found to be dominant in all the alloys. Also, the β-phase fraction increased from 55% in the In52Sn48 alloy to approximately 59% in the ISC481 alloy and reduced to 53% in ISC482 and 31% in ISC488.

Furthermore, the γ-InSn₄ fraction decreases with the addition of Cu. The γ-phase fraction decreased from 44% in the In52Sn48 alloy to 31% in the ISC488 alloy, which had the smallest γ-phase fraction among the ISC alloys.
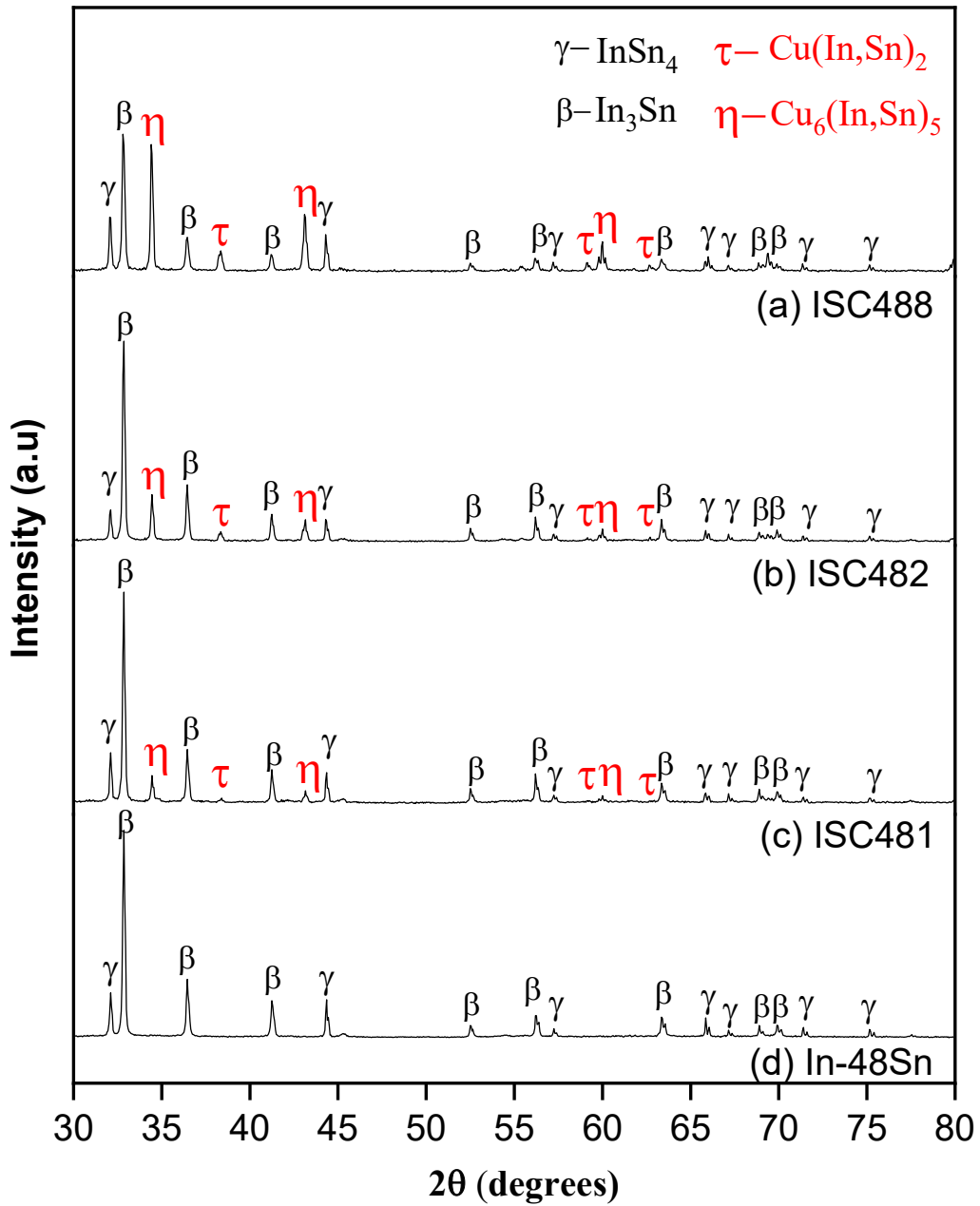
Figure 3.7 XRD patterns of the (a) ISC488, (b) ISC482, (c) ISC481, and (d) IS48 alloys.
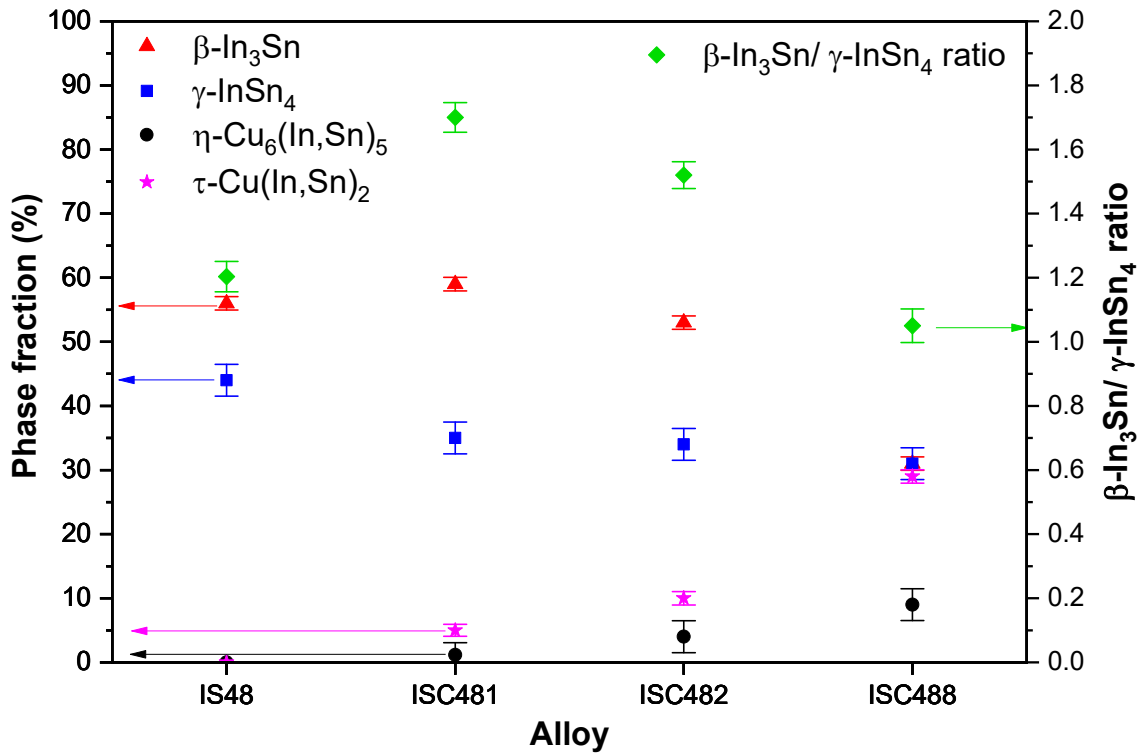
Figure 3.8 Phase fractions (left side) and β/γ ratios (right side) of the IS48, ISC481, ISC482, and ISC488 alloys.

In the In-Sn-Cu ternary system, the η-phase continuously exists from the Cu-In to the Cu-Sn system at high temperatures [3,4]. β-Sn with a higher melting temperature is dominant in the reaction with Cu and In, forming η-(Cu,In,Sn) and γ-(In,Sn) during solidification, which is consistent with the thermodynamic modeling result of the In-Sn-Cu ternary system by Riani and coworkers [5], and can be expressed as Equation (3). Consequently, Sn is partly consumed to form the η-(Cu,In,Sn) phase, and the remaining Sn reacts with In to form the γ-phase, which reduces the γ-InSn$_4$ fraction in ISC alloys compared with the eutectic In52Sn48 alloy.

$$L + \beta\text{-Sn} \leftrightarrow \eta\text{-(Cu,In,Sn)} + \gamma\text{-(In,Sn)}. \tag{3}$$
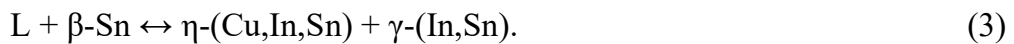
As previously discussed in Section 3.3.1, during the cooling process at temperatures below 90ºC, Cu atoms in the η (Cu-rich) phase slowly diffuse toward the β (In-rich) phase in the alloy matrix, which is then transformed to τ-Cu(In,Sn)$_2$ (Eq.(2)) [1,4,5,12], thereby reducing the β-In$_3$Sn fraction and increasing the τ-phase fraction. It is important to note that

due to the limited time available for the η-$Cu_6(In,Sn)_5$ phase to fully transform into the τ-$Cu(In,Sn)_2$ phase, a small amount of the η-$Cu_6(In,Sn)_5$ remains in the ISC481 (1%), ISC482 (4%), and ISC488 (9%) alloys. These results reveal that the addition of Cu to the In52Sn48 alloy has a significant effect on its microstructure and the fraction of each phase, which indicates that the mechanical properties of the ISC alloys differ from those of the eutectic In52Sn48 solder.

3.3.3 Mechanical properties

Figure 3.9 shows a chart demonstrating a typical engineering stress–strain curves of IS48, ISC481, ISC482, and ISC488 alloys, in which consists of an elastic region and a plastic region. In the elastic region, the engineering stress is linear, with the engineering strain conforming to Hooke's law as follows [16]:

$$E = \sigma/\varepsilon \tag{4}$$

Here, E is the elastic modulus, which can be determined from the slope of the elastic portion of the stress–strain curve, σ is the engineering stress, and ε is the engineering strain. We calculated that the elastic modulus of IS48, ISC481, ISC482 and ISC488 alloys are 24.1, 23.2, 25.1, and 26.9 GPa, respectively. The elastic modulus of IS48 is in agreement with the value reported by Kim [17]. All alloys exhibits a low elastic modulus compared to that of commercial SAC305 alloy (54.0 GPa) [18] and Sn-58Bi alloy (41.3 GPa) [19]. This is an advantage of IS48, ISC482, and ISC488 alloys to be able to apply in flexible electronic devices. Moreover, the tensile strength of ISC alloys increases with the increase of Cu content, which is expected that Cu addition can help improve the creep resistance and thermal failure resistance of the ISC alloys.

Figure 3.10 shows the average tensile strength and elongation of the In52Sn48 and ISC alloys; the error bar displays the maximum and minimum deviation, and the dots represent ten measured values for each alloy. The In52Sn48 and ISC482 alloys exhibit a similar strength of approximately 11.0 MPa, which is higher than that of the ISC481 alloy (~9.0 MPa), with the ISC488 alloy exhibiting the highest tensile strength of approximately 17.0 MPa. Also, the elongation of the ISC alloys improves with the addition of Cu, with

the ISC481 demonstrating the highest elongation of 74%, which is approximately two times that of the In52Sn48 alloy (32%); elongation for the ISC482 and ISC488 alloys was 55% and 37%, respectively. The result of mechanical property of IS48 alloy in this study are compatible with tensile strength of In52Sn48 alloy in other reports (UTS = 8.0-11.5 MPa) [20–22]. Previous studies have reported that the mechanical properties of alloys can be determined from their microstructures, such as grain size and the fraction of each phase [9,23–25]. **Figure 3.8** demonstrates that the ISC481 alloy exhibits the highest soft β/hard γ ratio; the order of β/γ among the alloys is ISC481 (1.7) > ISC482 (1.5) > In52Sn48 (1.2), which coincides with the order of their elongation. In contrast, although the ISC488 alloy has the lowest ratio of β/γ (1.0), the In52Sn48 alloy has 1.42 times more hard γ-phase (44%) than the ISC488 alloy (31%), implying that the hardness of these alloys is dominated by the hard γ-phase. As a result, the ISC488 alloy containing the smallest amount of hard γ phase is softer, and exhibits better elongation than the In52Sn48 alloy. The relationship between mechanical properties and the β/γ ratio is shown in **Figure 3.11**.
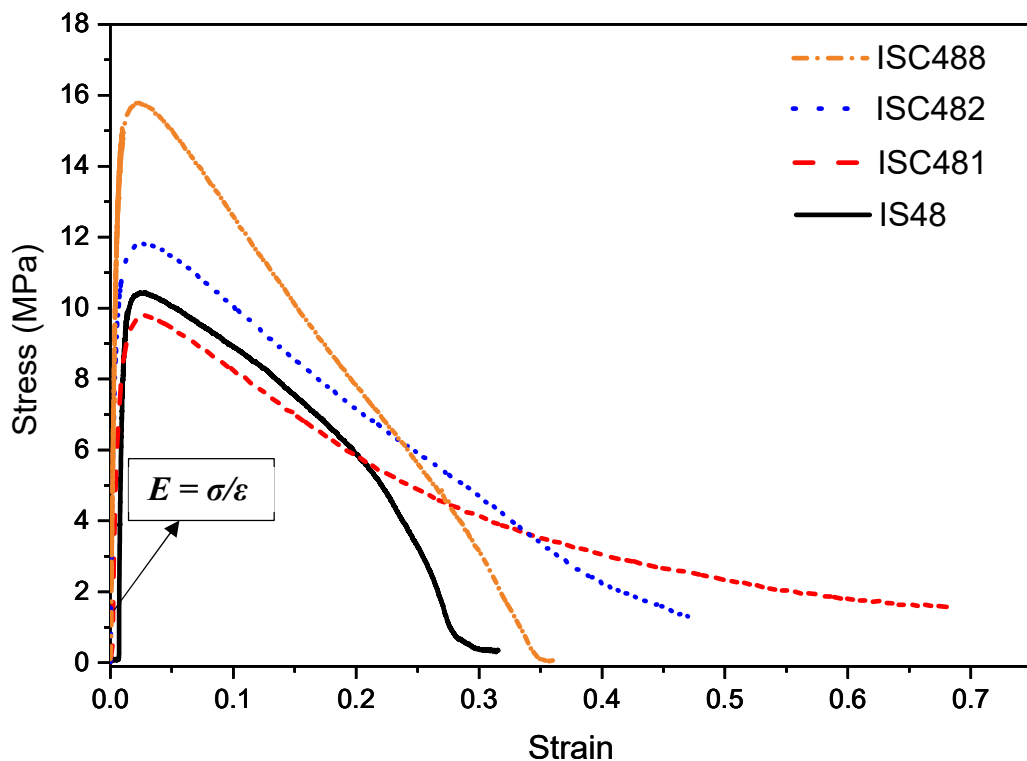
Figure 3.9 Representative stress-strain curves of the IS48, ISC481, ISC482, and ISC488 alloys.
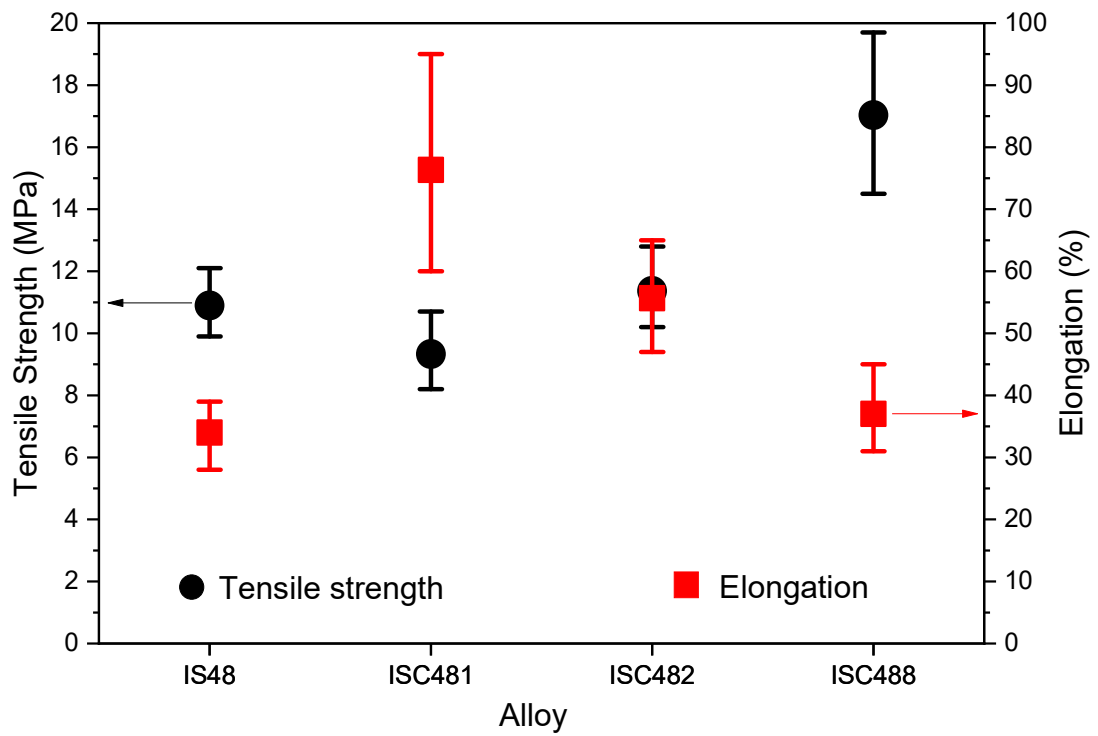
Figure 3.10 Mechanical properties of the IS48, ISC481, ISC482, and ISC488 alloys.
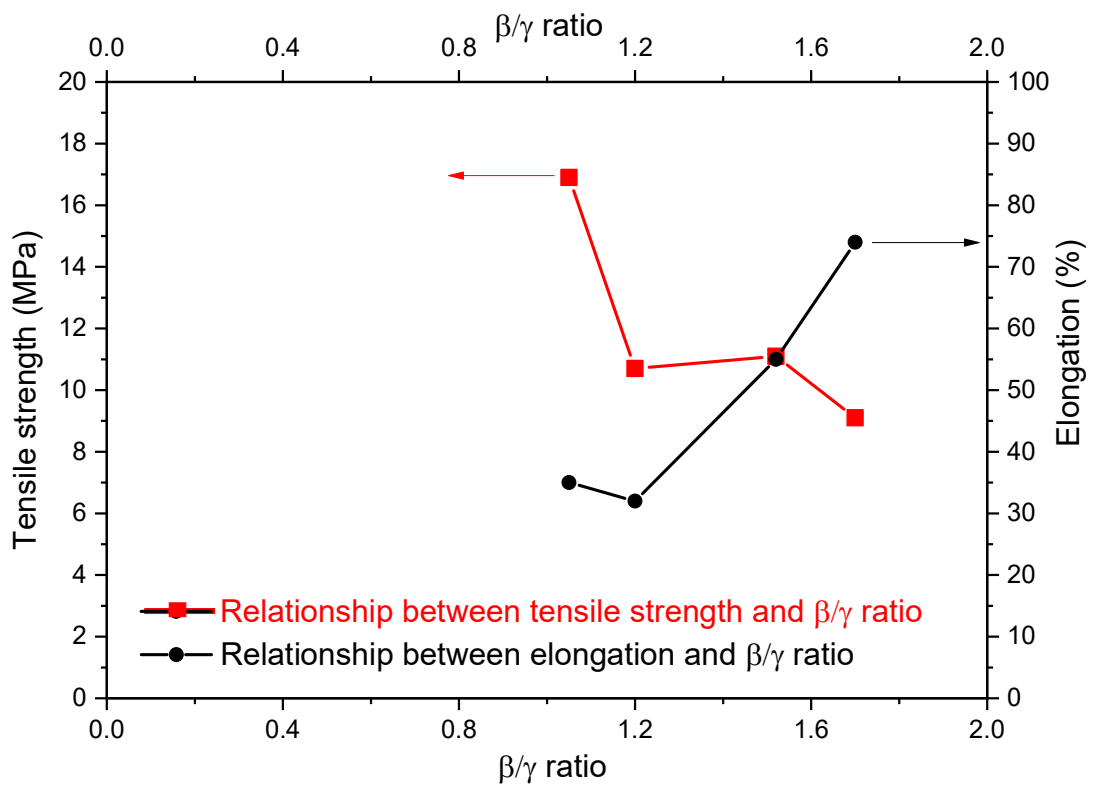
Figure 3.11 Relationship between mechanical properties and the β/γ ratio.

It can be seen that an increase in the β/γ ratio decreases the tensile strength and increases the elongation of the alloy. Moreover, as discussed in Section 3.3.2, Cu atoms become nucleation sites in liquid metal during cooling. Following nucleation at different catalytic sites, the η-(Cu,In,Sn) phase may grow much earlier than the γ-(In,Sn) and β-(In,Sn) phases [26], and would suppress solidification of the β and γ phases of the ISC alloys. Therefore, the sizes of the β and γ phases in the ISC alloys are smaller than those in the eutectic In52Sn48 alloy. ISC488 in particular, as shown by the EPMA mapping in **Figure 3.6**, exhibits the highest tensile strength among the alloys studied. Furthermore, owing to the partial phase transformation of the $Cu_6(In,Sn)_5$ into the $Cu(In,Sn)_2$ phase, only a small amount of $Cu_6(In,Sn)_5$ remains because of the large phase boundaries in ISC488. During the deformation of ISC488, the small phase sizes and the large phase boundaries between the four phases enhance the tensile strength significantly, which is a type of classical dislocation hardening [27,28]. In contrast, the $Cu_6(In,Sn)_5$ and $Cu(In,Sn)_2$ phases do not have any significant effect on the strength of the ISC481 alloy, owing to their low concentration (7%) in the total area. However, these phases slightly increase the strength of ISC482, where their concentration is 13%. Additionally, as shown in the chart in **Figure 3.8**, the area fraction of $Cu_6(In,Sn)_5 + Cu(In,Sn)_2$ (~38%) phases is 7% higher than that of the soft In_3Sn (~31%) phase in ISC488; therefore, its elongation is nearly the same as the In52Sn48 alloy.

3.3.4 Fracture mode

Figure 3.12 presents the fracture modes and surfaces of the alloys after the tensile test. The In52Sn48 (**Figure 3.12a,b**) and ISC488 (**Figure 3.12g,h**) alloys exhibit a similar brittle fracture mode. A typical brittle mode with planar stress fractures on inclined planes can be observed in **Figures 3.12a,g**. Some cleavages with sharp edges, which can be ascribed to transgranular fracture internal phases, can be observed on the surface, as shown in **Figure 3.12b,h**. This fracture phenomenon can also be observed in ISC481 and ISC482 but at a higher density, where both alloys exhibit a ductile mode fracture (**Figure 3.12d,f**).
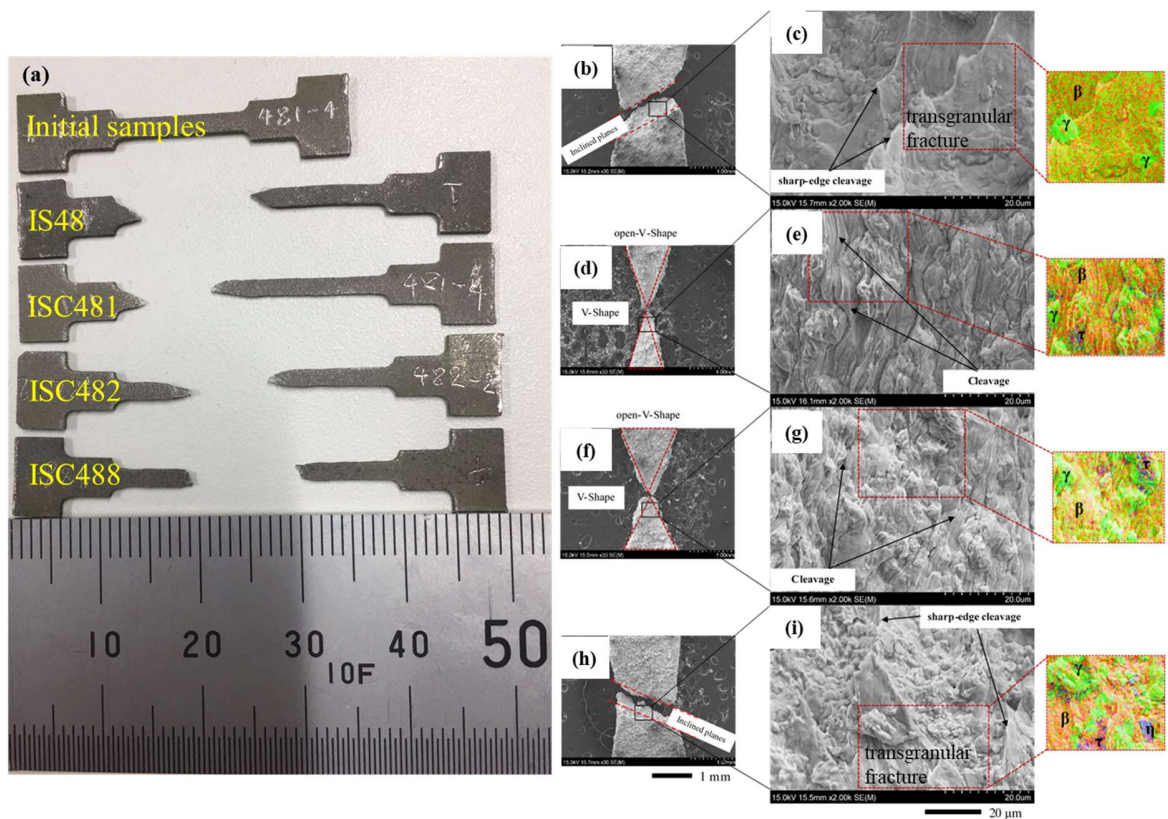
Figure 3.12 (a) Typical fractured tensile samples before and after testing; fracture modes of the (b,c) IS48 (d,e) ISC481, (f,g) ISC482, and (h,i) ISC488 alloys

Next, the V-shaped necking areas were observed on both the broken side of the ISC481 and ISC482 tensile sample, where ISC481 exhibits a narrower opened-V-shape than the ISC482 alloy, as shown in **Figure 3.12c,e**; this is consistent with the mechanical results in **Figure 3.10,** where ISC481 displays greater elongation (74%) than ISC482 (55%). Finally, EDX mapping analysis revealed that the τ-IMC phase appears on the fracture surface of the ISC481 and ISC482 samples, and both η and τ phases appear on the fracture surface of ISC488. These results are consistent with the increase in the IMC fraction, as shown in **Figure 3.8**. The increased number of IMC phases enhances the tensile strength of ISC488, as discussed in Section 3.3.3.

3.4 Conclusions

In this chapter, the effects of the addition of 1.0, 2.0, and 8.0 wt.% Cu on the properties of the eutectic In52Sn48 alloy were obvious. Conclusions are given below and the results are summarised in **Table 3.3**.

- Owing to the ternary eutectic reaction, the initial fusion temperatures of the ISC alloys are all approximately 115ºC, which is close to that of the eutectic In52Sn48 alloy.

- The ISC481 alloy with the highest dominant β-In$_3$Sn phase fraction and comparatively smaller IMC fraction displays the greatest elongation and lowest tensile strength, while the ISC488 alloy with the largest total amount of the η-Cu$_6$(In,Sn)$_5$ + τ- Cu(In,Sn)$_2$ IMC phases exhibits enhancement of mechanical properties with a tensile strength of approximately 17.0 MPa.

- All the ISC alloys fracture in transgranular mode, as is commonly observed in ductile materials. These results confirm that the addition of Cu has a significant effect on the microstructure, tensile strength, and elongation of the eutectic In52Sn48 alloy.

Table 3.3 Summarized results of chapter 3.

Alloy	Onset melting temperature (˚C)	Microstructure (Eutectic spacing of γ phase)	Elongation (%)	Tensile strength (MPa)
IS48	114.4	9.1 μm	34	11.0
ISC481	*Stable* (114.6)	*Refined* (7.1 μm)	*Better* (74)	*Reduce* (9.0)
ISC482	*Stable* (114.7)	*Refined* (6.8 μm)	*Better* (55)	Slightly increase (11.5)
ISC488	*Stable* (114.8)	*Refined* (5.6 μm)	*Better* (37)	*Better* (17.0)

Reference

1. Susan, D.F.; Rejent, J.A.; Grant, R.P.; Vianco, P.T. The Solidification Behavior and Microstructure of In-Sn-Cu Solder Alloys with Low Cu. *4th Int. Brazing Solder. Conf.* **2009**, 1–6.

2. Uemura, T.; Sakai, T.; Sakuyama, S. Improvement of mechanical properties of In-48mass%Sn solder by Ag and Cu addition. *Proc. 2016 IEEE 18th Electron. Packag. Technol. Conf. EPTC 2016* **2016**, 181–184, doi:10.1109/EPTC.2016.7861467.

3. LIU, X.J.; LIU, H.S.; OHNUMA, I.; KAINUMA, R.; ISHIDA, K.; ITABASHI, S.; KAMEDA, K.; YAMAGUCHI, and K. Experimental determination and thermodynamic calculation of the phase equilibria in the Cu-In-Sn system. *J. Electron. Mater.* **2001**, *30*, 1093–1103, doi:10.3139/146.111135.

4. Lin, S.K.; Yang, C.F.; Wu, S.H.; Chen, S.W. Liquidus projection and solidification of the Sn-In-Cu ternary alloys. *J. Electron. Mater.* **2008**, *37*, 498–506, doi:10.1007/s11664-008-0380-0.

5. Riania, P.; Gabriele Cacciamania, Nadia Parodia, Gabriella Borzonea, Rinaldo Marazzaa, Francesca Nannib, G.G. Phase equilibria in the In–Sn-rich part of the Cu–In–Sn ternary system. *J. Alloys Compd.* **2009**, *487*, 90–97.

6. Meigh, H.J. *Ternary Alloy Systems*; 2019; Vol. 11; ISBN 9783540257776.

7. Çadirli, E.; Kaya, H.; Gündüz, M. Effect of growth rates and temperature gradients on the lamellar spacing and the undercooling in the directionally solidified Pb-Cd eutectic alloy. *Mater. Res. Bull.* **2003**, *38*, 1457–1476, doi:10.1016/S0025-5408(03)00169-7.

8. Shepelevich, V.G.; Wang, J. Structure and microhardness of rapidly solidified In-Sn foils. *Inorg. Mater.* **2012**, *48*, 577–581, doi:10.1134/S0020168512050184.

9. Le Han, D.; Shen, Y.A.; Jin, S.; Nishikawa, H. Microstructure and mechanical properties of the In–48Sn–xAg low-temperature alloy. *J. Mater. Sci.* **2020**, *55*, 10824–10832, doi:10.1007/s10853-020-04691-7.

10. Goldstein, J.L.F.; Morris, J.W. The Effect of Substrate on the Microstructure and Mechanical Behavior of Eutectic Indium-Tin. *MRS Proc.* **1994**, *323*, doi:10.1557/proc-323-159.

11. Zhou, S.; Shen, Y.A.; Uresti, T.; Shunmugasamy, V.C.; Mansoor, B.; Nishikawa, H. Improved mechanical properties induced by In and In & Zn double additions to eutectic Sn58Bi alloy. *J. Mater. Sci. Mater. Electron.* **2019**, *0*, 0, doi:10.1007/s10854-019-01056-y.

12. Susan, D.F.; Rejent, J.A.; Hlava, P.F.; Vianco, P.T. Very long-term aging of 52In-48Sn (at.%) solder joints on Cu-plated stainless steel substrates. *J. Mater. Sci.* 2009, *44*, 545–555.

13. Wang, J.; Mao, D.; Shi, L.; Zhang, W.; Zhang, X. Effect of Zinc Addition on the Microstructure, Thermal and Mechanical Properties of Indium-Tin-xZinc Alloys. *J. Electron. Mater.* **2019**, *48*, 817–826, doi:10.1007/s11664-018-6768-6.

14. Song, R.W.; Fleshman, C.J.; Chen, H.; Tsai, S.Y.; Duh, J.G. Suppressing interfacial voids in Cu/In/Cu microbump with Sn and Cu addition. *Mater. Lett.* **2020**, *259*, 126855, doi:10.1016/j.matlet.2019.126855.

15. Lin, S.K.; Chung, T.Y.; Chen, S.W.; Chang, C.H. 250 °C isothermal section of ternary Sn-In-Cu phase equilibria. *J. Mater. Res.* **2009**, *24*, 2628–2637, doi:10.1557/jmr.2009.0317.

16. Ma, H.; C.Suhling, J. A review of mechanical properties of lead-free solders for electronic packaging. *J. Mater. Sci.* **2009**, *224*, 1141–1158, doi:10.1007/s10853-008-3125-9.

17. Kim, J.W.; Jung, S.B. Characterization of the shear test method with low melting point In-48Sn solder joints. *Mater. Sci. Eng. A* 2005, *397*, 145–152.

18. Yang, L.; Yang, Y.; Zhang, Y.; Xu, F.; Qiao, J.; Lu, W.; Yu, B. Microstructure evolution and

mechanical properties of the In–Sn–20Cu composite particles TLP bonding solder joints. *Appl. Phys. A Mater. Sci. Process.* **2020**, *126*, 1–8, doi:10.1007/s00339-020-03523-4.

19. Tanaka, H.; Qun, L.F.; Munekata, O.; Taguchi, T.; Narita, T. Elastic Properties of Sn-Based Pb-Free Solder Alloys Determined by Ultrasonic Pulse Echo Method. *Mater. Trans.* **2005**, *46*, 1271–1273, doi:10.2320/matertrans.46.1271.

20. Cheong, J.; Goyal, A.; Tadigadapa, S.; Rahn, C. Reliable bonding using indium-based solders. *Reliab. Testing, Charact. MEMS/MOEMS III* **2004**, *5343*, 114, doi:10.1117/12.524823.

21. Shu, Y.; Gheybi Hashemabad, S.; Ando, T.; Gu, Z. Ultrasonic powder consolidation of Sn/In nanosolder particles and their application to low temperature Cu-Cu joining. *Mater. Des.* **2016**, *111*, 631–639, doi:10.1016/j.matdes.2016.09.013.

22. Liu, Y.; Tu, K.N. Low melting point solders based on Sn, Bi, and In elements. *Mater. Today Adv.* **2020**, *8*, doi:10.1016/j.mtadv.2020.100115.

23. Zhou, S.; Mokhtari, O.; Rafique, M.G.; Shunmugasamy, V.C.; Mansoor, B.; Nishikawa, H. Improvement in the mechanical properties of eutectic Sn58Bi alloy by 0.5 and 1 wt% Zn addition before and after thermal aging. *J. Alloys Compd.* **2018**, *765*, 1243–1252, doi:10.1016/j.jallcom.2018.06.121.

24. Sayyadi, R.; Naffakh-m, H. The Role of Intermetallic Compounds in Controlling the Microstructural , Physical and Mechanical Properties of Cu- [Sn- Ag-Cu-Bi] -Cu Solder Joints. **2019**, *3*, 1–20, doi:10.1038/s41598-019-44758-3.

25. Ye, D.; Du, C.; Wu, M.; Lai, Z. Microstructure and mechanical properties of Sn–xBi solder alloy. *J. Mater. Sci. Mater. Electron.* **2015**, *26*, 3629–3637, doi:10.1007/s10854-015-2880-z.

26. Perepezko, J.H.; Uttormark, M.J. Undercooling and Nucleation during Solidification. *ISIJ Int.* **1995**, *35*, 580–588, doi:10.2355/isijinternational.35.580.

27. WILLIAM D. CALLISTER, J.; DAVID G. RETHWISCH *Fundamentals Materials science and Engineering : An Integrated Approach*; 5th ed.; John Wiley & Sons, Inc, 2015; ISBN 978-1-119-17548-3.

28. Lu, K.; Lu, L.; Suresh, S. Strengthening materials by boundaries at the nanoscale. *Science (80-.).* **2009**, *349*, 349–353, doi:10.1126/science.1159610.

Chapter 4

Shear strength, microstructure, and the interfacial reaction of In-Sn-xCu/Cu joints

4.1 Introduction

Based on the results in the previous two chapters, we can see that the addition of Cu has a more significant effect on the mechanical properties of the In52Sn48 alloy than the addition of Ag. The elongation of the In52Sn48 bulk alloy is enhanced by a factor of approximately 2.0, and the tensile strength by a factor of approximately 1.5 with the addition of 2.0 and 8.0 wt.% Cu, respectively. Moreover, Cu outperforms Ag in being low cost [1]. Thus, the two developed alloys ISC482 and ISC488 with the best results in terms of mechanical properties, were selected to fabricate joints with a Cu substrate. The results of previous work imply that the interfacial reactions between the In-Sn alloy and the Cu substrate are complicated, and the diffusion of Cu from the substrate into the alloy matrix could affect the composition and thickness of the interface layer [2–9]. The relationships between the microstructure evolutions of alloy matrix, interfacial reactions, and the mechanical changes in the In-Sn/Cu joints with the addition of trace elements such as Cu, are still not completely understood. Therefore, in this chapter, the effects of the addition of Cu on wettability, microstructure evolution, interfacial reactions, and shear strength of the In-Sn-xCu/Cu joints (x = 2.0 and 8.0 wt.%) is investigated.

4.2 Experimental procedure

4.2.1 Materials

The fabrication and characteristics of the new ISC482 and ISC488 alloys are given in the previous chapter, and the chemical composition of the alloys is shown in **Table 4.1**. The eutectic In-48Sn (IS48), In-Sn-2.0Cu (ISC482), and In-Sn-8.0Cu (ISC488) alloy bars were rolled to 100 ± 10 μm thickness foils using a rolling machine (DBR50, Daito Seisakusho, Japan) and punched into 3 and 6 mm diameter alloy foils. Oxygen-free copper discs with diameters of 5 and 10 mm and thickness of 3 and 5 mm were used as upper and lower substrates, respectively. Cu plate (15×15×1 mm) was used as the substrate for the wettability test. Before making the joints, the copper discs and Cu plates were polished with #2000 SiC grit paper and a 1.0-μm diamond paste (DP-spray P, Struer, USA). Subsequently, the alloy foils and copper discs were cleaned with HCl (2 vol%) and ethanol.

Table 4.1 Chemical compositions of the eutectic IS48, ISC482, and ISC488 alloys.

Element	In52Sn48-2.0Cu (IAC482), *wt. %*	In52Sn48-8.0Cu (ISC488), *wt. %*	In52Sn48 (IS48), *wt. %*
Sn	47.720	45.000	48.200
In	Balance	Balance	Balance
Cu	1.530	7.370	0.003
Ni	0.001	0.001	0.001
Bi	-	-	0.02
Pb	0.001	0.001	0.001

To make wettability test samples, four alloy discs (3-mm diameter, 100-μm thickness) of the IS48, ISC482, and ISC488 alloys were coated with a drop of flux (IEC60068-69, SMIC, Japan) then placed on the Cu plate and heated in a furnace (SK-5000 SMT-Scope, Sanyoseiko, Japan) with a heating profile as shown in **Figure 4.1a.** To make the alloy joints, six alloy foils (6-mm diameter, 100-μm thickness) of the IS48, ISC482, and ISC488 alloys were coated with a drop of flux (IEC60068-69), then the alloy foils were placed between the 5-mm upper copper disc and 10-mm bottom disc to make the joint samples. The samples were then placed in an SK-5000 SMT-Scope furnace with a heating profile as shown in **Figure 4.1b.** The joints were preheated at 110°C for 60 s and reflowed at 160°C for 90 s in N_2 atmosphere; the concentration of oxygen in the furnace was maintained below 1000 ppm.

4.2.2 Characterisation methods

A colour 3D laser scanning microscope (VK-9700, Keyence, Japan) was used to measure the wetting angles of the alloys on the Cu substrate. Four wettability test samples were prepared and six positions were measured for each wettability sample; a typical demonstration of this method is shown in **Figure 4.2**. The cross-section of the wettability test samples was observed using SEM (SU-70, Hitachi, Japan). Then, ImageJ software was used with the SEM images to measure the wetting angles of the IS48, ISC482, and ISC488

alloys on the Cu substrate. The shear strength of the joint was determined at room temperature (20°C) using a shear test machine (STR-1000, Rhesca, Japan) operated at a crosshead rate of 1 mm/min; a schematic of the shear test is shown in **Figure 4.3**. The shear strength was calculated by dividing the maximum shear force at the failure site by the area of the alloy joint. The average shear strength was calculated on six Cu/alloy/Cu joints for the IS48, ISC482, and ISC488 alloys.
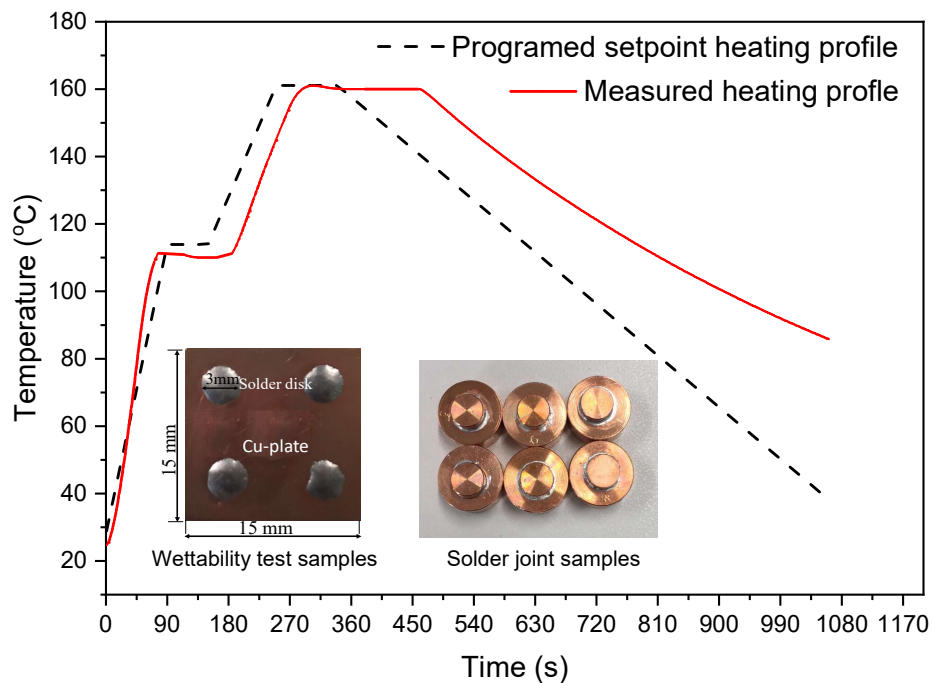
Figure 4.1 Heating profile of the reflow process for wettability test samples, and alloy joint samples.
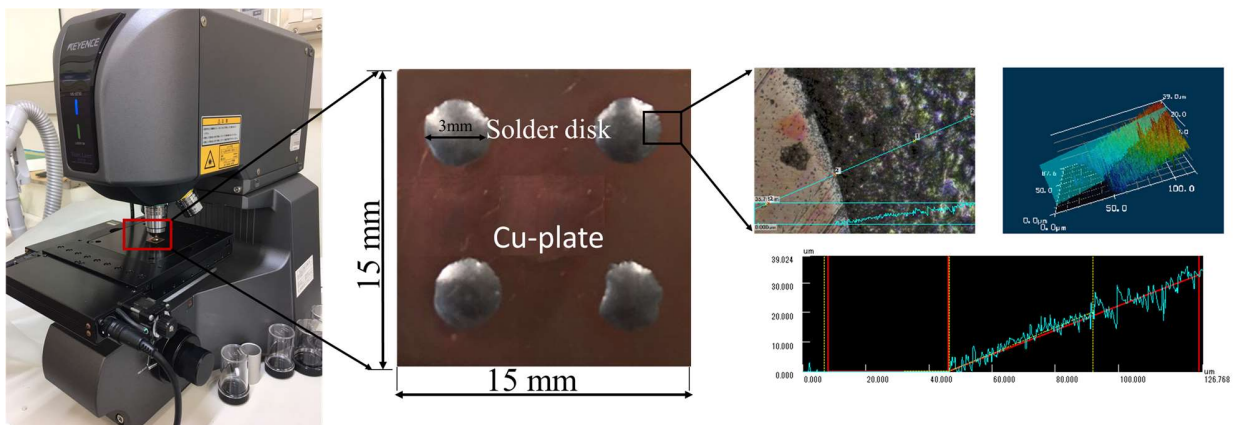
Figure 4.2 Typical demonstration of using of color 3D laser scanning microscope to measure the contact angle of alloy/Cu joints.
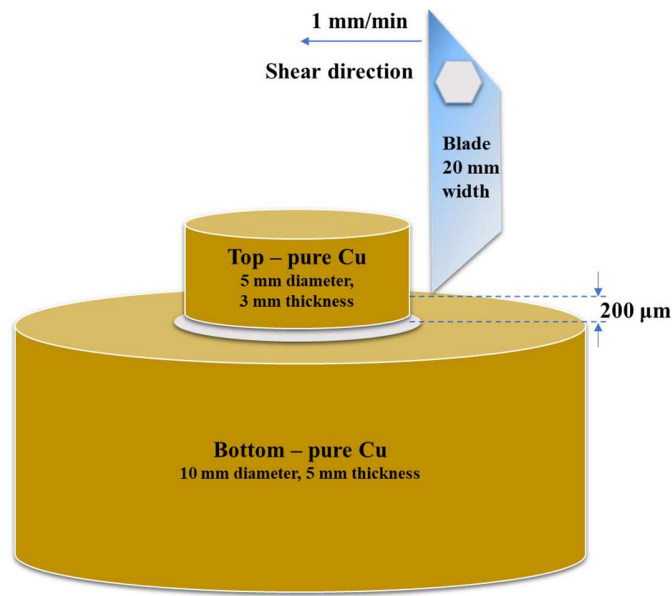
Figure 4.3 Schematic illustration of the shear test.

To identify the IMC at the interfacial layer between the alloy and the Cu substrate, the top Cu disc of the shear samples after the shear test of the Cu/IS48/Cu and the Cu/ISC488/Cu joints was used as XRD samples. The fracture surfaces of the XRD samples were polished using a 1.0-µm alumina suspension (Buehler, USA) until the IMC layer was detected near the substrate side. Subsequently, the samples were taken for X-ray diffraction (XRD; Ultima IV, Rigaku, Japan) examination in the 2θ range of 25-80° at a scan rate of 1°/min. The microstructure, interfacial layer of the alloy joints, and top view of the shear-fractured samples were examined by SEM equipped with EDS. The elemental distribution of the alloy matrix and the interfacial layer was analysed using a field-emission electron probe microanalyser (FE-EPMA; JXA-8530F JEOL, Japan). The shear-fractured samples were sectioned, mounted, ground with SiC grit papers (#150, 400, 800, 1200, and 2000), and finely polished using a 1.0-µm alumina suspension. SEM and EPMA were used to study crack propagation in the alloy joints after the shear test. The thickness of the IMC layers was measured using ImageJ software. Four EPMA maps of Cu for each alloy were used for the IMC thickness measurements. IMC thickness was measured at twenty different locations on each Cu map, from which the average value of the IMC layer was calculated.

4.3 Results and discussion

4.3.1 Wettability

The wetting phenomenon together with the dissolution of the substrate in the molten alloy leads to the formation of IMC layers by complex surface reactions. As a result, significant changes take place in the microstructure and composition of the interface and the alloy itself, ultimately affecting both the wetting behaviour and the mechanical properties of the alloy joint [10]. The contact angle (θ) is typically used as a measure of the wettability of an alloy on a substrate. In a state of equilibrium, the relationship between the solid-liquid (γ_{sl}), solid-vapour (γ_{sv}), and liquid-vapour (γ_{lv}) interfacial tensions is defined by Young's Equation [11]:

$$\mathrm{Cos\theta} = \frac{\gamma_{sv} - \gamma_{sl}}{\gamma_{lv}} \tag{1}$$

Figure 4.4 shows a typical cross-section of alloy/Cu joints, in which the contact angles of the IS48, ISC482, and ISC488 alloys on the Cu substrate are 16°, 25°, and 37°, respectively. Combined with the results measured by the 3D laser scanning method, the contact angle can be summarized as shown in **Figure 4.5**; the error bar displays the maximum and minimum values, and the dots indicate the original test results at 24 positions. It should be noted that the contact angle increases with an increase in Cu content. Researchers [12,13] have studied the viscosity of the element Cu in liquid Cu-In-Sn alloys and the surface tension of the same liquid alloy. Ali et al. reported that the viscosity values of liquid Cu-In-Sn alloys at 1073 K increase from approximately 0.001 Pa•s to 0.003 Pa•s when the Cu concentration increases from 20 at.% to 80 at.%, respectively. The surface tension values of liquid Cu-In-Sn alloys at 1073 K increase from approximately 0.49 N/m to 0.53 N/m when the Cu content increases from 20 at.% to 30 at.%, respectively. This result is due to the higher viscosity of liquid Cu (4.5560 mPa•s) than In (0.6995 mPa•s) and Sn (1.0878 mPa•s) [12]. Therefore, the addition of Cu leads to an increase in the surface tension of the ISC molten alloy (γ_{lv}), thereby reducing the value of cosθ (in Equation (1)); this explains the increase in the θ values of the ISC482 and ISC488 alloys relative to the IS48 alloy. However, the wettability of the ISC482 and ISC488 alloys with the Cu substrate

is acceptable because the contact angles are lower than those of other low melting temperature alloys, as listed in **Table 4.2**.
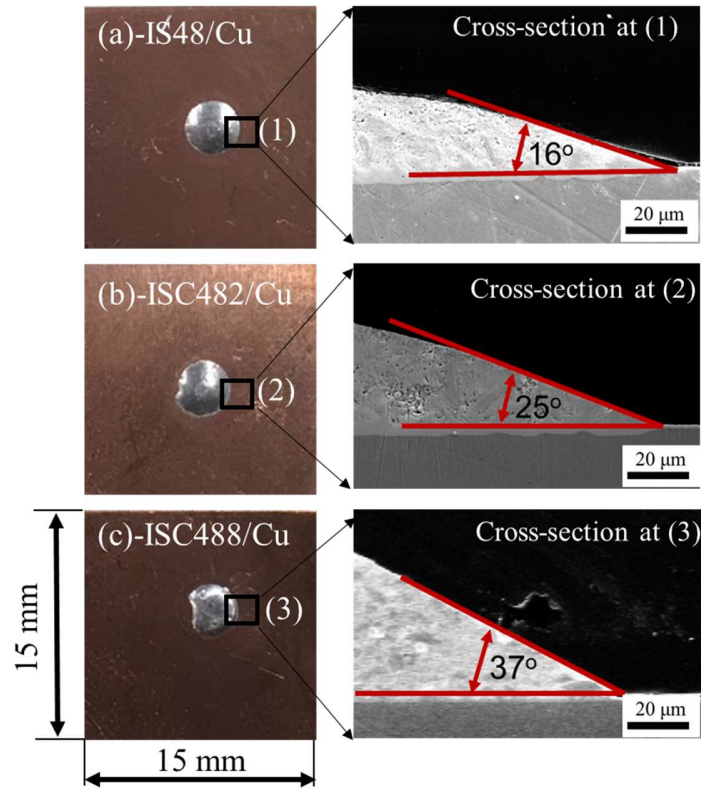
Figure 4.4 Cross-sectional of (a) IS48/Cu, (b) ISC482/Cu, and (c) ISC488/Cu joints.
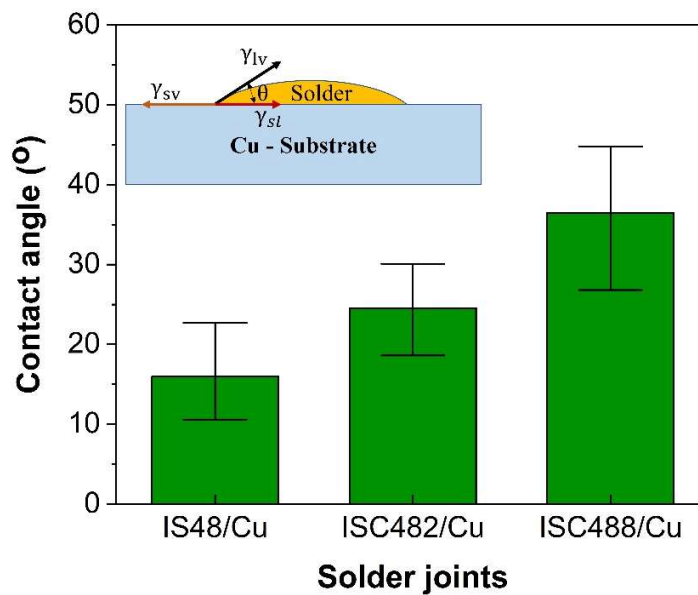
Figure 4.5 Contact angles of IS48, ISC482, and ISC488 alloys on Cu substrate.

Table 4.2 Wetting angle of IS48 and ISC alloys in comparison with other alloys.

Alloy	Wetting angle, θ°	Remark
IS48	16	This study
ISC482	25	This study
ISC488	37	This study
In–31.6Bi–19.6Sn	39	[14]
69.5Sn–30Bi–0.5Cu	45	[15]

4.3.2 Microstructure evolution and interfacial reaction

During the reflow process, the IMC layer is formed at the interface because some reactions occur between the alloys and the Cu substrate. This IMC layer plays a crucial role in the manufacture and reliability of the alloy joints [16]. **Figure 4.6** shows the low-magnification view of the cross-sectional SEM images of the Cu/IS48/Cu, Cu/ISC482/Cu, and Cu/ISC488/Cu alloy joints. The continuous layers of the IMCs indicate good bonding between the ISC alloys and the Cu discs; this can be attributed to the acceptable wettability of all the alloys. **Figure 4.7** shows the high-magnification view of the cross-sectional backscattered electrons (BSE) and EPMA images of the Cu/IS48/Cu, Cu/ISC482/Cu, and Cu/ISC488/Cu alloy joints. It is clear that two main phases, namely, β-(In,Sn) and the γ-(In,Sn), are formed in the alloy matrixes of the In-Sn-xCu/Cu joints.
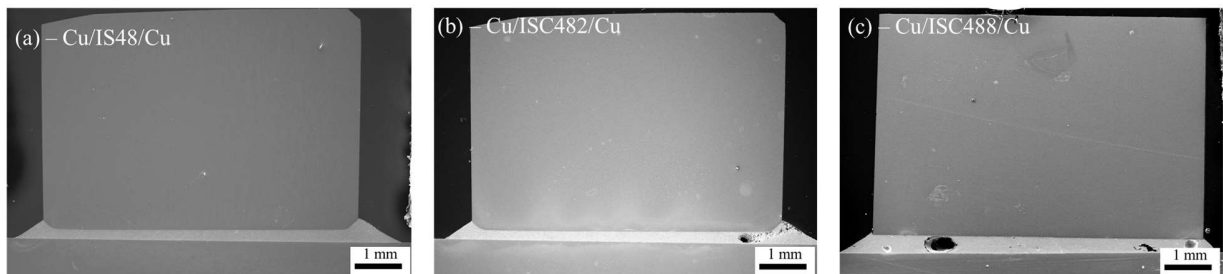
Figure 4.6 Low-magnification view of the cross-sectional SEM images of: (**a**) Cu/IS48/Cu, (**b**) Cu/ISC482/Cu, and (**c**) Cu/ISC488/Cu joints.
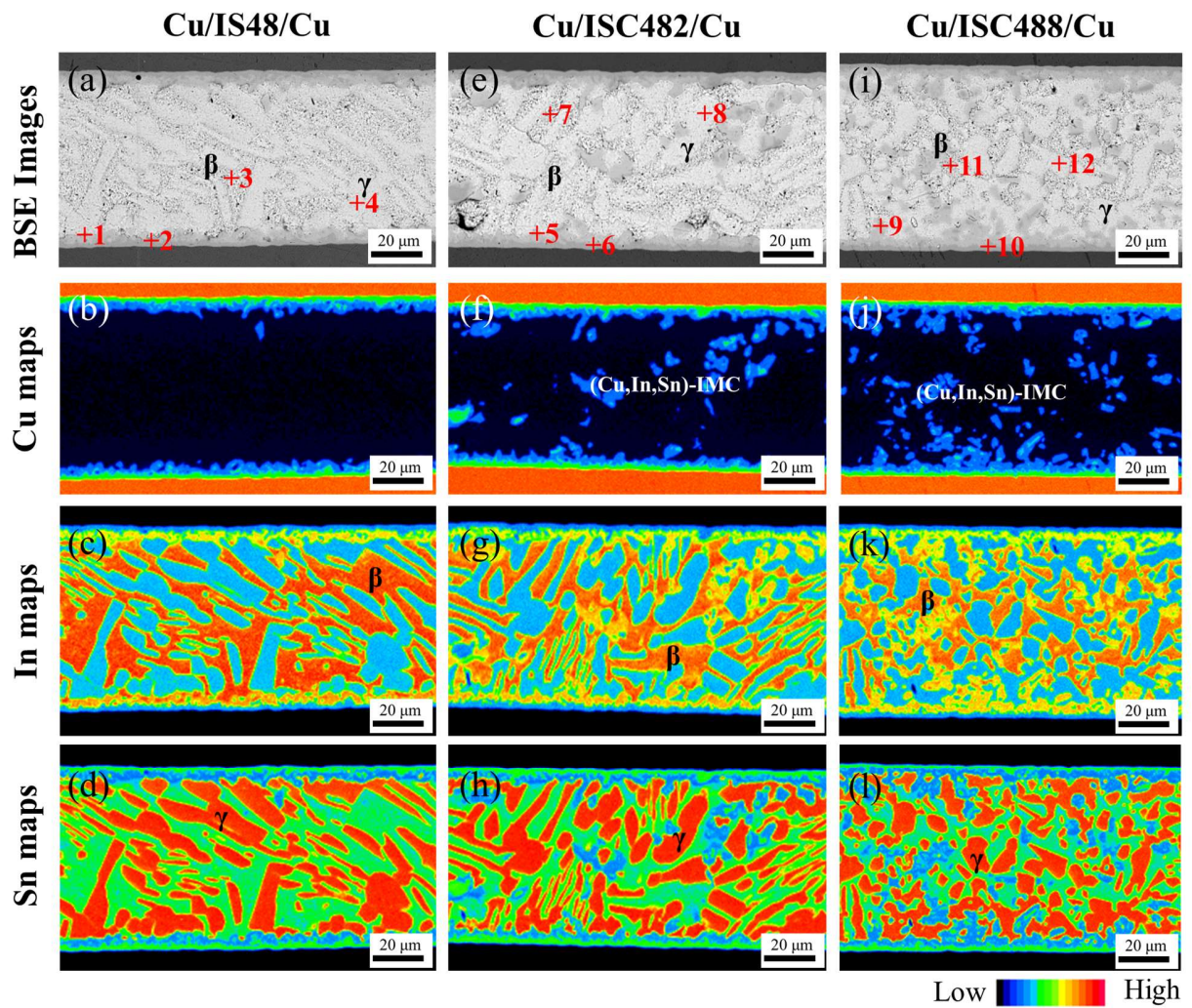
Figure 4.7 The high-magnification view of the cross-sectional BSE and EPMA images of the: (**a-d**) Cu/IS48/Cu joint, (**e-h**) Cu/ISC482/Cu joint, and (**i-l**) Cu/ISC488/Cu joint; and the locations of the EPMA points listed in **Table 4.2**.

The β-(In,Sn) and the γ-(In,Sn) phases are formed through eutectic reactions during cooling from 115°C to 113°C, as discussed in our previous study [17]; these results are consistent with the phase constitutions in the In-Sn phase diagram [18] and other reported results [19]. The (Cu,In,Sn)-IMC formed in the ISC482 and ISC488 alloy matrixes (**Figures 4.7f,j**) lead to finer microstructures compared to those of the IS48 alloy (**Figures 4.7c,g,k**). The microstructural evolution of the IS48, ISC482, and ISC488 alloy matrixes after the reflow is consistent with the behaviours of bulk alloys after casting. However, it is well known that the cooling rate during solidification process will effect on the microstructure of alloy

[7,20,21]. Seah [22] reported that dendrite arm spacing decreases with increasing cooling rate and hence fine-grained microstructures of cast iron then improved mechanical properties of this alloy. The cooling rate used in a solder joint reflow process is approximately 7 °C/min, which is slower than normal cooling rate as-cast condition [23]. As a result, **Figure 4.8** exhibits that the eutectic spacing in all alloy matrixes of solder joints is higher than that of the bulk IS48 and ISC alloys, as mentioned in Section 3.3.2 of Chapter 3. The chemical composition of the β-(In,Sn), γ-(In,Sn) phases and the IMC layers obtained using EPMA point analysis are summarised in **Table 4.3**. The results indicate the formation of two layers of IMCs at the interface between the ISC alloys and the Cu substrate: a Cu-rich $Cu_6(In,Sn)_5$ layer near the Cu substrate and a Cu-deficient $Cu(In,Sn)_2$ layer near the alloy matrix. The total thicknesses of the IMC layers $[Cu_6(In,Sn)_5 + Cu(In,Sn)_2]$ for each interface, as calculated using the ImageJ software and high-magnification EMPA Cu maps, as mentioned in Section 4.2.2, are shown in **Figure 4.9.** The error bars show the maximum and minimum deviations within the measured values of 80 positions in the four EPMA Cu maps for each alloy. The total thickness of the IMC layer of IS48 is the highest, approximately 6.6 μm, followed by ISC488 (6.4 μm), and ISC482 (5.8 μm).
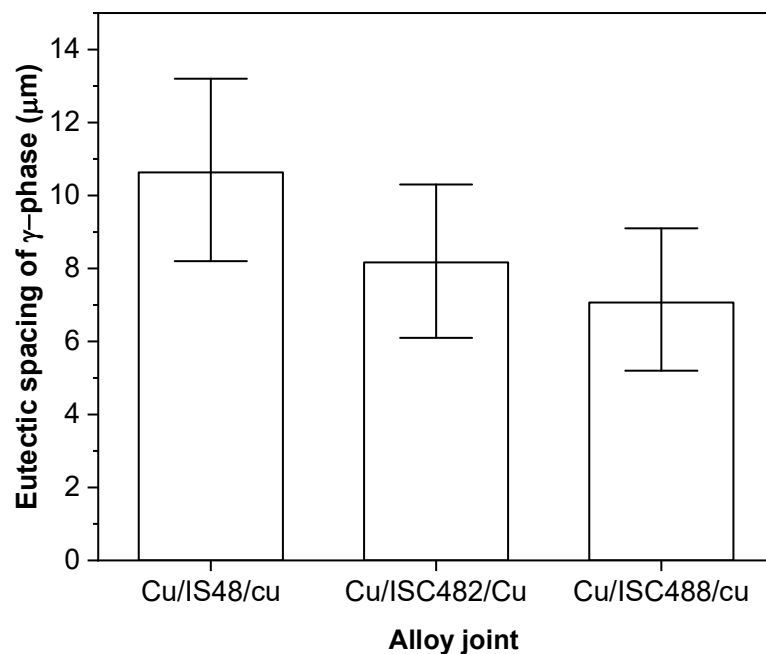
Figure 4.8 Eutectic spacing of alloy joints.

Table 4.3 Elemental composition of the points marked in **Figure 4.7**.

Alloy joint	Point	Cu (at. %)	In (at. %)	Sn (at. %)	Estimated IMC
Cu/IS48/Cu	1	31.36	52.72	15.92	τ-Cu(In,Sn)$_2$
	2	56.51	20.60	22.89	η-Cu$_6$(In,Sn)$_5$
	3	0.05	75.75	24.20	β-In$_3$Sn
	4	0.07	24.53	75.40	γ-InSn$_4$
Cu/ISC482/Cu	5	32.16	53.83	14.01	τ-Cu(In,Sn)$_2$
	6	56.89	20.39	22.72	η-Cu$_6$(In,Sn)$_5$
	7	0.76	75.61	23.63	β-In$_3$Sn
	8	0.83	24.03	75.14	γ-InSn$_4$
Cu/ISC488/Cu	9	30.95	54.93	14.12	τ-Cu(In,Sn)$_2$
	10	58.49	23.74	17.77	η-Cu$_6$(In,Sn)$_5$
	11	0.93	73.98	25.09	β-In$_3$Sn
	12	0.87	24.94	74.19	γ-InSn$_4$
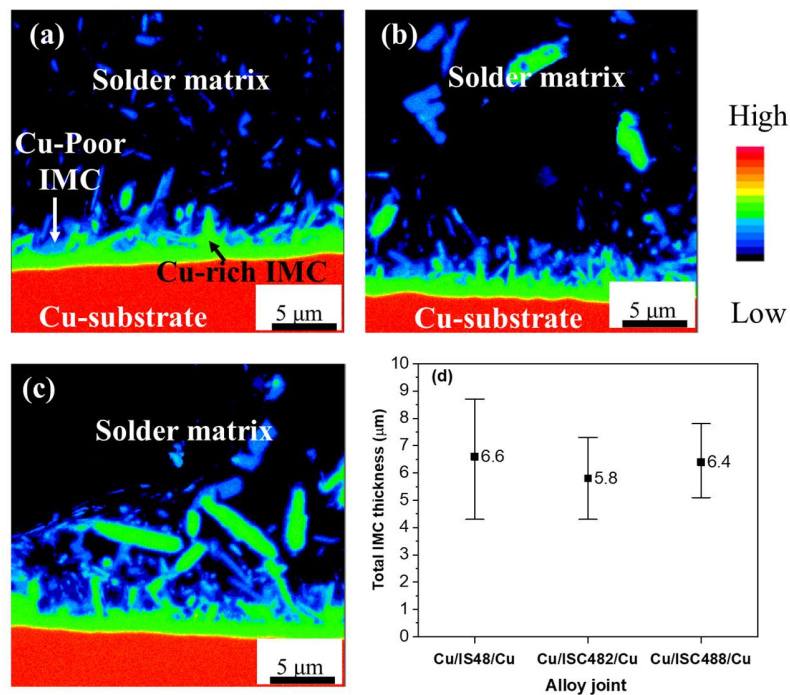
Figure 4.9 (a-c) Typical EMPA Cu maps images, and (d) total thickness of the IMC layer in Cu/IS48/Cu, Cu/ISC482/Cu, and Cu/ISC488/Cu joints.

Figure 4.10 illustrates the mechanism of IMC formation at the interfaces of the alloy joints. At the initial stages of joint formation (stage 1), the Cu atoms from the substrate tend to diffuse and dissolve into the liquid In-Sn alloy; after that they quickly react with In and Sn atoms in the alloy matrix to form a thin $Cu_6(In,Sn)_5$ IMC layer at the interface (stage 2), which is consistent with the η-Cu_6Sn_5 phase formed during the Sn/Cu interfacial reaction [9]. Subsequently, during the cooling process, the β and γ phases are solidified; the $Cu_6(In,Sn)_5$ IMC layer increases the thickness and some $Cu_6(In,Sn)_5$ IMC also formed in the alloy matrixes of Cu/ISC482/Cu and Cu/ISC488/Cu joints owing to the presence of 2 wt.% Cu in the ISC482 and 8 wt.% Cu in the ISC488 alloys (stage 3). When the temperature below 90 °C, the Cu-deficient $Cu(In,Sn)_2$ IMC is formed surrounding a $Cu_6(In,Sn)_5$ IMC (stage 4) as a result of solid-solid transformation from the $Cu_6(In,Sn)_5$ IMC [17,24], as mentioned in Section 3.3.1 in Chapter 3.
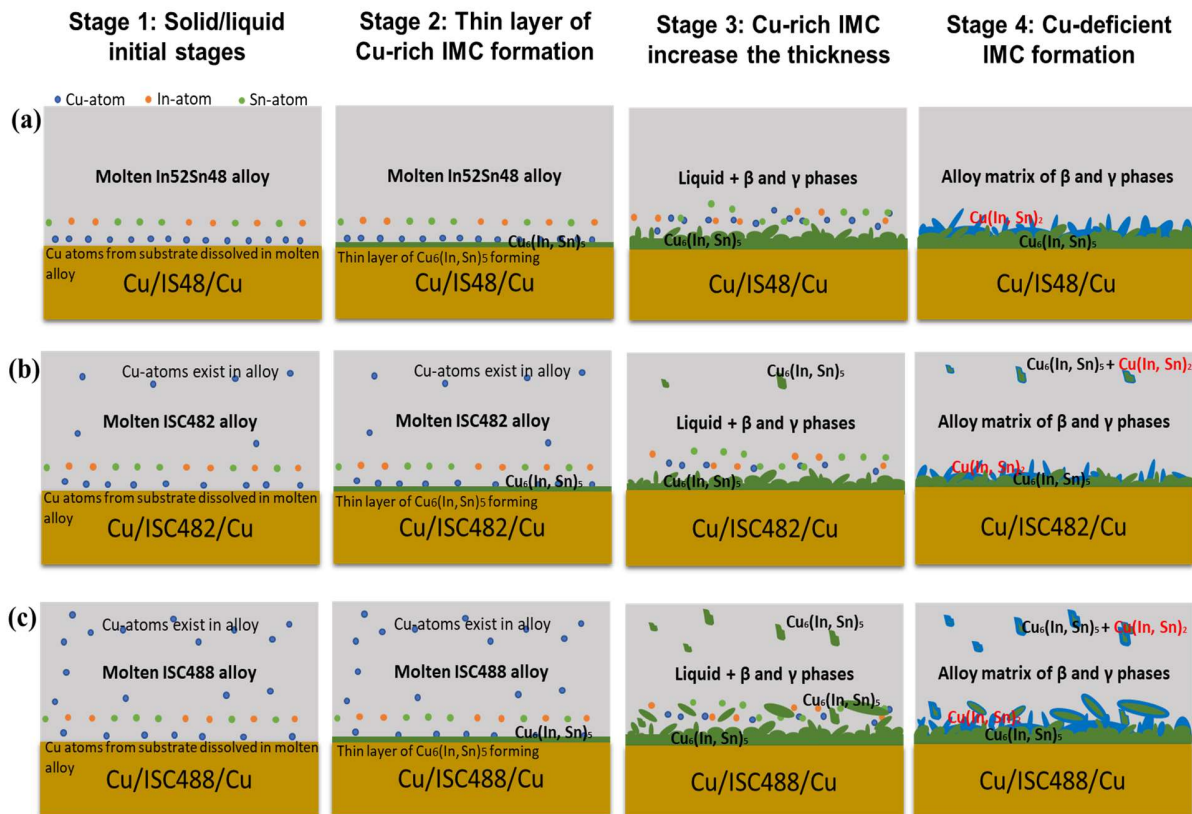
Figure 4.10 Illustration of the mechanism of IMC formation at the interface of (a) Cu/IS48/Cu, (b) Cu/ISC482/Cu, and (c) Cu/ISC488/Cu joints.

The reduction in thickness of the IMC layer at the interface between the ISC482 alloy and the Cu substrate when compared to the IS48 alloy, can be attributed to the presence of 2 wt.% Cu in the ISC alloy (**Figure 4.10b**); this suppresses the diffusion of Cu from the substrate to the molten In-Sn alloy. On the other hand, although the large amount of Cu in the ISC488 alloy (8 wt.%) leads to little diffusion of Cu from the substrate into the liquid alloy, the higher amount of (Cu,In,Sn)-IMC formed in the ISC488 alloy matrix near the interface tends to merge with the $Cu_6(In,Sn)_5$ layer of the ISC488/Cu interfacial layer (**Figure 4.10c**). Consequently, the ISC488/Cu interface exhibits greater total thickness and surface roughness compared to the ISC482/Cu interface (**Figure 4.9b,c**).

Figure 4.11 shows the XRD patterns of the IS48/Cu and ISC488/Cu interfaces; β-In_3Sn and γ-$InSn_4$ phases are observed (PDF card # 00-007-0345 and PDF card # 00-007-0396) because the alloy remains on the polished samples of the IS48/Cu and ISC488/Cu interfaces. The peaks at 2θ angles of $43.45°$ and $50.31°$ originate from the Cu substrate (PDF card # 00-001-1241). The peaks at $29.98°$ and $34.19°$ correspond to the η-Cu_6Sn_5 phase (PDF card # 01-076-2703). It should be noted that $Cu_6(In,Sn)_5$ has a Cu_6Sn_5 crystal structure due to the solid solution effect of In atoms in the Cu_6Sn_5 crystal lattice forming a $Cu_6(In,Sn)_5$ IMC layer at the alloy/Cu interface [25]. Moreover, the peaks at $26.24°$, $45.41°$, $33.43°$, and $68.93°$ correspond to the τ-$CuIn_2$ phase (PDF card # 01-080-3063). It has been reported that Sn and In atoms have similar atomic radii, and so Sn atoms can substitute In atoms through solid state diffusion during cooling after the reflow process [26,27]; hence, the IMC near the alloy matrix should be represented as $Cu(In,Sn)_2$ [27].

4.3.3 Shear strength

Generally, the fine microstructures of the alloy matrixes and the thickness and roughness of the IMC layer, affect the reliability of the alloy/Cu joint [28,29]. **Figure 4.12** shows the shear strengths of the Cu/IS48/Cu, Cu/ISC482/Cu, and Cu/ISC488/Cu joints; the error bar displays the maximum and minimum values, and the dots indicate the original test results.
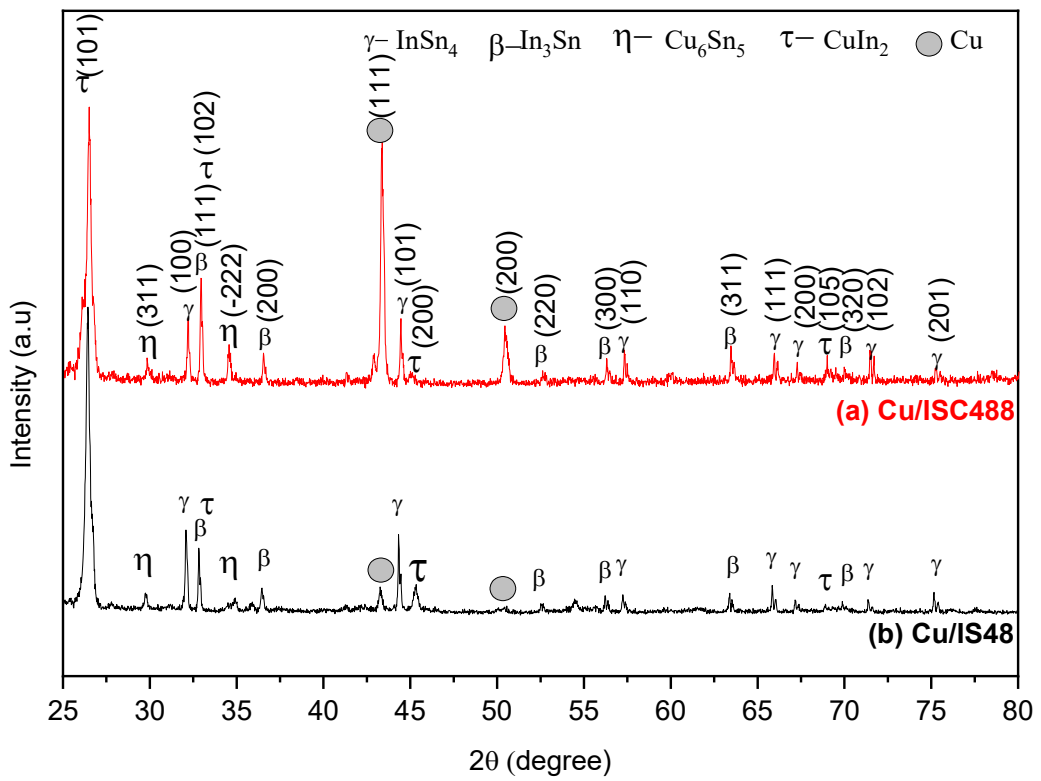
Figure 4.11 XRD patterns of the (**a**) ISC488/Cu and (**b**) IS48/Cu alloys.
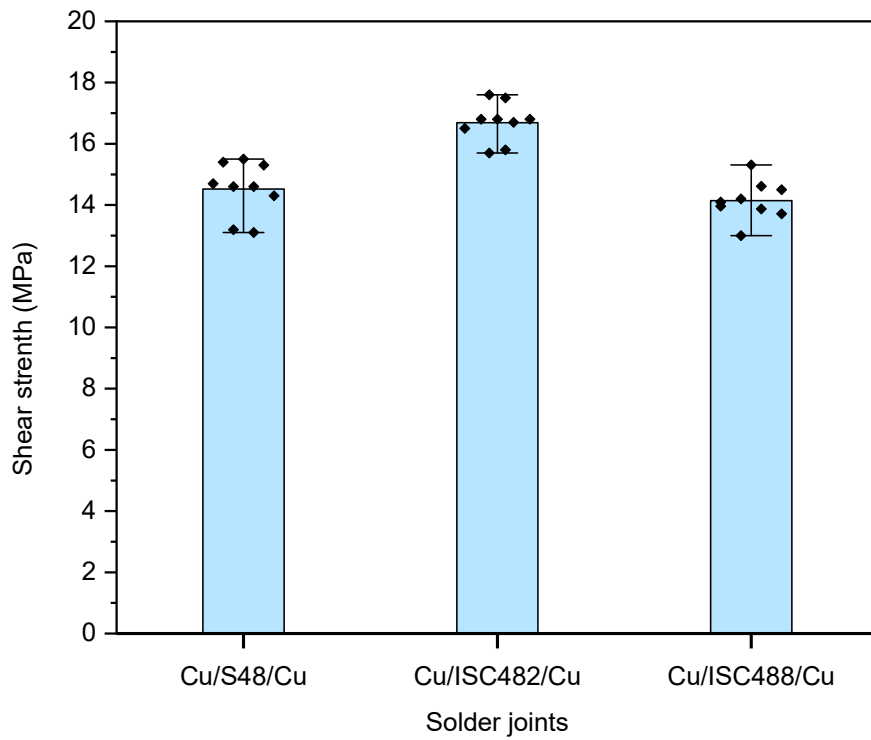
Figure 4.12 Shear strengths of the alloy joints.

The Cu/IS48/Cu joint exhibits an average shear strength of approximately 14.5 MPa, which is nearly equal to that of the Cu/ISC488/Cu joint (14.3 MPa) and is approximately 14% lower than that of the Cu/ISC482/Cu joint (16.5 MPa). **Figure 4.13** shows the top view SEM and EPMA images of the fracture samples of the Cu/IS48/Cu, Cu/ISC482/Cu, and Cu/ISC488/Cu joints at the bottom disc side after shear testing. **Figure 4.13 (b,c)** shows that the void distribution in the shear fracture surfaces of ISC482/Cu and ISC488/Cu increases with an increase in the Cu content, and is higher than that of IS48/Cu.
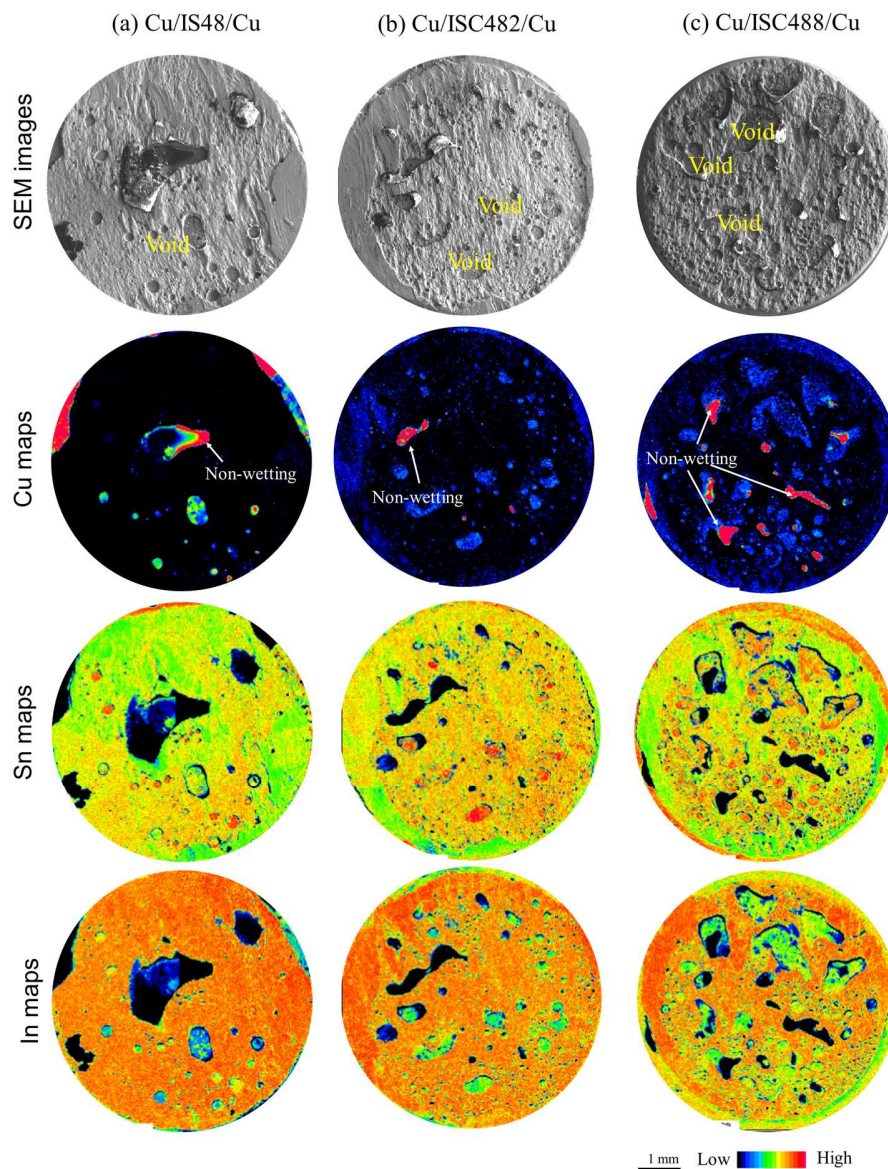
Figure 4.13 Top view SEM and EPMA images of the fractured samples at the bottom disks after the shear test: (**a**) Cu/IS48/Cu, (**b**) Cu/ISC482/Cu, and (**c**) Cu/ISC488/Cu joints.
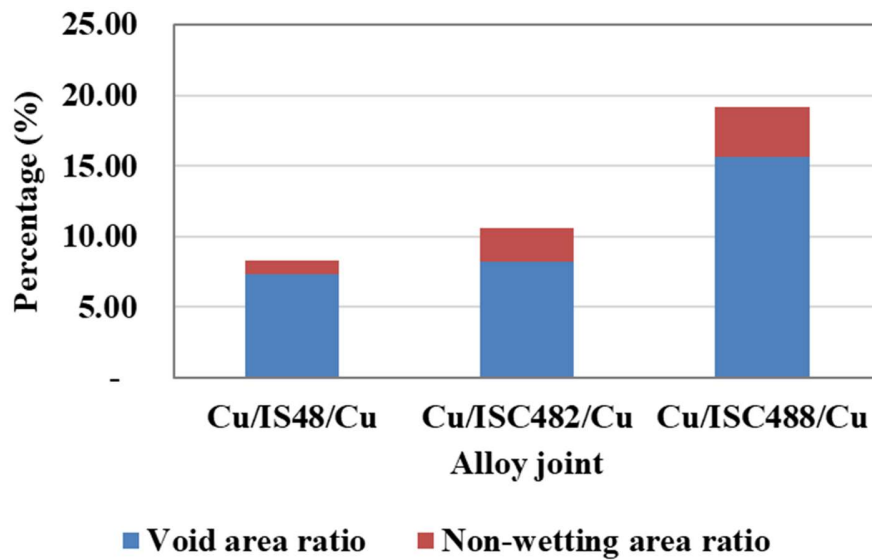
Figure 4.14 Percentage of void and non-wetting area on fracture surface of alloy joints.

The percentage of voids and non-wetting areas on the shear fracture surface samples was measured using ImageJ software. Four EPMA images of the fractured samples for each alloy joint were used for this measurement; the smallest area was calculated as 0.01 mm^2, and the results are summarised in **Figure 4.14**. The results indicate that the percentage of non-wetting (3.5%) and voids (15.7%) are largest on the fracture surfaces of ISC488/Cu because ISC488/Cu exhibits the lowest wettability on the Cu substrate, as discussed previously. The next largest values are for the Cu/ISC482/Cu joint (2.5% and 8.2%, respectively), and Cu/ISC482/Cu joint (0.97% and 7.3%, respectively). The void formation and non-wetting regions may be the reasons for the reduced shear strength of Cu/ISC488/Cu joints.

4.3.4 Fracture behaviour

The void formation, thickness, and morphology of the IMC layer significantly affect the strength of the alloy joint owing to its brittle nature [30,31]. **Figure 4.15** shows that although all the alloy joints exhibit ductile behaviour, with many dimples on the fracture surface, the fracture surface of IS48/Cu has fewer voids and no IMC. A few large fragments of (Cu,In,Sn)-IMC are observed near the voids on the fracture surface of ISC488/Cu (**Figure 4.15i**), which suggests stress concentration of voids; this confirms the low shear strength of the ISC488/Cu joint.
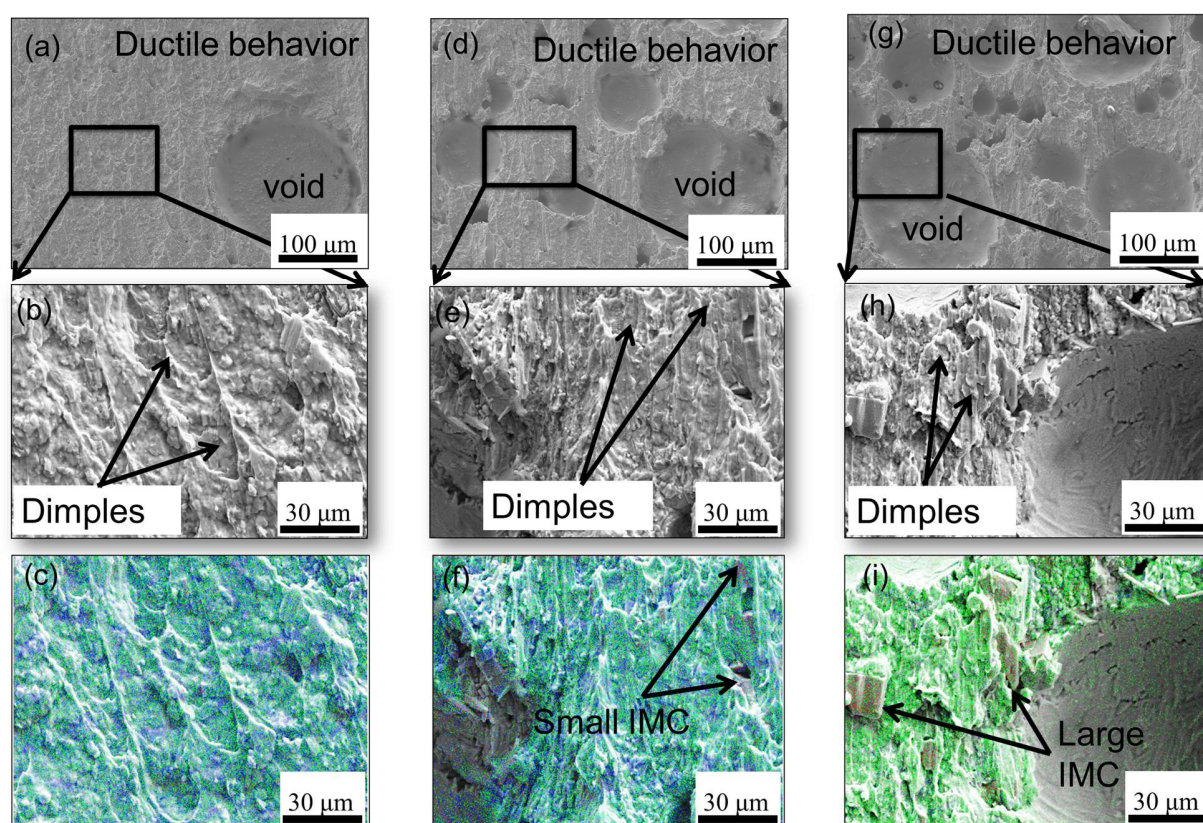
Figure 4.15 SEM images of the fracture surface of shear test samples: **(a-c)** Cu/IS48/Cu, **(d-f)** Cu/ISC482/Cu, and (g-i) Cu/ISC488/Cu joints.

Conversely, a few small fragments of (Cu,In,Sn)-IMC are found on the fracture surface of ISC482/Cu (**Figure 4.15f**), and the number and size of the voids are smaller when compared to those observed on the fracture surface of ISC488/Cu. Hence, the ISC482/Cu joint exhibits greater shear strength compared to the other alloy joints. **Figure 4.16 (a-c)** shows the SEM images of typical cross-sectional fracture samples. Crack propagation occurs in the alloy matrixes of both the ISC alloy joints and along the alloy/IMC interfaces, with the formation of a few non-wetting regions between the alloys and the substrates because of the outgassing phenomenon during the reflow process [32]. **Figure 4.16 (d-f)** shows the EPMA maps of Cu obtained from locations (1), (2), and (3) marked in **Figure 4.16(a-c),** respectively. The ISC482/Cu interface has a smoother IMC surface than the IS48/Cu interface, while the ISC488/Cu interface exhibits the roughest IMC surface among all the alloy/Cu interfaces. These results are consistent with those of **Figure 4.9**; the IS48/Cu interface shows the greatest total thickness of the IMC layer owing to the absence of Cu in

the alloy matrix. The IS482/Cu interface has a smaller total thickness of the IMC layer and a highly smooth surface because of the presence of 2 wt.% Cu in the alloy matrix. **Figure 4.17** shows the schematic of the crack propagation and void distribution in the Cu/IS48/Cu, Cu/ISC482/Cu, and Cu/ISC488/Cu alloy joints. It can be seen that the fine microstructure with a small amount of (Cu,In,Sn)-IMC in the ISC482 alloy matrix (**Figure 4.7e-h**) and the thin interfacial IMC layer enhance the reliability of the Cu/ISC482/Cu joint. Large β and γ grains and the absence of a (Cu,In,Sn)-IMC layer in the IS48 alloy matrix (**Figure 4.7a-d**) [17] reduce the shear strength of the Cu/IS48/Cu joint compared to the Cu/ISC482/Cu joint. The Cu/ISC488/Cu joint has finer grains (**Figure 4.7i-l**); however, it also has the highest number of voids (**Figure 4.14)** and the roughest interfacial IMC layer of all the alloy joints (**Figure 4.9c**); these may act as additional stress concentration points [33] causing a reduction in the shear strength of the Cu/ISC488/Cu joint, as shown in **Figure 4.12**.
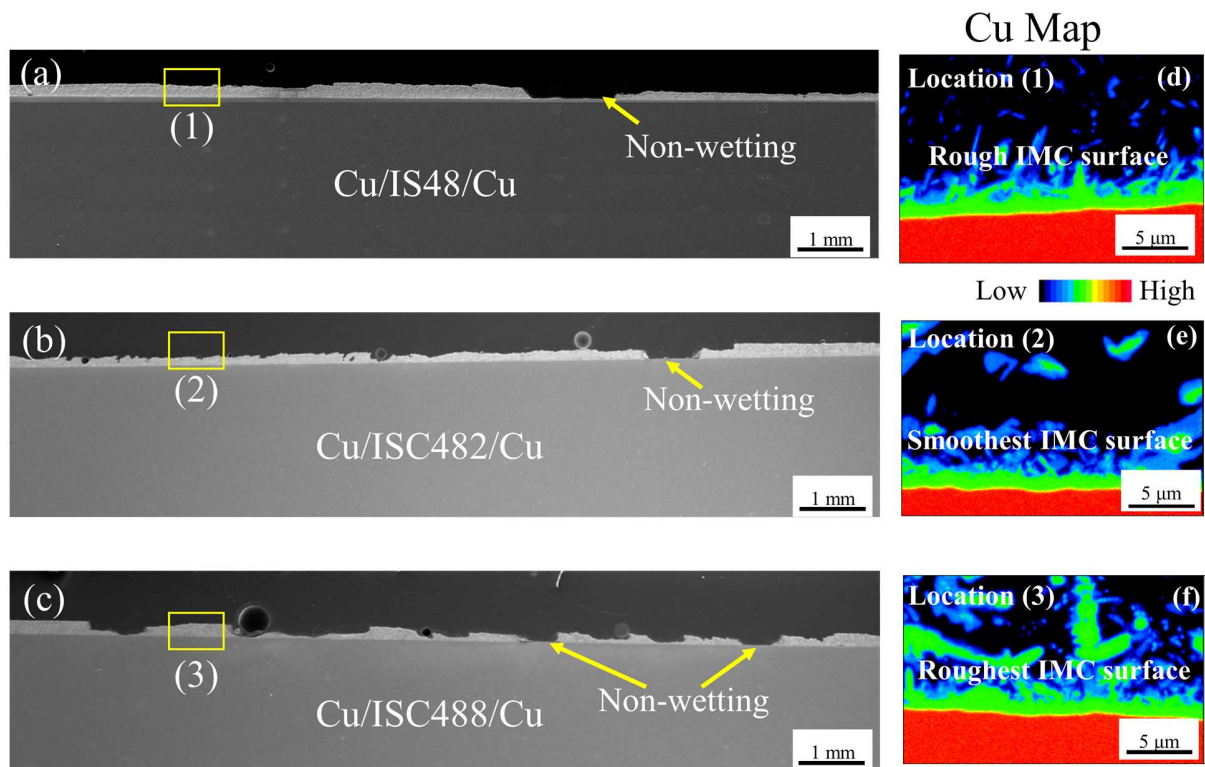
Figure 4.16 SEM images of typical cross-sectional fractured samples of (**a**) Cu/IS48/Cu, (**b**) Cu/ISC482/Cu, and (**c**) Cu/ISC488/Cu joints. (**d–f**) EPMA images of typical locations (1, 2, and 3) at the interface of the fractured samples.
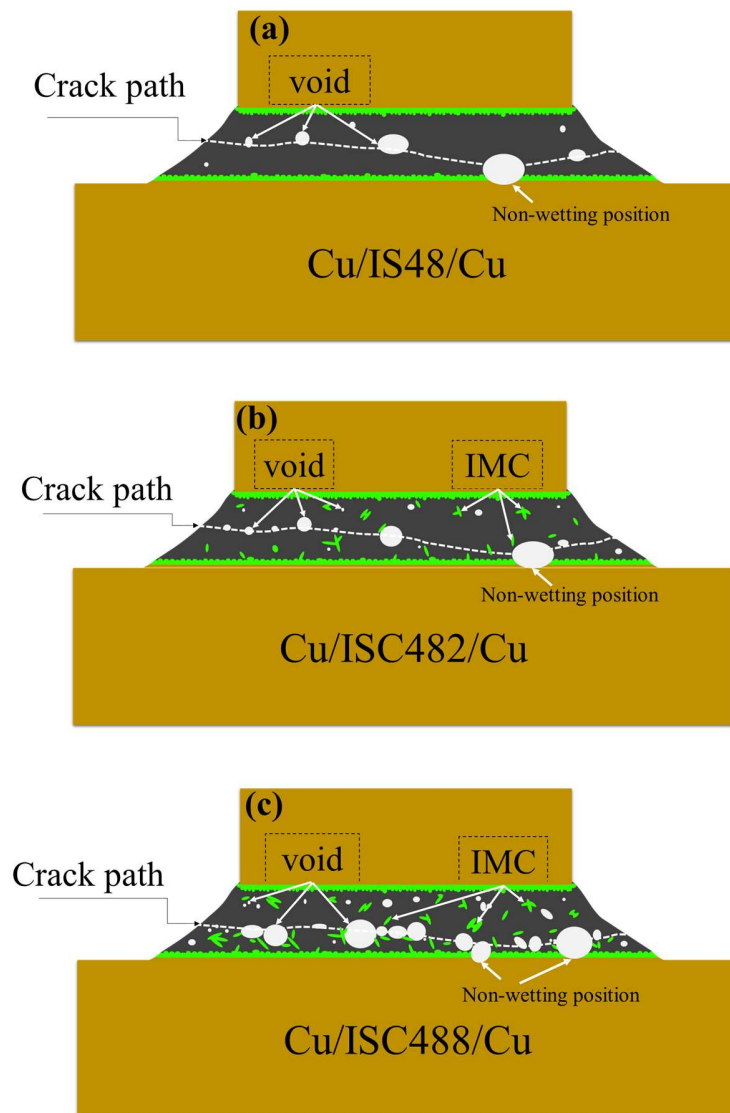
Figure 4.17 Schematics of crack propagation and void distribution in (**a**) Cu/IS48/Cu, (**b**) Cu/ISC482/Cu, and (**c**) Cu/ISC488/Cu joints.

4.4 Conclusions

In this chapter, the effects of the addition of 2.0 and 8.0 wt.% Cu on the wettability, microstructure evolution, and shear strength of In-Sn-xCu/Cu joints were analysed and compared with those of In-48Sn/Cu joints. Conclusions are set out below and the results are summarised in **Table 4.4**.

- The addition of Cu increases the contact angle of the In-Sn-xCu alloys on the Cu substrate because of the higher viscosity of liquid Cu than In and Sn. However, both

the ISC alloys exhibit acceptable wettability, as indicated by the formation of a continuous $Cu_6(In,Sn)_5 + Cu_(In,Sn)_2$ IMC layer at the In-Sn-xCu/Cu interface.

- The In-Sn-2.0Cu/Cu joint exhibits a fine microstructure with small numbers of voids and (Cu,In,Sn)-IMC in the alloy matrix. It also has the smoothest and thinnest IMC layer at the interface; this enhances the shear strength of the alloy joint (16.5 MPa) when compared to the In-Sn/Cu joint (14.5 MPa).
- Conversely, the In-Sn-8.0Cu/Cu joint has the highest number of voids in the alloy matrix and has a thick and rough IMC layer at the interface, which reduces the shear strength of the alloy joint (14.3 MPa).

Table 4.4 The summarized results data of chapter 4.

Alloy joint	Wettability (Contact angle)	IMC layer (Thickness)	Shear strength
Cu/IS48/Cu	16˚	$Cu_6(In, Sn)_5 + Cu(In, Sn)_2$ (6.6 μm)	14.5 MPa
Cu/ISC482/Cu	25˚	$Cu_6(In, Sn)_5 + Cu(In, Sn)_2$ **Thinner** (5.8 μm)	**Better** (16.5 MPa)
Cu/ISC488/Cu	37˚	$Cu_6(In, Sn)_5 + Cu(In, Sn)_2$ (6.4 μm)	Equal (14.3 MPa)

Reference

1. Abtew, M.; Selvaduray, G. Lead-free solders in microelectronics. *Mater. Sci. Eng. R Reports* **2000**, *27*, 95–141, doi:10.1016/S0927-796X(00)00010-3.

2. Kim, D.-G.; Jung, S.-B. Interfacial reactions and growth kinetics for intermetallic compound layer between In–48Sn solder and bare Cu substrate. *J. Alloys Compd.* **2005**, *386*, 151–156.

3. Shohji, I.; Fujiwara, S.; Kiyono, S.; Kobayashi, K.F. Intermetallic compound layer formation between Au and In-48Sn solder. *Scr. Mater.* **1999**, *40*, 815–820, doi:10.1016/S1359-6462(99)00007-X.

4. Mannan, S.H.; Clode, M.P.; Dagher, M. Study of intermetallic crystal growth between Nb and molten 52In-48Sn solder. *J. Electron. Mater.* **2005**, *34*, 125–131, doi:10.1007/s11664-005-0222-2.

5. Koo, J.A.M.; Jung, S.B. Reliability of in-48Sn solder/Au/Ni/Cu BGA packages during reflow process. *J. Electron. Mater.* **2005**, *34*, 1565–1572, doi:10.1007/s11664-005-0166-6.

6. Koo, J.M.; Yoon, J.W.; Jung, S.B. Interfacial reactions between In-48Sn solder and electroless nickel/immersion gold substrate during reflow process. *Surf. Interface Anal.* **2006**, *38*, 426–428, doi:10.1002/sia.2193.

7. J. L. FREER and J. W. MORRIS, J. Microstructure and Creep of Eutectic Indium/Tin on Copper and Nickel Substrates, Journal of electronic materials. **1992**, *21*, 647–652.

8. Goldstein, J.L.F.; Morris, J.W. The Effect of Substrate on the Microstructure and Mechanical Behavior of Eutectic Indium-Tin. *MRS Proc.* **1994**, *323*, doi:10.1557/proc-323-159.

9. Chuang, T.H.; Yu, C.L.; Chang, S.Y.; Wang, S.S. Phase identification and growth kinetics of the intermetallic compounds formed during In-49Sn/Cu soldering reactions. *J. Electron. Mater.* **2002**, *31*, 640–645, doi:10.1007/s11664-002-0136-1.

10. Sobczak, N.; Kudyba, A.; Nowak, R.; Radziwill, W.; Pietrzak, K. Factors affecting wettability and bond strength of solder joint couples. *Pure Appl. Chem.* **2007**, *79*, 1755–1769, doi:10.1351/pac200779101755.

11. Kumar, G.; Prabhu, K.N. Review of non-reactive and reactive wetting of liquids on surfaces. *Adv. Colloid Interface Sci.* **2007**, *133*, 61–89, doi:10.1016/j.cis.2007.04.009.

12. Dogan, A.; Arslan, H. Thermophysical properties of Cu–In–Sn liquid Pb-free alloys viscosity and surface tension. *Philos. Mag.* **2017**, 1–18, doi:http://dx.doi.org/10.1080/14786435.2017.1392053.

13. Yakymovych, A.; Vus, V.; Mudry, S. Viscosity of liquid Cu-In-Sn alloys. *J. Mol. Liq.* **2016**, *219*, 845–850, doi:10.1016/j.molliq.2016.04.055.

14. Noor, E.E.M.; Sharif, N.M.; Yew, C.K.; Ariga, T.; Ismail, A.B.; Hussain, Z. Wettability and strength of In-Bi-Sn lead-free solder alloy on copper substrate. *J. Alloys Compd.* **2010**, *507*, 290–296, doi:10.1016/j.jallcom.2010.07.182.

15. Zang, L.; Yuan, Z.; Zhao, H.; Zhang, X. Wettability of molten Sn–Bi–Cu solder on Cu substrate. *Mater. Lett.* **2009**, *63*, 2067–2069, doi:https://linkinghub.elsevier.com/retrieve/pii/S0167577X0900487X.

16. Tan, C.Y.; Mohd Arif Anuar Mohd Salleh; Saud, N. The study of interfacial reaction between SnAgCu (SAC) lead-free solder alloys and copper substrate: A short review. *IOP Conf. Ser. Mater. Sci. Eng.* **2020**, *864*, doi:10.1088/1757-899X/864/1/012182.

17. Le Han, D.; Shen, Y.; He, S.; Nishikawa, H. Effect of Cu addition on the microstructure and mechanical properties of In–Sn-based low-temperature alloy. *Mater. Sci. Eng. A* **2021**, *804C*, 1–8, doi:10.1016/j.msea.2021.140785.

18. LIU, X.J.; LIU, H.S.; OHNUMA, I.; KAINUMA, R.; ISHIDA, K.; ITABASHI, S.; KAMEDA, K.; YAMAGUCHI, and K. Experimental determination and thermodynamic calculation of the phase equilibria in the Cu-In-Sn system. *J. Electron. Mater.* **2001**, *30*, 1093–1103, doi:10.3139/146.111135.

19. Riania, P.; Gabriele Cacciamania, Nadia Parodia, Gabriella Borzonea, Rinaldo Marazzaa, Francesca Nannib, G.G. Phase equilibria in the In–Sn-rich part of the Cu–In–Sn ternary system. *J. Alloys Compd.* **2009**, *487*, 90–97.

20. Yang, F.; Ni, F. Effect of cooling rate on the solidification of Zn-5wt%Al alloy. *Adv. Mater. Res.* **2012**, *366*, 502–505, doi:10.4028/www.scientific.net/AMR.366.502.

21. Humpton, G.; M.Jacobson, D. *Principles of Soldering*; 2004; ISBN 987-0-07-351108-5.

22. Seah, K.H.W.; Hemanth, J.; Sharma, S.C. Effect of the cooling rate on the dendrite arm spacing and the ultimate tensile strength of cast iron. *J. Mater. Sci.* **1998**, *33*, 23–28, doi:10.1023/A:1004321007806.

23. Lee, T.-K.; Bieler, T.R.; Kim, C.-U.; Ma, H. *Fundamentals of Lead-Free Solder Interconnect Technology - From Microstructure to Reliability*; 2015; ISBN 978-1-4614-9265-8.

24. Susan, D.F.; Rejent, J.A.; Grant, R.P.; Vianco, P.T. The Solidification Behavior and Microstructure of In-Sn-Cu Solder Alloys with Low Cu. *4th Int. Brazing Solder. Conf.* **2009**, 1–6.

25. Shang, P.J.; Liu, Z.Q.; Li, D.X.; Shang, J.K. Phase identification of intermetallic compounds formed during in-48Sn/Cu soldering reactions. *2009 Int. Conf. Electron. Packag. Technol. High Density Packag. ICEPT-HDP 2009* **2009**, *3*, 597–600, doi:10.1109/ICEPT.2009.5270680.

26. Lin, S.K.; Chung, T.Y.; Chen, S.W.; Chang, C.H. 250 °C isothermal section of ternary Sn-In-Cu phase equilibria. *J. Mater. Res.* **2009**, *24*, 2628–2637, doi:10.1557/jmr.2009.0317.

27. Tian, F.; Liu, Z.Q.; Shang, P.J.; Guo, J. Phase identification on the intermetallic compound formed between eutectic SnIn solder and single crystalline Cu substrate. *J. Alloys Compd.* **2014**, *591*, 351–355, doi:10.1016/j.jallcom.2013.12.257.

28. Yazzie, K.E.; Fei, H.E.; Jiang, H.; Chawla, N. Rate-dependent behavior of Sn alloy-Cu couples: Effects of microstructure and composition on mechanical shock resistance. *Acta Mater.* **2012**, *60*, 4336–4348, doi:10.1016/j.actamat.2012.04.018.

29. Mohamed Anuar, R.A.; Osman, S.A. The formation of intermetallic layer structure of SAC405/Cu and SAC405/ENImAg solder joint interfaces. *Solder. Surf. Mt. Technol.* **2021**, *33*, 75–85, doi:10.1108/SSMT-03-2019-0009.

30. Shin, C.K.; Huh, J.Y. Effect of Cu-containing solders on the critical IMC thickness for the shear strength of BGA solder joints. *Proc. Electron. Packag. Technol. Conf. EPTC* **2000**, 406–411, doi:10.1109/EPTC.2000.906408.

31. Xinmeng, Z.; Yuefeng, L.; Jun, Z.; Mingming, S.; Bobo, Y.; Yang, L.; Chunfeng, G.; Rongrong, H. Effect of Soldering Temperature on the Reliability of Sn-Ag-Cu Lead-Free Solder Joints. *J. Electron. Mater.* **2021**, *50*, 869–880, doi:10.1007/s11664-020-08715-5.

32. Bušek, D.; Dušek, K.; Růžička, D.; Plaček, M.; MacH, P.; Urbánek, J.; Starý, J. Flux effect on void quantity and size in soldered joints. *Microelectron. Reliab.* **2016**, *60*, 135–140, doi:10.1016/j.microrel.2016.03.009.

33. Sun, L.; Chen, M. he; Zhang, L.; He, P.; Xie, L. sheng Recent progress in SLID bonding in novel 3D-IC technologies. *J. Alloys Compd.* **2020**, *818*, 152825, doi:10.1016/j.jallcom.2019.152825.

Chapter 5

Effect of isothermal ageing on the properties of In-Sn-xCu alloys and their joints on a Cu substrate

5.1 Introduction

In Chapters 3 and 4, the addition of Cu (2.0 and 8.0 wt.%) was shown to refine the microstructure of an as-cast In52Sn48 alloy and its joint on a Cu substrate. However, in order to serve the function of joining electronic components to a printed wiring board circuit, solder alloys are used at high homologous temperatures (usually exceeding 0.3-0.5 times the melting temperature, T_m, of the alloy). At this temperature, diffusion processes are very active. As a result, the microstructure of solder alloys is unstable at normal operating, and storage temperatures for electronic equipment. As-cast microstructures coarsen over time after the assembly is completed and, within the joints, the interphase spacing increases. These changes, in turn, influence the mechanical properties and in-service performance of a solder alloy [1]. Therefore, in this chapter, a thermal ageing test was conducted on the IS48, ISC482, and ISC488 alloys and their joints on a Cu substrate to evaluate changes in their microstructure and mechanical properties.

5.2 Experimental procedure

5.2.1 Materials

The IS48, ISC482, and ISC488 alloys were fabricated as described in Section 3.2.1 of Chapter 3. Then, the alloy bars were machined into dog-bone shaped specimens (**Figure 5.1a**) by wire electric discharge machining (Soldick AG 360L, Japan) to prepare the tensile samples for the ageing test. The Cu/IS48/Cu, Cu/ISC482/Cu, and Cu/ISC488/Cu joints (**Figure 5.1b**) were fabricated using the procedure described in Section 4.2.1 of Chapter 4.

5.2.2. Ageing condition and process

The working temperatures of some electronics devices are listed in **Table 5.1** [1]. Based on the working temperatures and melting temperatures of alloys, the ageing temperature was set at approximately 0.85 T_m (60°C). The tensile samples and alloy joint samples were aged in an oil bath at a temperature of 60°C for 168, 504, and 1008 h, as shown in **Figure 5.1c-d**. The number of samples for the thermal ageing test is summarised in **Table 5.2**. After ageing, the samples were removed from the oil bath and cooled to room temperature. The oil on the sample surfaces was removed with ethanol.
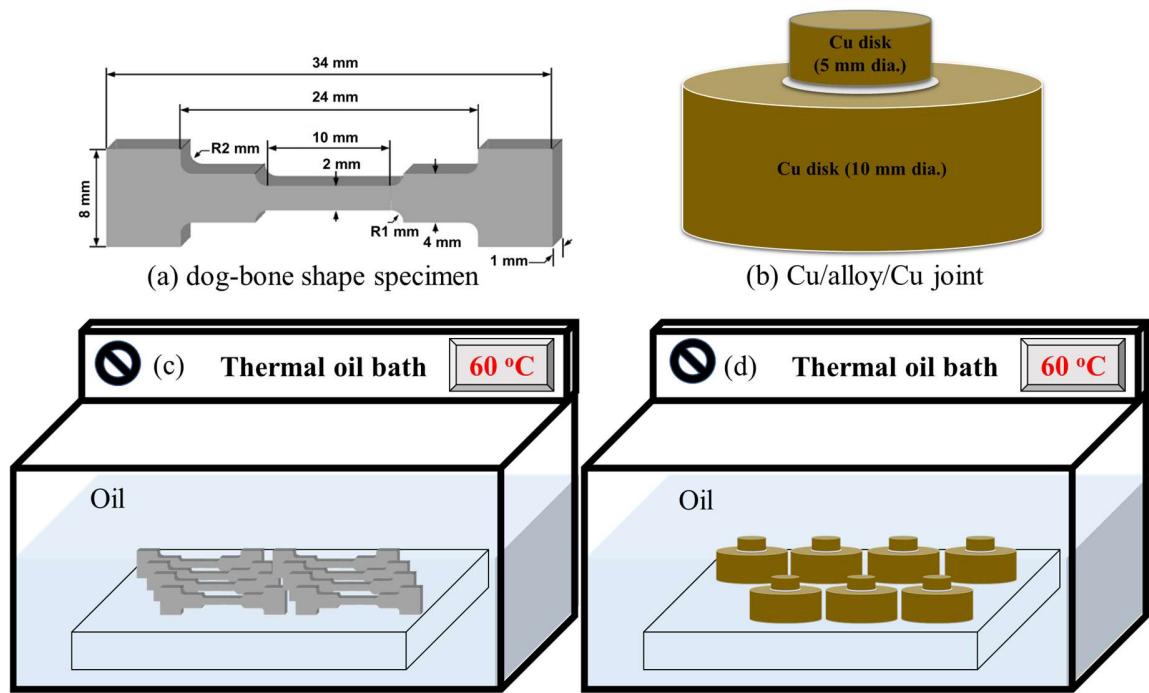
Figure 5.1 The geometry of (a) dog-bone shape specimen, (b) Cu/alloy/Cu joint, and the schematic of thermal ageing test in oil bath.

Table 5.1 Working temperature condition of electronic devices (Worst case use environments for products in the field based on IPC-SM-785) [1].

Use category	Minimum extreme temperature (°C)	Maximum extreme temperature (°C)
Consumer electronics	0	+60
Computers	+15	+60

5.2.3 Characterisation methods

The tensile strength of the alloys was measured using a universal tensile machine (Autograph AG-X, Shimadzu, Japan) at a strain rate of 5×10^{-4} s^{-1}. Then, SEM (SU-70, Hitachi, Japan) was used to examine the fracture surfaces of the alloys after the tensile test. The shear strength of the joint was determined at room temperature (20°C) using a shear test machine (STR-1000, Rhesca, Japan) operated at a crosshead rate of 1 mm/min.

Table 5.2 Number of samples for thermal ageing test at 60 °C.

Alloy/ alloy joint	Number of samples		
	168 h	504 h	1008 h
IS48 alloy	8	8	8
ISC482 alloy	8	8	8
ISC488 alloy	8	8	8
Cu/IS48/Cu joint	7	7	7
Cu/IS482/Cu joint	7	7	7
Cu/ISC488/Cu joint	7	7	7

The shear strength was calculated by dividing the maximum shear force at the failure site by the area of the alloy joint. The average shear strength was calculated on six Cu/alloy/Cu joints for the IS48, ISC482, and ISC488 alloys. To investigate the microstructure of the alloys and the interfaces of the alloy joints, the alloy joint samples were sectioned. Both alloys and cross-sectional joint samples were polished with SiC grit papers of #150, #400, #800, #1200, and #2000, after which fine polishing was performed with a 1.0 μm alumina suspension (Buehler, USA). Then, the samples were analysed by SEM (SU-70, Hitachi, Japan). Field-emission electron probe microanalysis (FE-EPMA; JXA-8530F JEOL, Japan) was used to identify the elemental distributions of the alloys and fracture surface samples. ImageJ software was used to measure the fractions of the phases and the eutectic spacing of the β-phase. Four EPMA images for each alloy were used for this measurement (total area of picture is approximately T_a =33.000 μm^2 for each image). Total number of γ–phase (n) in each image was also counted, the average γ phase size (γ_a) was measured and calculated, and then the total γ-phase area (T_γ) was calculated by multiplying the average γ-phase size by the total number of γ-phases per each EPMA image. After that, the total β-

phase area (T_β) per each image was calculated by subtracting the total area of the γ-phases from the total area of the image ($T_\beta = T_a - T_\gamma$). The β/γ ratio was then determined by dividing the total measured β-phase area by the total measured γ-phase area (β/γ = T_β / T_γ). The eutectic spacing is the distance between two consecutive lamellae of the β-In_3Sn phase, and the average values were calculated based on the measured results of 60 eutectic spacings for each alloy.

5.3 Characteristics of bulk alloys

5.3.1 Microstructure

Figure 5.2 shows the backscattered electron (BSE) and mapping images of the IS48 alloy before (as-cast) and after (168, 504, 1008 h) ageing, obtained using EPMA. There are two main β (In-rich) and γ (Sn-rich) phases in the alloy matrixes. Both In and Sn have a high homologous temperature at the ageing temperature (0.78 and 0.66, respectively). Therefore, In and Sn atoms easily diffuse through the grain boundary of β and γ during isothermal ageing [1]. Moreover, it can be seen from the In-Sn phase diagram (**Figure 1.7**) that the solubility of Sn in the In-rich phase decreases significantly as the temperature decreases from the melting point to room temperature, while the solubility of In in the Sn-rich phase is nearly constant at 28 at.% [2,3]. Normally, during solidification process such as casting, the alloy could get the non-equilibrium phases, and during heat-treatment process the phases tend to transform from non-equilibrium stage to equilibrium stage [4,5]. Therefore, in order to return to equilibrium of the β phase, Sn atoms tend to congregate in several regions of the β phase to form a precipitate of the new Sn-rich solid solution. This explains the presence of Sn-rich phase precipitates inside the In-rich matrix, which are clearly visible in the In-maps/Sn-maps in **Figure 5.2**. Moreover, due to the constant solubility of In in the Sn-rich phase, there is no precipitation of In inside the Sn-rich phase, and the Sn-rich phase remains continuous as is visible in the Sn-maps in **Figure 5.2**. The average grain size, and the β/γ ratio in the IS48 alloy before and after ageing, were measured by ImageJ software from EPMA mapping images, as shown in **Figure 5.3**. It should be noted that both β and γ phases increase in average grain size after thermal ageing, and the β phase increases faster than the γ phase. The average size of phase β was 340 μm^2 as-cast

condition, then this size increased by 19%, 33%, and 52% (519 μm^2) after 168, 504, and 1008 h of ageing, respectively. The average size of the γ phase was 272 μm^2 in the as-cast condition, then the γ phase size increased by 17%, 25%, and 41% (384 μm^2) after 168, 504, and 1008 h of ageing. In this study, the coarsening rate of the β (In-rich) and γ (Sn-rich) phases was calculated by dividing the difference in average phase size before and after ageing by the ageing time, as summarised in **Table 5.3**. Freer et al. [6] reported that the self-diffusion activation energies of In and Sn are 0.78 eV and 1.08 eV, respectively. Moreover, In has a higher homologous temperature (0.78) than Sn (0.66). Therefore, during ageing, In atoms diffuse more readily than Sn, resulting in the β phase increasing in size faster than the γ phase, as shown in **Figure 5.3** and **Table 5.3**.

Figure 5.2 Microstructure of IS48 alloy before and after ageing at 60 °C: (a) as-cast (b) 168 h, (c) 504 h, and (d) 1008h.
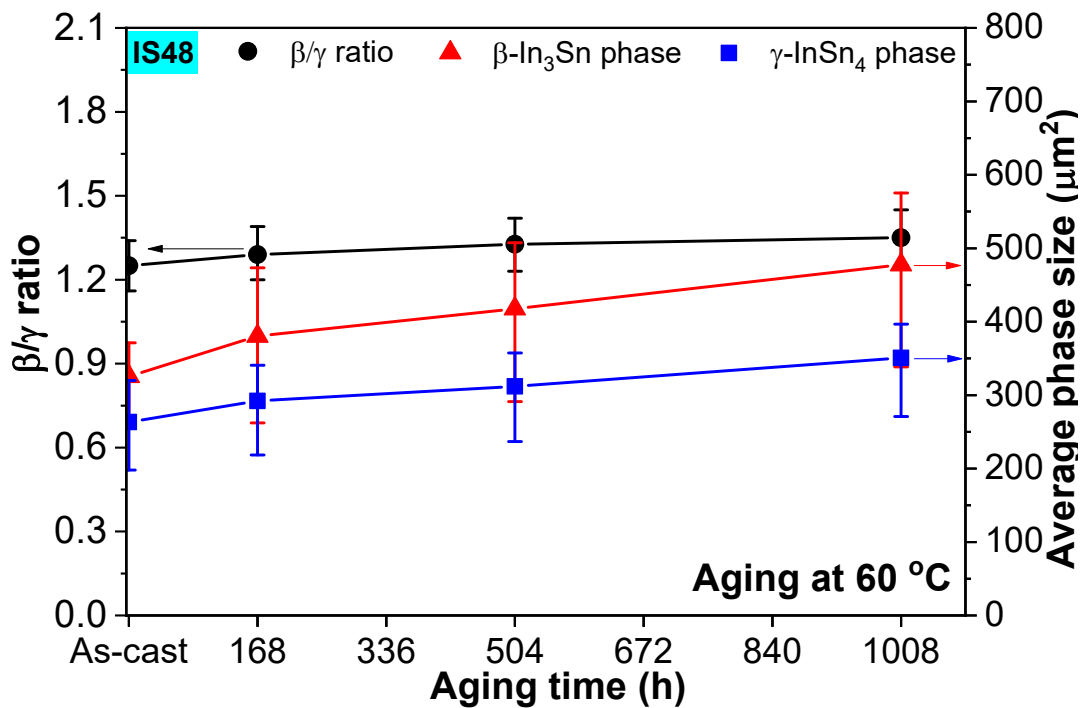
Figure 5.3 Average grain size and the β/γ ratio in IS48 alloy before and after thermal ageing.

Table 5.3 Coarsening rate of β (In-rich) and γ (Sn-rich) phase in IS48 alloy during ageing.

Phase	Coarsening rate ($\mu m^2 h^{-1}$)		
	168 h	**504 h**	**1008 h**
β (In-rich)	0.39	0.23	0.18
γ (Sn-rich)	0.27	0.14	0.11

The microstructure evolution of the ISC482 and ISC488 alloys before and after ageing are shown in **Figures 5.4** and **5.5**, respectively. The average grain size and the β/γ ratio in the ISC482 and ISC488 alloys before and after ageing were measured by ImageJ software from EPMA mapping images, as shown in **Figures 5.6** and **5.7**, respectively. As mentioned in Chapter 3, when Cu is added, the ternary (Cu,In,Sn)-IMC including η (cu-rich) + τ (Cu-poor) forms in the matrixes of the ISC482 and ISC488 alloys, refining the microstructure of these alloys in the as-cast condition, as shown in **Figures 5.4a** and **5.5a**.
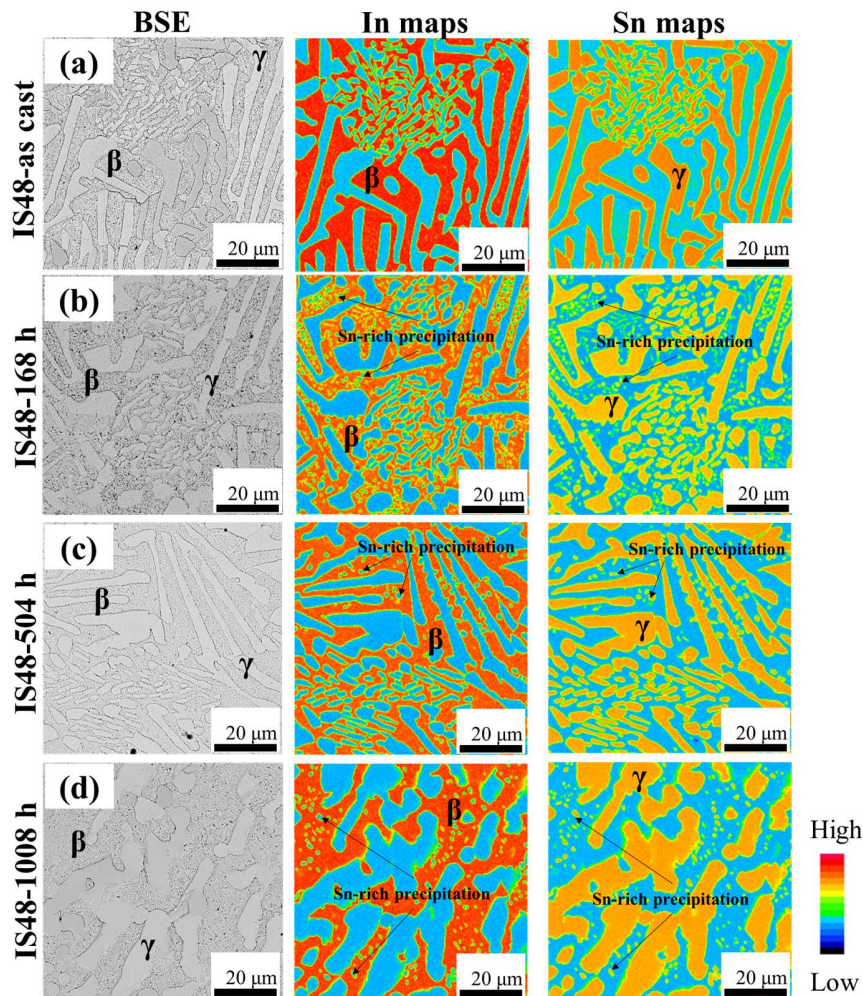
Figure 5.4 Microstructure of ISC482 alloy before and after ageing at 60 °C: (a) as-cast (b) 168 h, (c) 504 h, and (d) 1008h.

Moreover, Cu from the addition and the substrate is known to diffuse into the solder matrix during the heating process [2], and may affect the solidification process to produce a non-lamellar eutectic microstructure in both the ISC482 and ISC488 alloys. After 168-1008 h of thermal ageing, both the ISC482 and ISC488 alloys exhibit slight phase coarsening (**Figure 5.4b-d, Figure 5.5b-d**) compared to IS48 (**Figure 5.2b-d**). In the ISC482 alloy, the average size of phase γ was 227 μm^2 in the as-cast condition, then this size increased by 14%, 17%, and 20% (272 μm^2) after 168, 504, and 1008 h of ageing, respectively (**Figure 5.6**). The average size of the γ phase in the ISC488 alloy was 207 μm^2 in the as-

cast condition, then the γ phase size increased by 7%, 15%, and 16% (241 μm^2) after 168, 504, and 1008 h of ageing, respectively (**Figure 5.7**). It should be noted that, after thermal ageing, the ISC482 and ISC488 alloys have a more stable and finer microstructure than the IS48 alloy. In other words, the addition of Cu not only refines the microstructure (as-cast condition) but also reduces the microstructural coarsening (during thermal ageing) of the IS48 eutectic alloy.
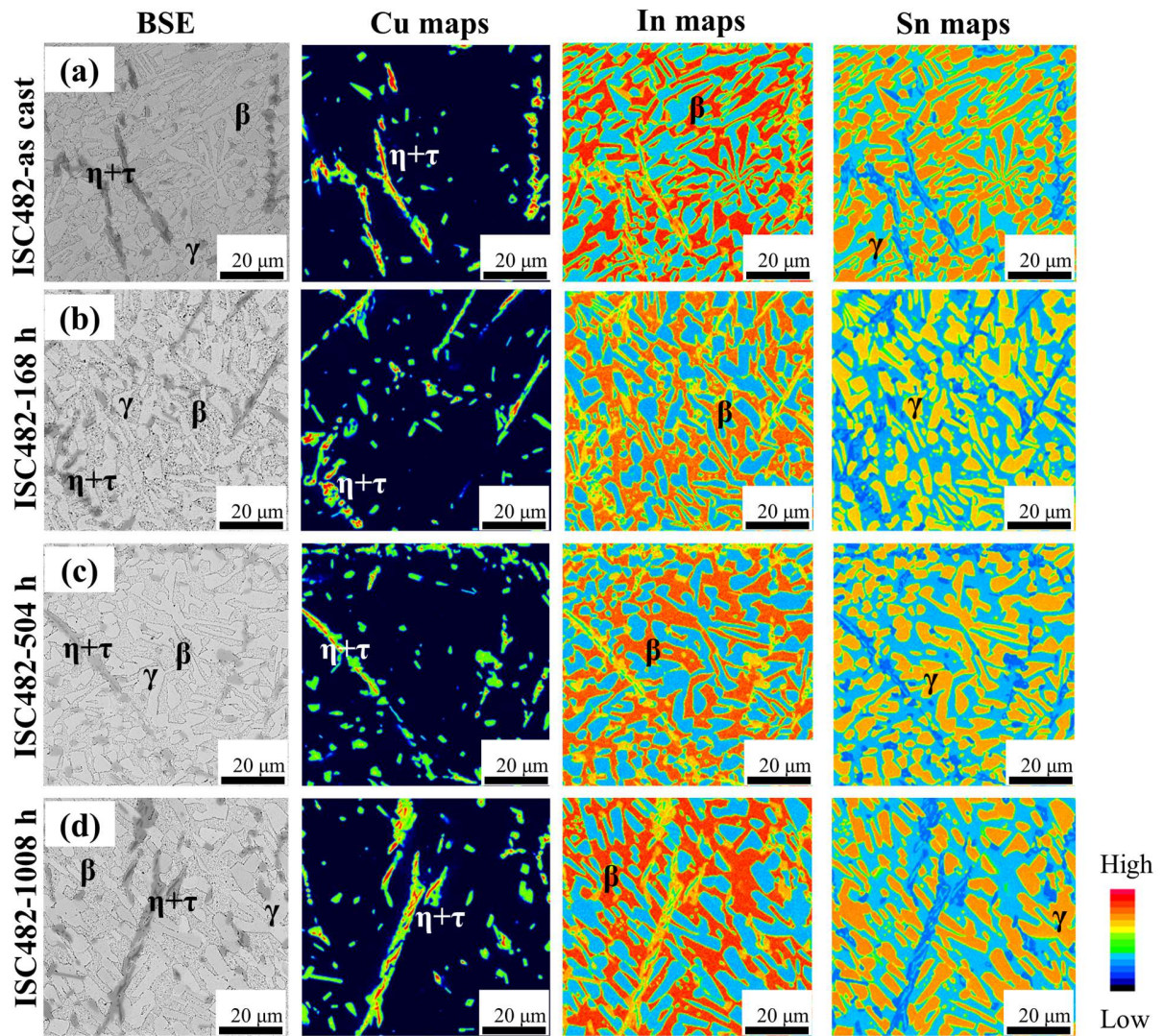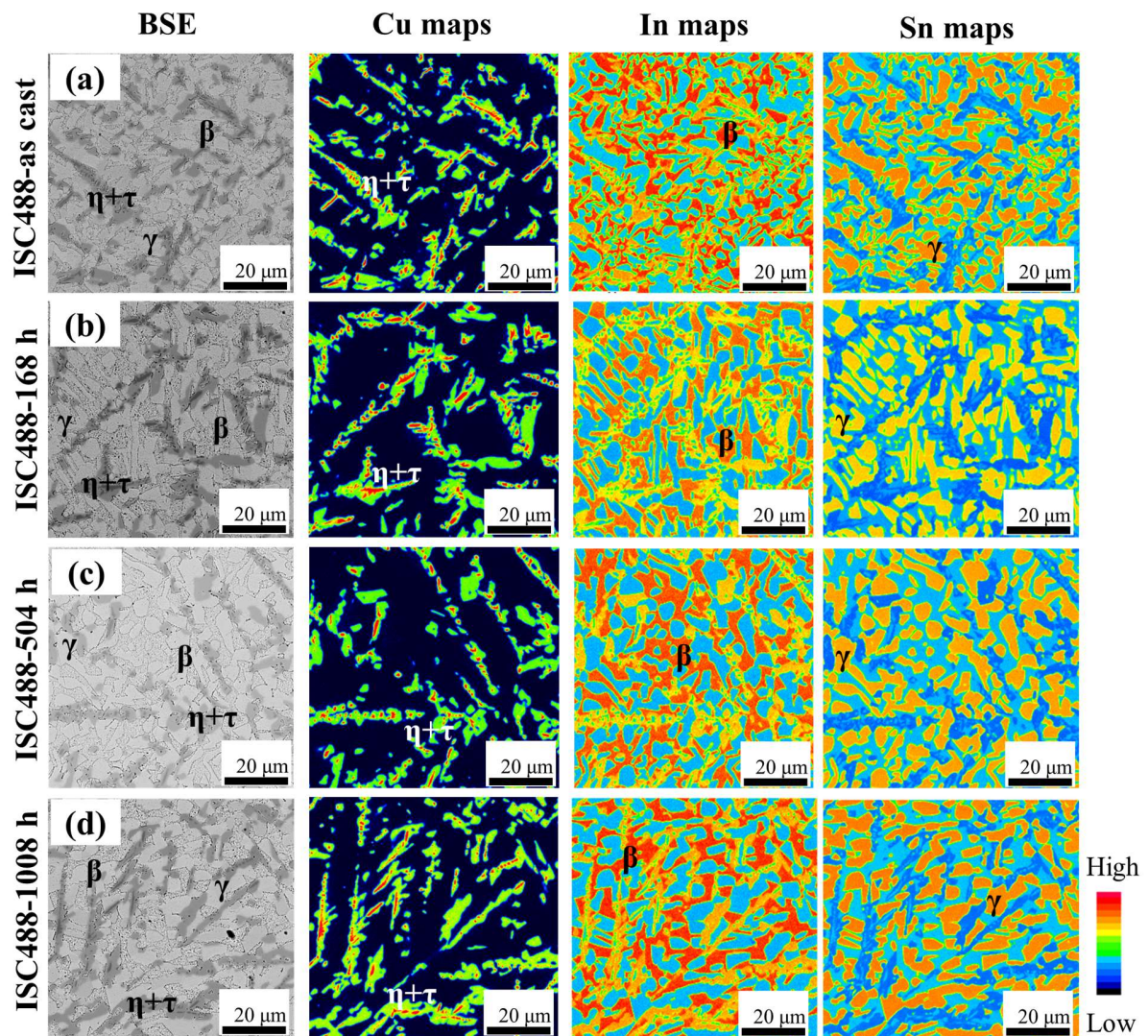

Figure 5.5 Microstructure of ISC488 alloy before and after ageing at 60 °C: (a) as-cast (b) 168 h, (c) 504 h, and (d) 1008h.
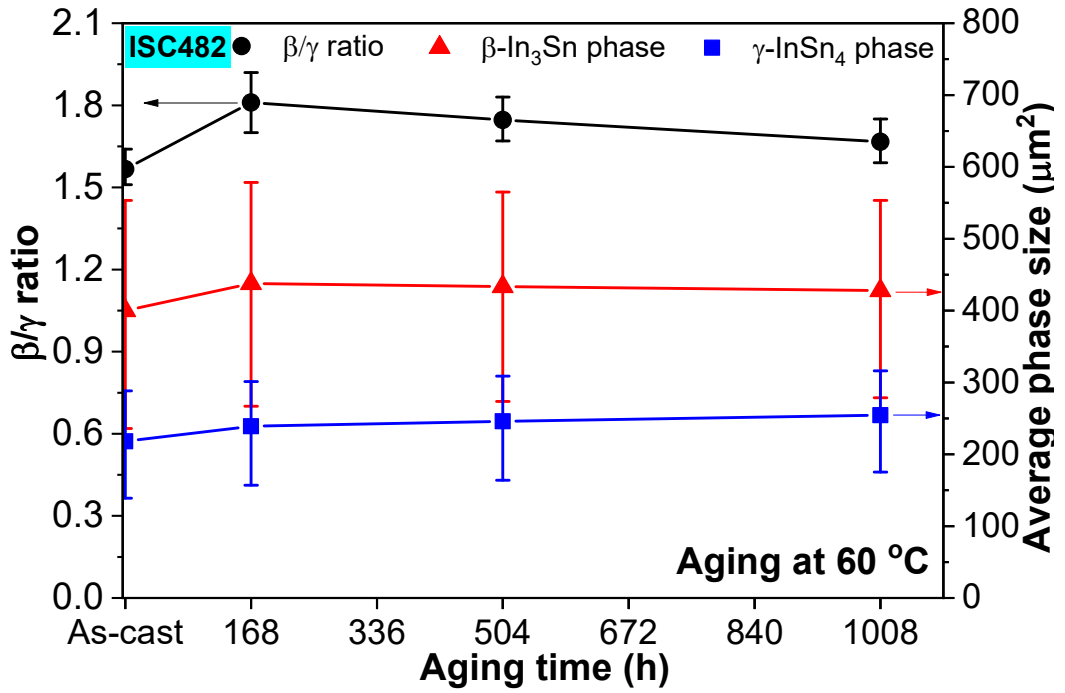
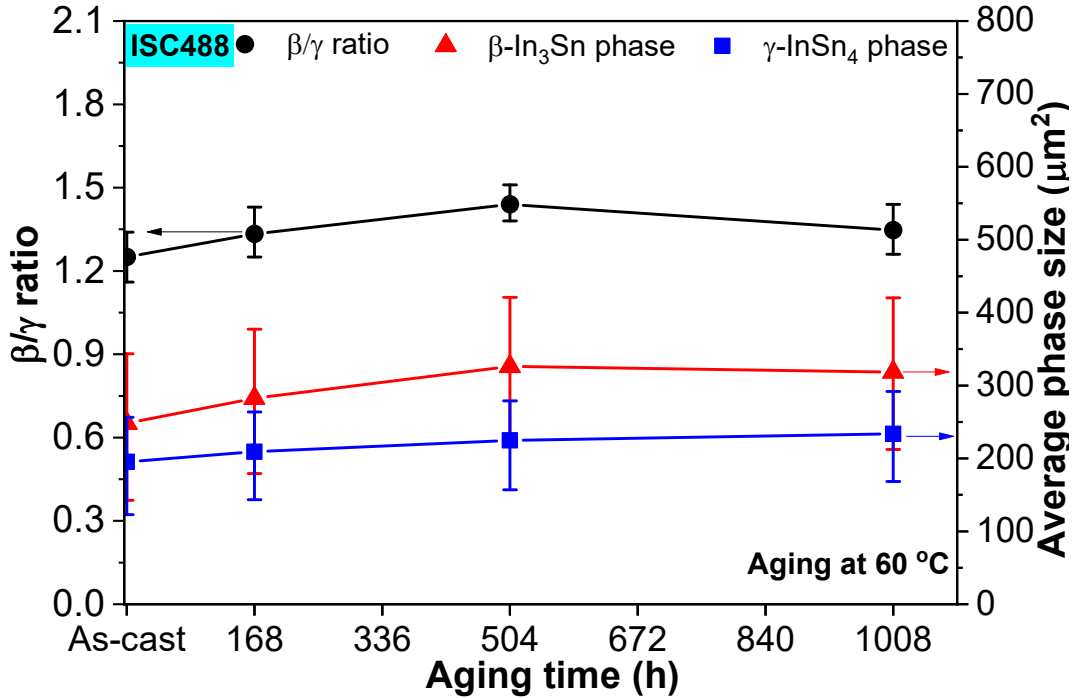**Figure 5.6** Average grain and the β/γ ratio in ISC482 alloy before and after thermal ageing.

Figure 5.7 Average grain and the β/γ ratio in ISC488 alloy before and after thermal ageing.

5.3.2 Mechanical properties

Figure 5.8 illustrates the representative stress-strain curves of the IS48, ISC482, and ISC488 alloys before and after thermal ageing. The stress-strain curves of both alloys are consistent with a typical ductile mode, while the ISC482 alloy shows the highest plastic deformation with extensional tailing (**Figure 5.8b**) compared to other alloys. Both alloys exhibit better elongation after thermal ageing. The average tensile strength and elongation of the IS48, ISC482, and ISC488 alloys were calculated based on eight samples for each alloy and ageing condition, as shown in **Figure 5.9**; the error bars show the maximum and minimum values. **Figure 5.9a** shows that all alloys exhibit a decrease in tensile strength after ageing, whereas the ISC482 and ISC488 alloys exhibit greater tensile strength than the IS48 alloy. After 168 h of ageing, the IS48 alloy exhibits a sharp decrease in tensile strength (14%), while the reduction in ISC482 and ISC488 alloys was 10% and 7%, respectively. After 1008 h of ageing, the IS48 alloy exhibited the greatest decrease in tensile strength (23% reduction), while the ISC488 alloy had only a 13% reduction. Also, **Figure 5.9b** demonstrates that elongation of the ISC alloys improves with the addition of Cu both before and after thermal ageing. The ISC482 alloy shows the greatest elongation of approximately 90%, 80%, and 70% after 168, 504, and 1008 h of ageing, respectively. This result is consistent with the stress-strain curve of the ISC482 alloy in **Figure 5.8b**. Meanwhile, the IS48 and ISC482 alloys exhibit a slight increase in elongation after 168-504 h of ageing (38-48%). Thereafter, both alloys exhibit equal elongation after 1008 h of ageing (44%), as the grain size and phase ratio in the alloy directly affect the tensile strength and elongation of the alloy [7–10]. Two basic theories explain the increase in strength of the ISC482 and ISC488 alloys both before and after ageing: smaller average grain size, and the presence of IMC in the solder matrix. Grain size refinement is well known to improve the yield strength of most metals. Yield strength is related to grain size by the Hall-Petch relationship [1,11]:

$$\sigma_y = \sigma_0 + k_y d^{-1/2} \qquad\qquad (1)$$

Here, σ_y is the yield stress (YS), d is the average grain size, $_0$ and k_y are the material constants.
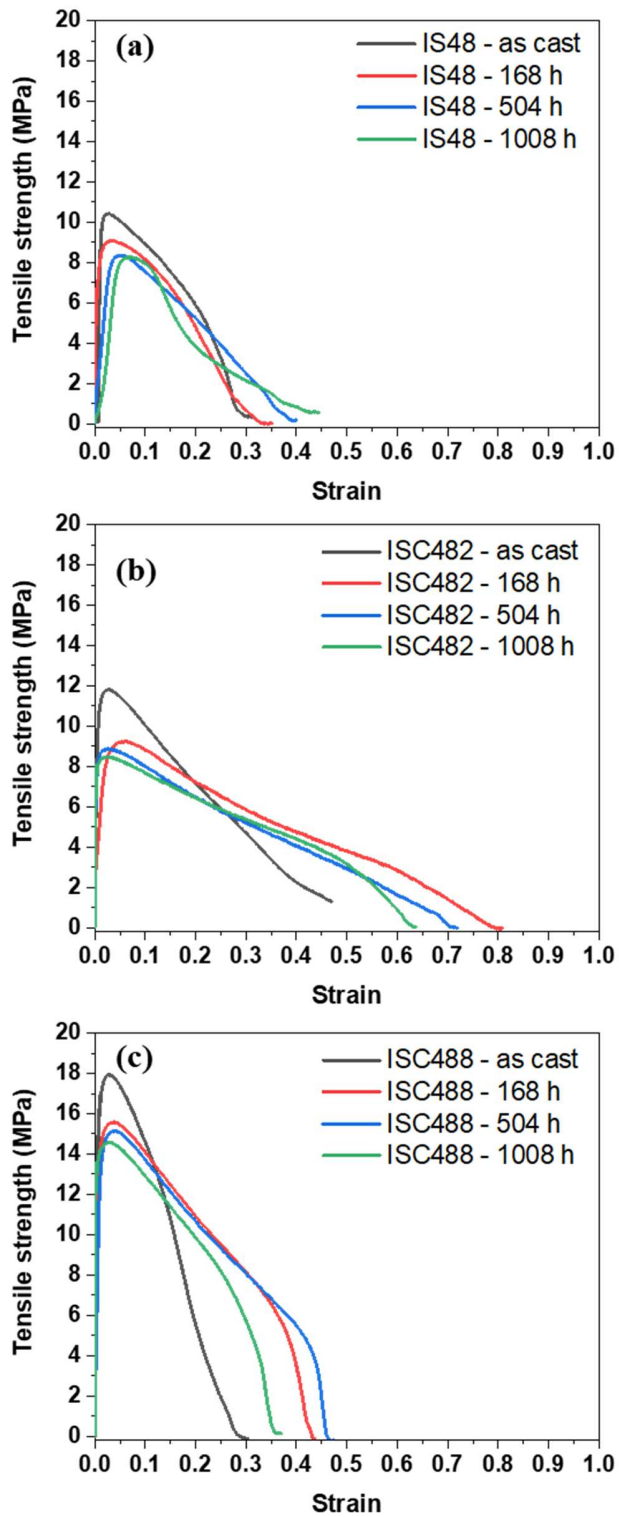
Figure 5.8 Typical strain-stress curves before and after thermal ageing at 60 °C of (a) IS48, (b) ISC482, and (c) ISC488 alloys.
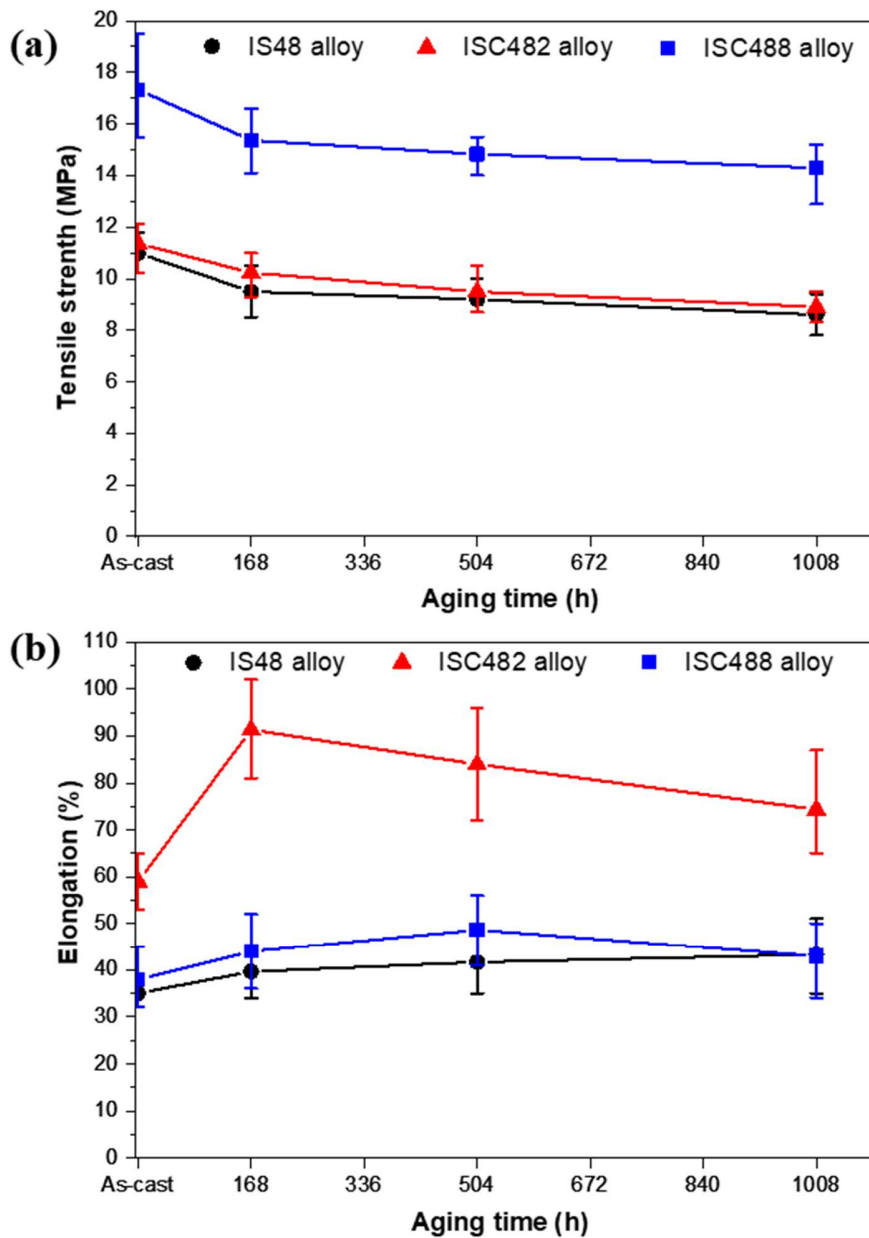
Figure 5.9 (a) Tensile strength, and (b) elongation before and after thermal ageing at 60 °C of IS48, ISC482, and ISC488 alloys.

Figures 5.6 and 5.7 show that both ISC482 and ISC488 alloys have smaller average grain sizes and more stable microstructures after ageing compared with IS48. The phenomenon where (Cu,In,Sn)-IMCs serve as obstacles to the dislocation movement and impede the grain boundary sliding and dispersion strengthening, can be explained by the Orowan mechanism [12]. As a result, both ISC482 and ISC488 alloys exhibit higher tensile strength

after ageing compared to that of the IS48 alloy. Furthermore, **Figures 5.3, 5.6, and 5.7** demonstrate that the ISC482 alloy has the highest soft β/hard γ ratio (1.6-1.8), both before and after ageing, and so has the greatest elongation. Meanwhile, the IS48 and ISC488 alloys have a phase ratio β/γ in the range 1.2-1.4, and so the elongation shown is similar.

5.3.3 Fracture mode

   Figure 5.10 presents the fracture modes and fracture surfaces of the IS48, ISC482, and ISC488 alloys after the tensile test in the as-cast condition. The IS48 and ISC488 alloys exhibit a similar fracture mode with a planar stress fracture on inclined planes and sharp edges on the fracture surface, which can be ascribed to the transgranular fracture internal phases (**Figure 5.10a** and **c**). The ISC482 alloy exhibits the highest density of plastic deformation with V-shaped necking areas observed on both of the broken sides (**Figure 5.10b**). This fracture behaviour is consistent with the mechanical results in **Figure 5.9b**, in which the ISC482 alloy has the highest elongation of the alloys.
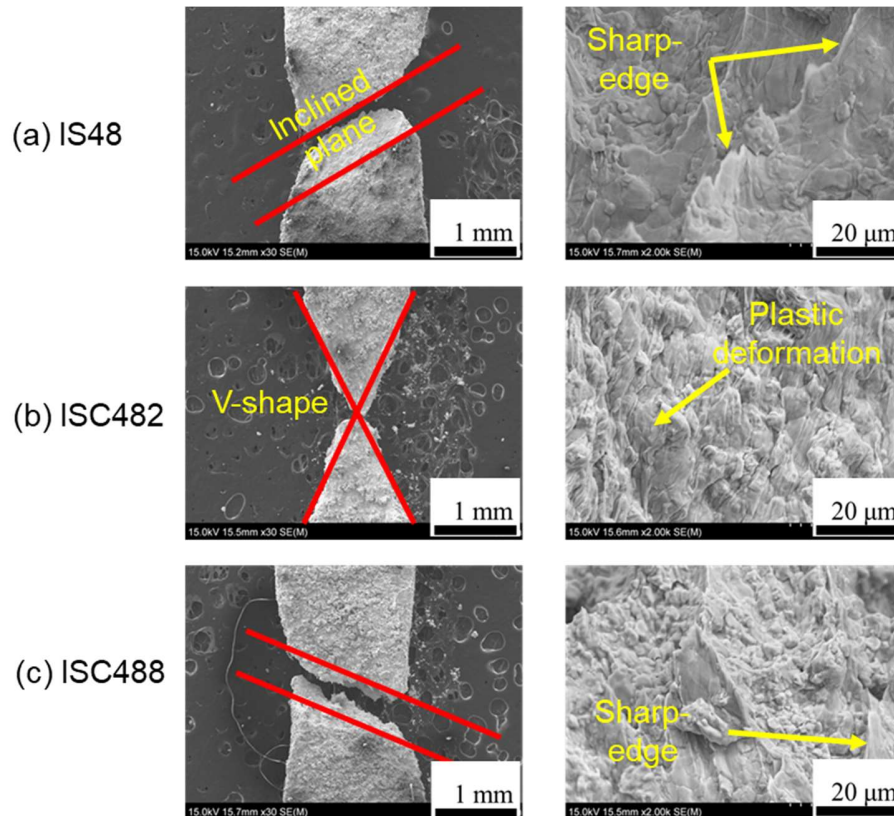
Figure 5.10 Fracture surfaces of tensile test samples of: (a) IS48, (b) ISC482, and (c) ISC488 alloys before ageing.

After 168-1008 h of ageing, both alloys showed ductile fracture behaviour similar to the as-cast condition (**Figures 5.11-5.13**). IS48 and ISC488 alloys show an inclined fracture, and many dimples appear on the fracture surface. Sharp edges represent tearing within phases and at the phase boundaries. The size of the dimples increases with ageing time, which is compatible with the coarsening of the phase after ageing as discussed above. On the other hand, the ISC482 alloy exhibits high-plastic fracture behaviour with V-shaped necking. However, the opened-V-shaped angle of the tensile test samples after ageing (**Figure 5.11b-5.13b**) was smaller than that of the fracture samples before ageing (**Figure 10b**). The fracture surface appears to have many overlapping phase locations, and the phase tends to be stretched and elongated under the action of tensile force. Thus, traces of phase slip appear on the fracture surface of the tensile samples of the ISC482 alloy; these results further demonstrate the high elongation of the ISC482 alloy after ageing, as shown in **Figure 5.9b**.
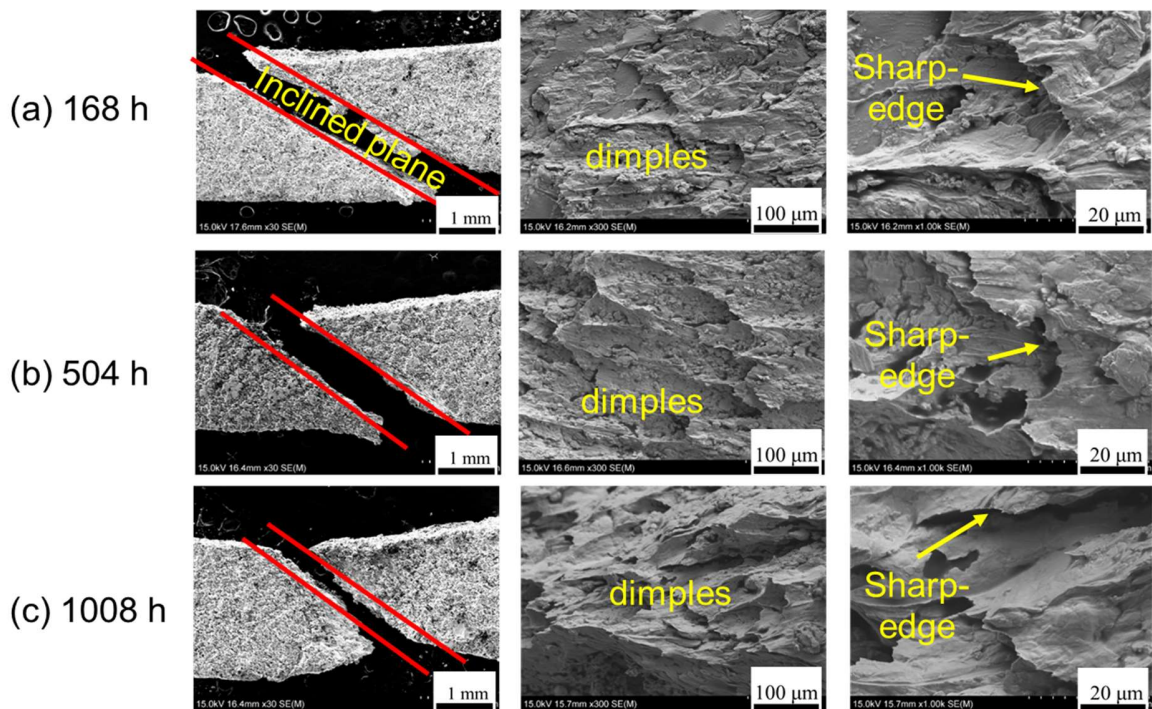
Figure 5.11 Fracture surfaces of tensile test samples of IS48 eutectic alloy after thermal ageing: (a) 168 h, (b) 504 h, and (c) 1008 h with different magnifications view.
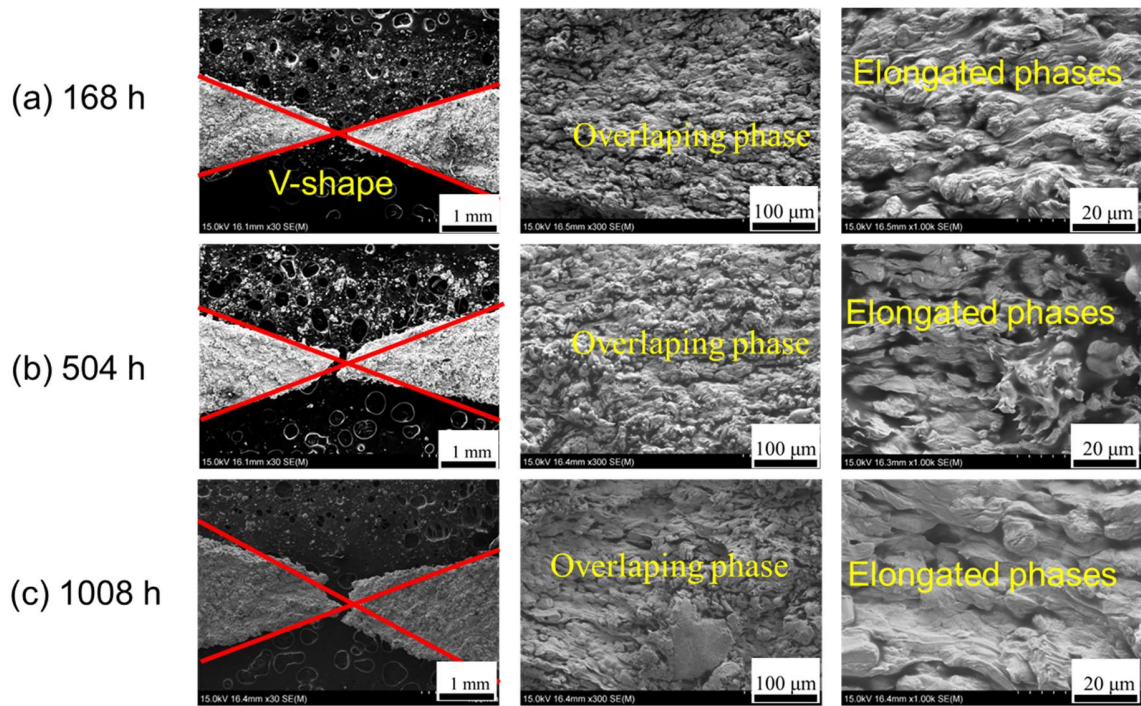
Figure 5.12 Fracture surfaces of tensile test samples of ISC482 alloy after thermal ageing: (a) 168 h, (b) 504 h, and (c) 1008 h with different magnifications view.
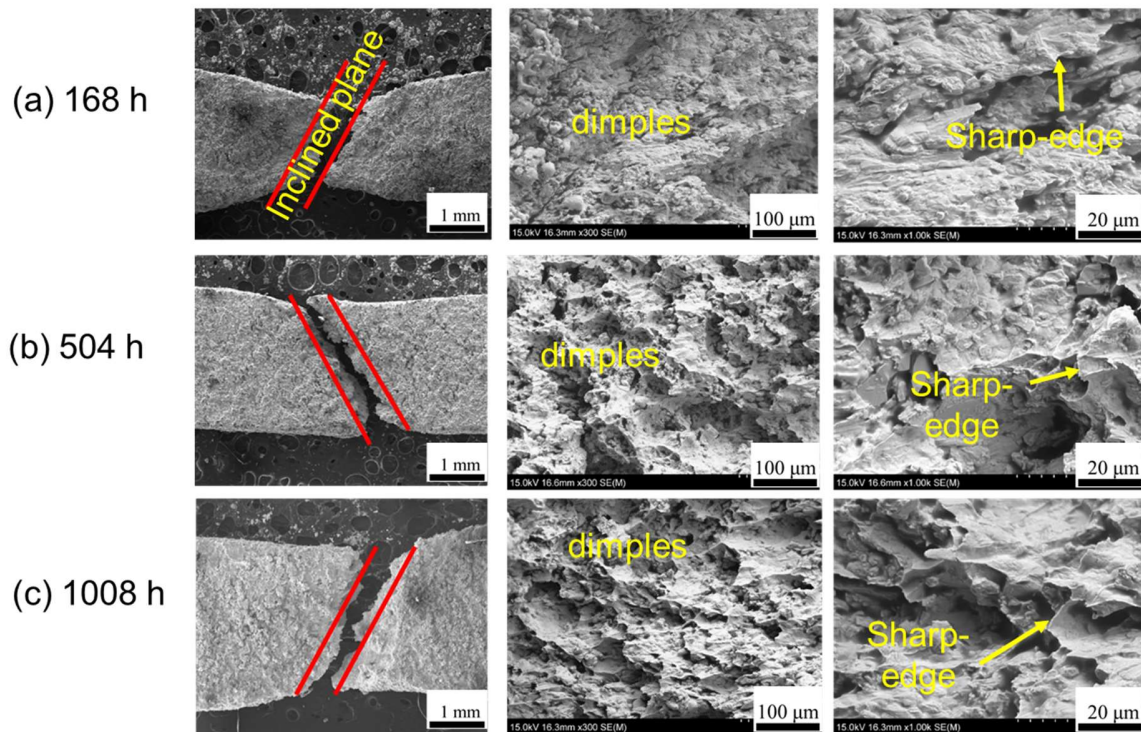
Figure 5.13 Fracture surfaces of tensile test samples of ISC488 alloy after thermal ageing: ((a) 168 h, (b) 504 h, and (c) 1008 h with different magnifications view.

5.4 Solder joints

5.4.1 Microstructure

The microstructure evolution before and after thermal ageing of Cu/IS48/Cu, Cu/ISC482/Cu, and Cu/ISC488/Cu alloy joints is presented in **Figures 5.14-5.16**, respectively. The two main β-(In-rich) and γ (Sn-rich) phases and (Cu,In,Sn)-IMC in the alloy matrixes, were determined in Chapter 4, and can be seen in the cross-sectional backscattered electrons (BSE) and EPMA images. **Figure 5.14** shows that the microstructures in the alloy matrix of the Cu/IS48/Cu joint coarsen after 168-1008 h of ageing; this result is consistent with the behaviours of bulk alloys, as mentioned in Section 5.3.1. From the Cu maps images, a very small amount of Cu was detected in the alloy matrix of the Cu/IS48 alloy joint, both before and after ageing, which indicates that Cu diffused from the substrate into the alloy matrix during the heating process. On the other hand, **Figures 5.15** and **5.16** show that both Cu/ISC482/Cu and Cu/ISC488/Cu alloy joints exhibit a smaller microstructure and a slight increase in phase size compared to IS/Cu after ageing for 168-1008 h. The (Cu,In,Sn)-IMC size in the solder matrix is almost unchanged after ageing (average grain size of 40 μm^2).
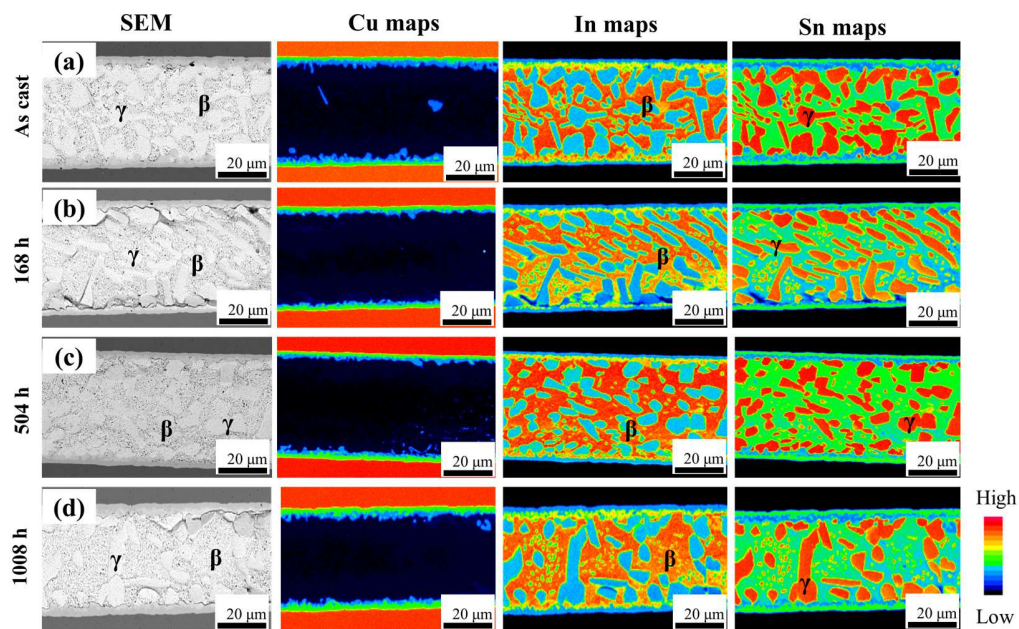
Figure 5.14 Microstructure of Cu/IS48/Cu joint before and after ageing at 60 °C: (a) as-cast (b) 168 h, (c) 504 h, and (d) 1008h.
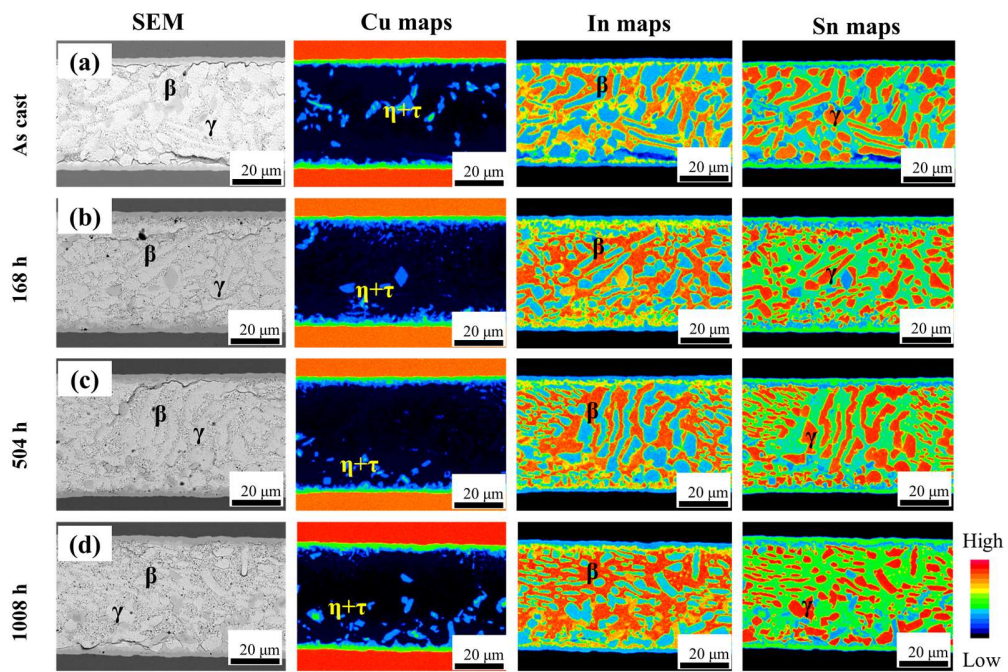
Figure 5.15 Microstructure of Cu/ISC482/Cu joint before and after ageing at 60 °C: (a) as-cast (b) 168 h, (c) 504 h, and (d) 1008h.
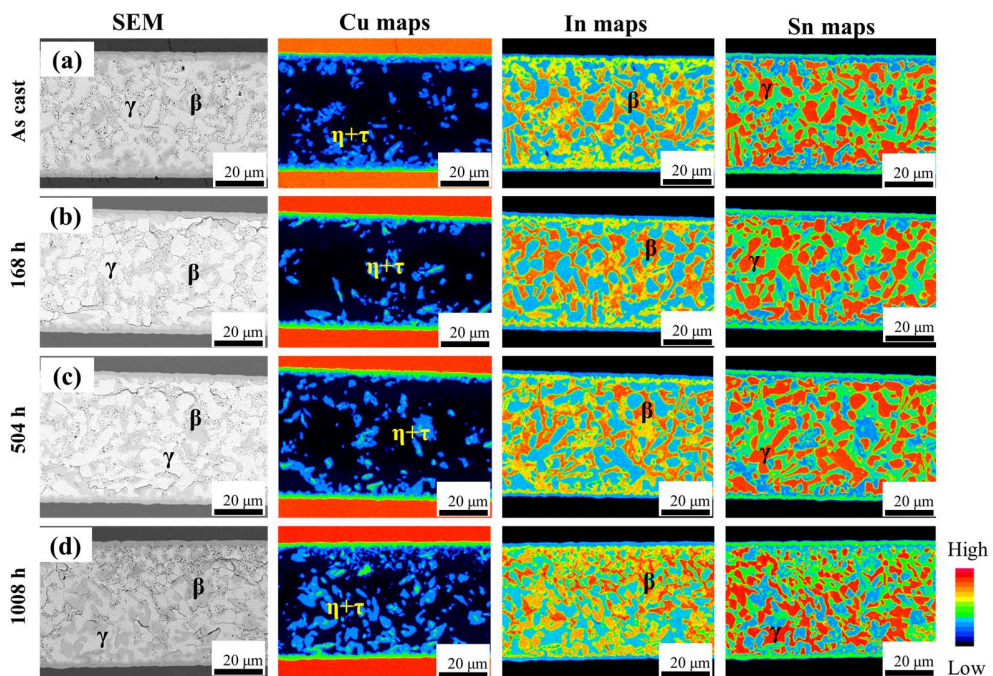
Figure 5.16 Microstructure of Cu/ISC488/Cu joint before and after ageing at 60 °C: (a) as-cast (b) 168 h, (c) 504 h, and (d) 1008h.
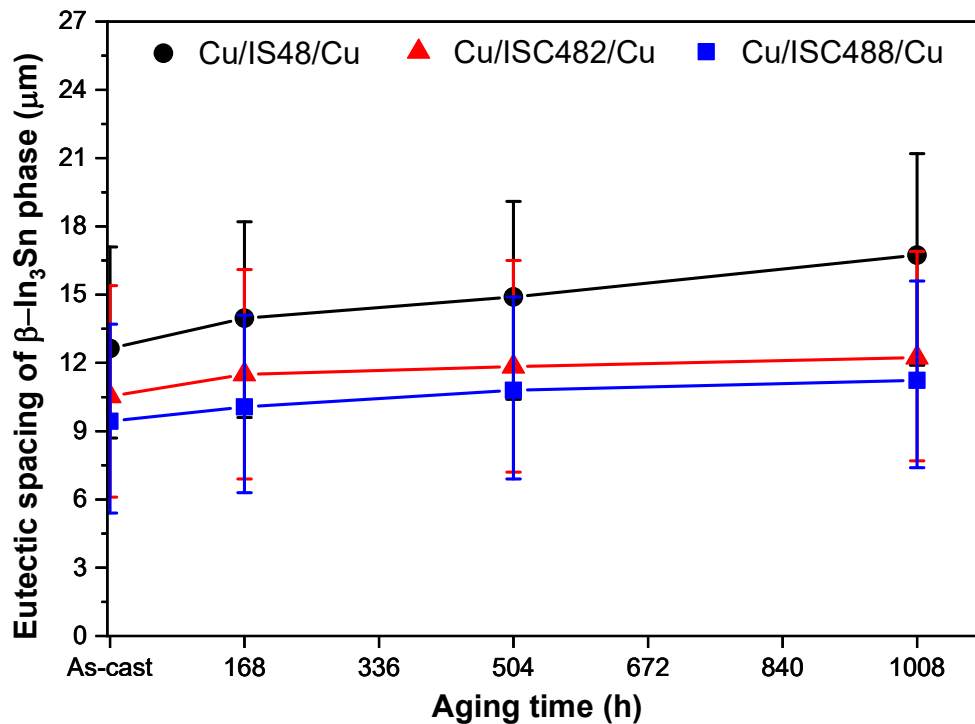
Figure 5.17 Eutectic spacing of β phase of Cu/ISC48/Cu, Cu/ISC482/Cu, and Cu/ISC488/Cu joints before and after ageing.

The eutectic spacing of the β phase was measured by ImageJ software using EPMA In map images, as shown in **Figure 5.17**; the alloy matrix of the Cu/IS48/Cu joint has the largest average eutectic spacing both before and after ageing, compared with values for the Cu/IS482/Cu and Cu/ISC488/Cu joints. These results support the conclusion that the addition of Cu not only refines the microstructure but also prevents phase coarsening after thermal ageing of the IS48 alloy, as previously discussed in Section 5.3.1. A change in the microstructure directly affects the mechanical properties of the alloy joint. The relationship between microstructure evolution after thermal ageing and shear strength is discussed in the next section.

5.4.2 Effect of thermal ageing on IMC growth

In the interfacial reaction between the In52Sn48 alloy and Cu substrates, both In and Sn may react with Cu to form several types of IMC, which makes the Cu/IS48 alloy joints exhibit particular and complicated microstructures [13]. It was explained in Chapter 4 that the interface layer of the Cu/IS48/Cu, Cu/ISC482/Cu, and Cu/ISC488/Cu joints before

ageing consists of $Cu_6(In,Sn)_5$ IMC near the Cu-side and $Cu(In,Sn)_2$ layer near the alloy side. **Figure 5.18** shows the typical EPMA elemental line profile of the Cu/IS48, Cu/ISC482, and Cu/ISC interfaces aged at 60°C for 168 h. This EPMA result confirms the existence of $Cu_6(In,Sn)_5$ and $Cu(In,Sn)_2$ layers. However, it is difficult to distinguish these two IMC layers in the BSE images. Therefore, EPMA Cu map images were used to determine the thickness of the IMC layer, as shown in **Figure 5.19**. The plate-like $Cu_6(In,Sn)_5$ IMC layer (green) next to the Cu substrate and the $Cu(In,Sn)_2$ IMC layer (blue) with irregular morphology on the alloy side, can be clearly seen (**Figure 5.19**). This result is compatible with the results of Kim et al. [14]. The thickness of the IMC layer at the Cu/IS48, Cu/ISC82, and Cu/ISC488 interfaces increases with ageing time. The relationship between the increase in IMC thickness and ageing time was measured by ImageJ software using EPMA Cu map images, as shown in **Figure 5.20**.
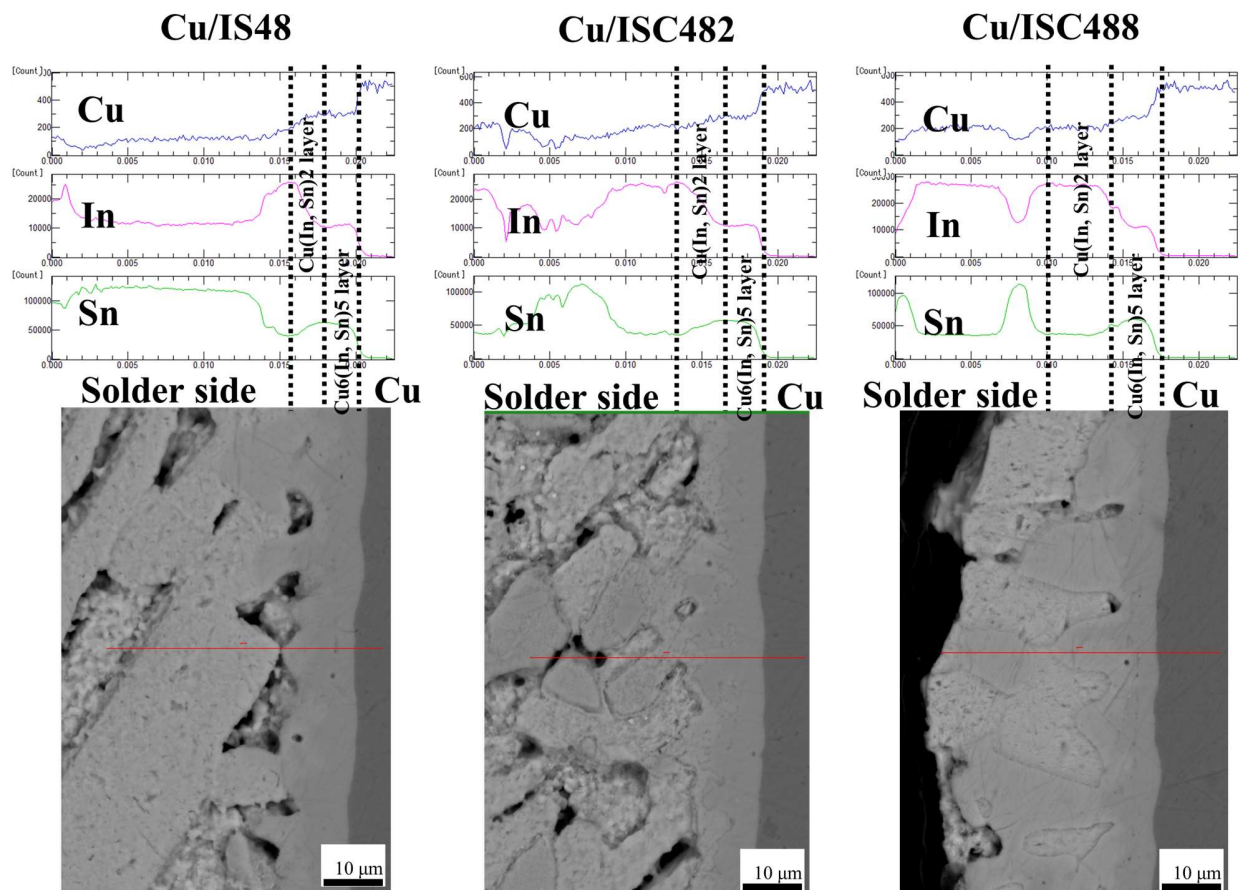
Figure 5.18 Typical EPMA elemental-line profile of the IMC layers of Cu/IS48, Cu/ISC482, and Cu/ISC488 interfaces after 168 h of ageing.
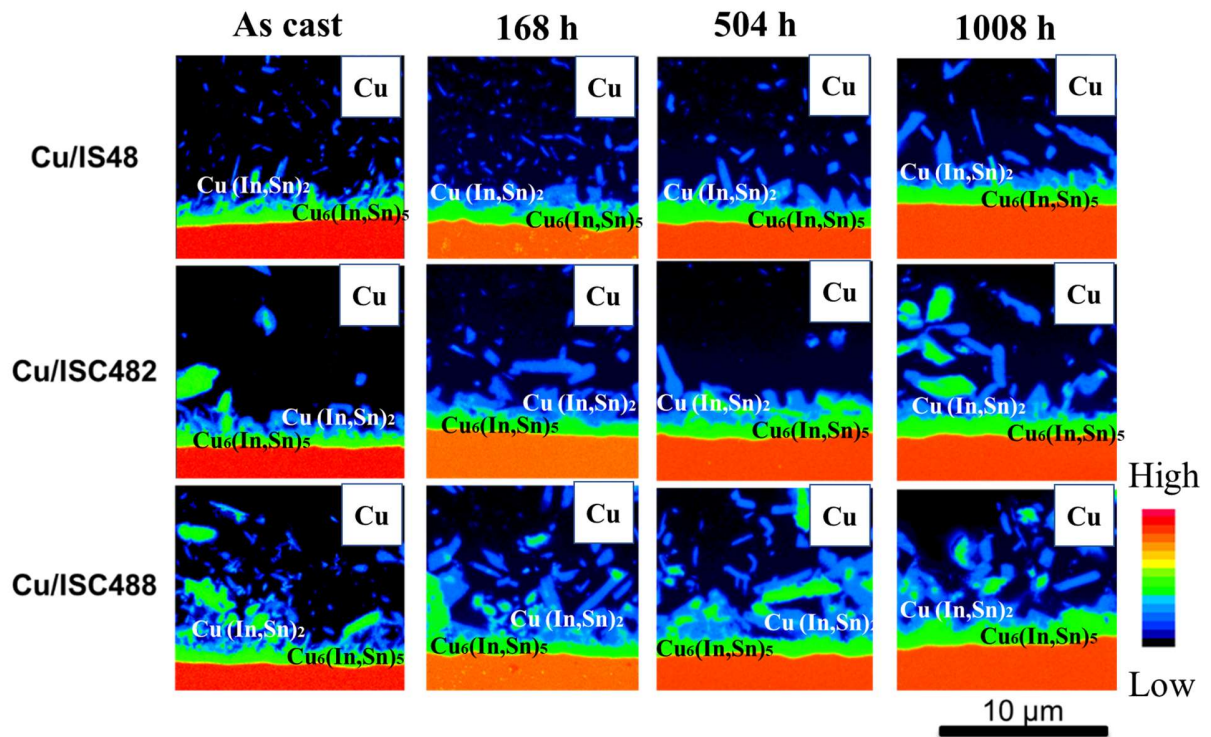
Figure 5.19 EPMA Cu map images of Cu/IS48, Cu/ISC482, and Cu/ISC488 interface before and after ageing.

The thickness of the $Cu_6(In,Sn)_5$ IMC layer and total IMC [$Cu_6(In,Sn)_5 + Cu(In,Sn)_2$] thickness increase linearly with the square root of ageing time, and growth is faster with a longer ageing time. In **Figure 5.20a**, it can be seen that the thickness of the $Cu_6(In,Sn)_5$ IMC layer of the Cu/ISC488 and Cu/ISC482 interfaces (3.6 µm and 3.2 µm) is smaller than that of the Cu/IS48 interface (4.0 µm) before ageing; this is because the addition of Cu prevents Cu atoms from diffusing from the Cu substrate into the alloy matrix during the heating process. After 168-1008 h of ageing, the thickness of the $Cu_6(In,Sn)_5$ IMC layer increased slightly, and after 1008 h of ageing, the thickness of the $Cu_6(In,Sn)_5$ IMC layer of Cu/ISC488 interface exceeds that of the Cu/ISC482, and Cu/IS48 interfaces (5.2 µm, 4.0 µm, and 4.8 µm, respectively). On the other hand, the total IMC thickness of the Cu/ISC488 interface exhibited a significant increase after 168-1008 h of ageing compared with the increase in the Cu/ISC482 and Cu/IS48 interfaces (**Figure 5.20b**). The relationship between IMC thickness at a solder/Cu interface and ageing time can be adequately follows the Equation (2) [15,16]:

$$H = K.t^n, \qquad\qquad\qquad (2)$$

Where H is the thickness of the interfacial IMC, K is the coefficient of IMC growth rate, t is the reaction time, and n is the time exponent. Thus, Equation (2) can be converted into a logarithmic expression:

$$ln(H) = lnK + nln(t), \qquad\qquad\qquad (3)$$

Therefore, $ln(H)$ shows a linear relationship with $ln(t)$. Based on the correlation graph between $ln(H)$ and $ln(t)$, using the linear fitting function of OriginPro software, Equation (3) of the line relating the logarithm of the $Cu_6(In,Sn)_5$ IMC thickness (d), total IMC thickness (H), and the ageing time (t) for each alloy/Cu interface, is shown in **Figure 5.20c-d**. The time exponent was determined and is summarised in **Table 5.4**.
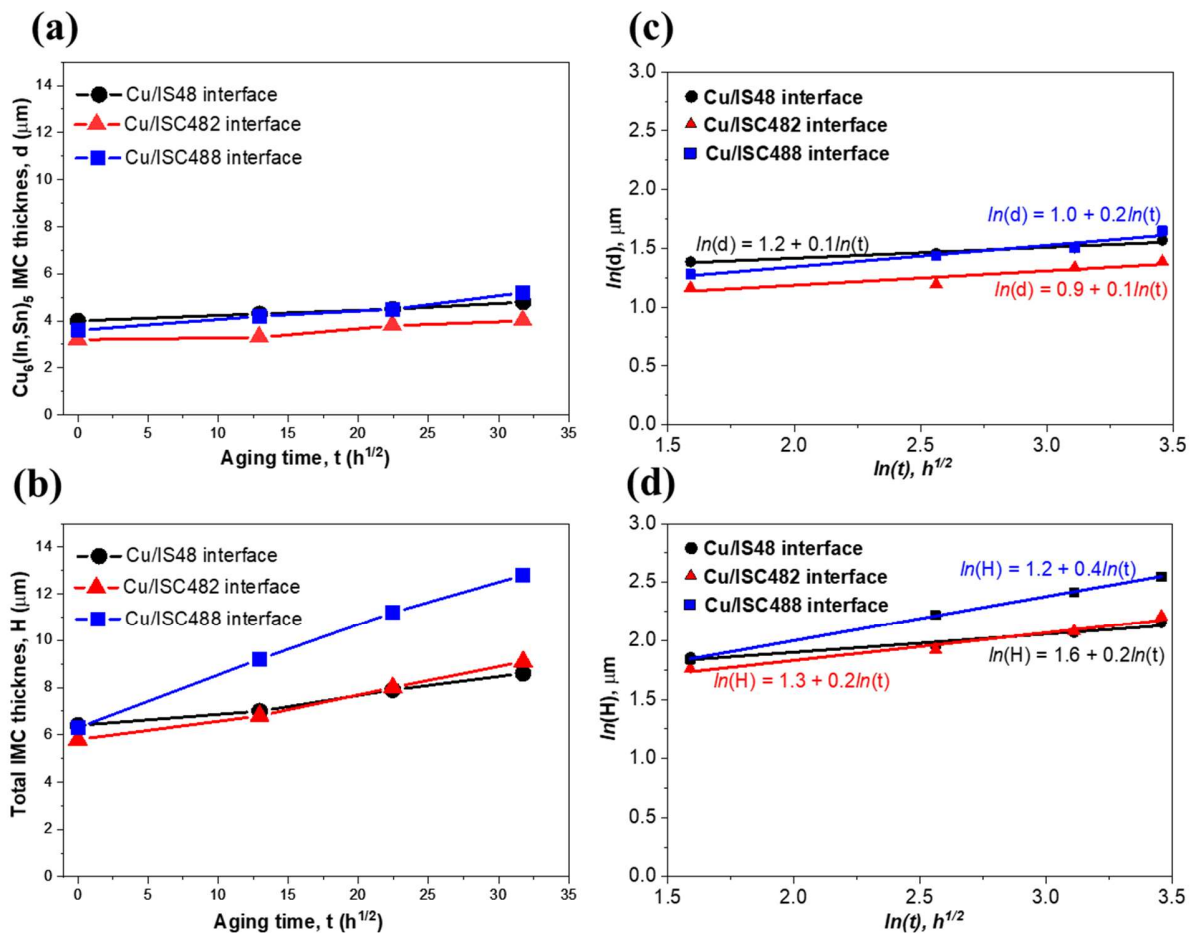
Figure 5.20 (a,c) The thickness of $Cu_6(In,Sn)_5$ IMC layer, and (b,d) total IMC thickness of interfacial layers of alloy joints before and after ageing.

Table 5.4 Time exponents (n) as a function of ageing time.

Alloy/Cu interface	Intermetallic compounds (IMC)	Time exponent (n)
Cu/IS48	$Cu_6(In, Sn)_5$ IMC layer	0.1
	$[Cu_6(In, Sn)_5 + Cu(In, Sn)_2]$ IMCs layer	0.2
Cu/ISC482	$Cu_6(In, Sn)_5$ IMC layer	0.1
	$[Cu_6(In, Sn)_5 + Cu(In, Sn)_2]$ IMCs layer	0.2
Cu/ISC488	$Cu_6(In, Sn)_5$ IMC layer	0.2
	$[Cu_6(In, Sn)_5 + Cu(In, Sn)_2]$ IMCs layer	0.4

Generally, the atomic diffusion of In, Sn, and Cu through the IMC layer is the main controlling process for IMC growth during ageing. The growth of intermetallic compounds in the solid state follows linear or parabolic growth kinetics. When n=1/3, the interfacial IMC growth follows the parabolic law and is grain boundary diffusion-controlled [17]; when n=1/2, interfacial IMC growth follows the parabolic law and is volume diffusion-controlled; when n=1, the interfacial IMC growth follows the linear law and is reaction controlled at the growth site [15,18]. **Figure 5.20c-d** indicates that the time exponents (*n*) after linear fitting were 0.1-0.4. This confirms that the growth of the IMC layers during isothermal ageing is controlled by grain boundary diffusion. Moreover, because the melting point of the IS48 and ISC alloys (~117°C) is much lower than that of the Cu substrate (1084°C), the homologous temperature of the IS48 and ISC alloys during ageing at 60°C (~0.85) is much higher than that of Cu (~0.25). As a result, diffusion is most likely to take place on the alloy side [3]. Therefore, we can see that the $Cu_6(In,Sn)_5$ IMC layer grows very slowly (confirmed by n=0.1-0.2). On the other hand, the total thickness of IMC increases sharply with ageing; in other words, the $Cu(In,Sn)_2$ IMC layer near the alloy side grows very quickly with ageing. The sizes of Sn and In atoms are very similar, and so Sn atoms can easily take substitutional sites of In in $Cu(In,Sn)_2$ IMC ($CuIn_2$ crystal lattices). In the same way, the In atoms also can take substitutional sites of Sn in $Cu_6(In,Sn)_5$ IMC (Cu_6Sn_5

crystal lattices). Since the Cu(In,Sn)$_2$ IMC layer is closer to the alloy side, the In and Sn atoms will diffuse more readily into the crystal lattice of this IMC layer, leading to a significant increase in the thickness of the Cu(In,Sn)$_2$ IMC layer. The diffusion and substitution lead to the growth of the Cu-In-Sn IMCs at the Cu/IS48, Cu/ISC482, and Cu/ISC488 interfaces during isothermal ageing [19].

5.4.3 *Shear strength and fracture surface*

Figure 5.21 shows the average shear strength of alloy joints before and after isothermal ageing at 60°C for 168-1008 h. It can be seen that all the Cu/IS48/Cu, Cu/ISC482/Cu, and Cu/ISC488/Cu joints have reduced average shear strength after 168-1008 h of ageing. However, after 1008 h of ageing, the Cu/ISC482/Cu and Cu/ISC488/Cu joints have higher average shear strength (10.3 MPa and 10.9 MPa, respectively) than the Cu/IS48/Cu joint (9.7 MPa). This result proves that Cu/IS482/Cu and Cu/ISC488/Cu joints have better thermal reliability than a Cu/IS48/Cu joint. The decrease in the shear strength of the alloy joints can be explained by the microstructural coarsening of the alloy matrix during thermal ageing, as discussed in the previous section. **Figure 5.17** indicates that the eutectic spacing of the β phase in the alloy matrix of Cu/IS48/Cu and Cu/ISC482/Cu joints increased by 17% and 14%, respectively, immediately after 168 h of ageing, while that of the matrix Cu/ISC488 joint increased by 7%. This means that the microstructural coarsening rate in the alloy matrix of the Cu/IS48 and Cu/ISC482 joints is faster, leading to a larger decrease in shear strength (about 26-27%) than the decrease for the Cu/ISC488 joint (22%). Furthermore, after 1008 h of ageing, the eutectic spacing of the β phase of the Cu/ISC482/Cu and Cu/ISC488/Cu joints increased slightly (20% and 16%), while that of the Cu/IS48/Cu joint increased significantly (41%). This result explains why the decrease in shear strength of the Cu/IS48/Cu joint (34%) is higher than that of the Cu/ISC488/Cu joint (25%). In addition, the voids generated during the heating process and the IMCs in the alloy matrix also have a significant influence on the shear strength of the alloy joints. **Figure 5.22** shows the top view and cross-sectional SEM images of shear-fractured samples of alloy joints on the bottom disc before and after ageing.

Figure 5.21 Shear strength of Cu/IS48/Cu, Cu/ISC482/Cu, and Cu/ISC488/Cu joints before and after ageing.

The percentage of voids on the fracture surface of the shear test samples after ageing were measured with the same method as described in Section 4.3.3 of Chapter 4 (**Figure 4.13**), and the results are shown in **Figure 5.23**. The highest number of voids appear in the Cu/ISC488 joint (15.8%) and the least in the Cu/IS48 joint (7.5%); this is because ISC488 has a lower wettability than IS48, as mentioned in Chapter 2. Generally, voids in solder joints are the factor that significantly affects joint strength. Moreover, from the cross-sectional images (**Figure 5.22b**), it can be seen that all the Cu/alloy joints are destroyed in the alloy matrix. This proves that the strength of the solder joint is determined mainly by the mechanical properties of the alloy matrix. The (Cu,In,Sn)-IMCs available in the alloy matrix of the Cu/IS482 and Cu/ISC488 joints (red arrow) are apparent in **Figure 5.22b** and the EPMA Cu map shown in **Figure 5.15-5.16**. These IMCs not only contribute to the stabilisation of the microstructure during ageing but also participate in strengthening the alloy matrix. Therefore, the Cu/ISC482 and Cu/ISC488 joints are stronger than the Cu/IS48 joint after ageing, as shown in **Figure 5.21**. The crack morphology through the alloy matrix of the Cu/IS482 joint is serrated because the ISC482 alloy has the greatest elongation both before and after ageing, as discussed in **Figure 5.9b**. The crack morphology of Cu/IS48 and Cu/ISC488 joints is flat, but all the alloys exhibit ductile behaviour under shear force.

This is demonstrated through the results of SEM image analysis at high magnification of the fracture surfaces of the alloy joints, as shown in **Figure 5.24**; it can be seen that many dimples appear on the fracture surface, both before and after ageing. This ductile fracture behaviour is owing to all bulk alloys exhibiting better elongation after isothermal ageing, as shown in **Figure 5.9**.
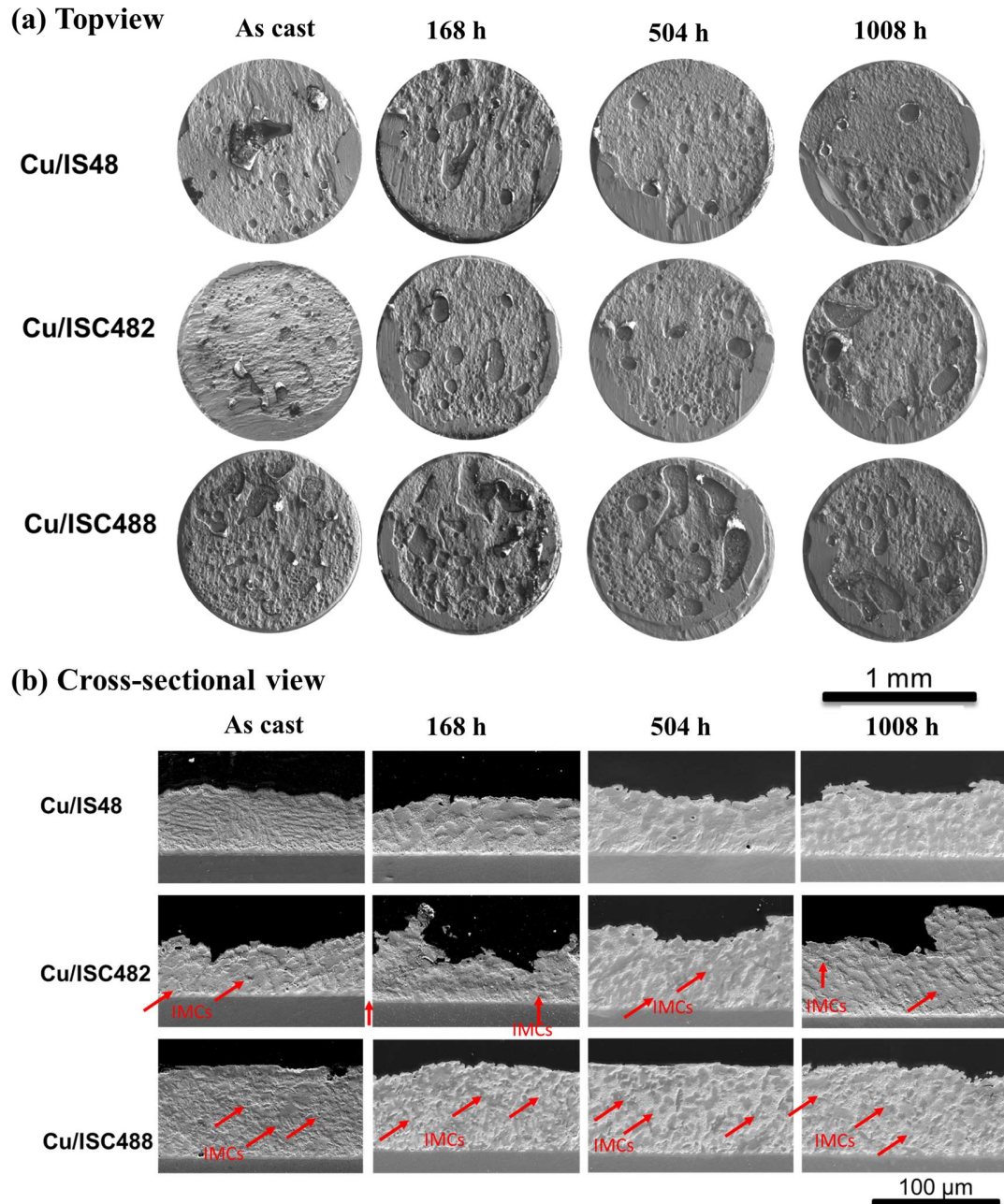
Figure 5.22 (a) Top view, and (b) cross-sectional SEM images of shear fractured samples of alloy joints at the bottom disk before and after ageing.
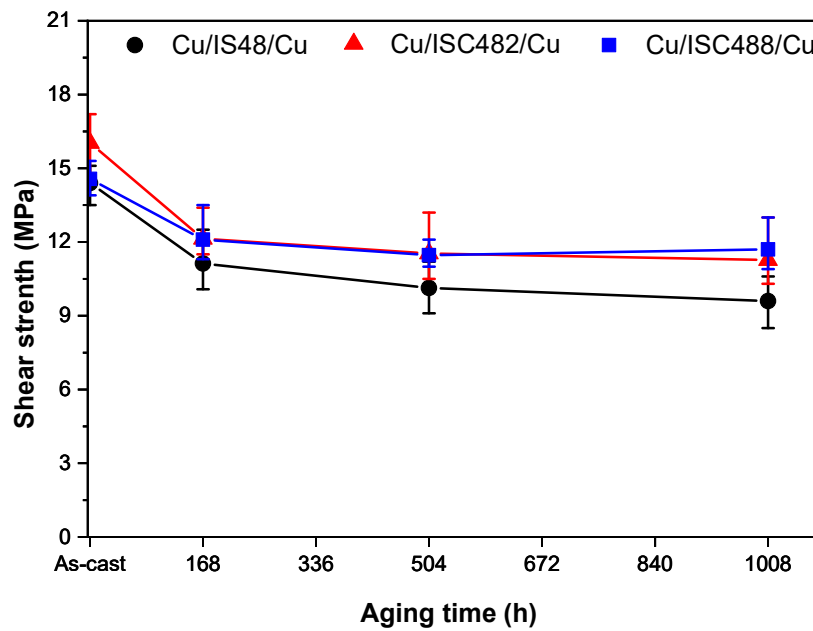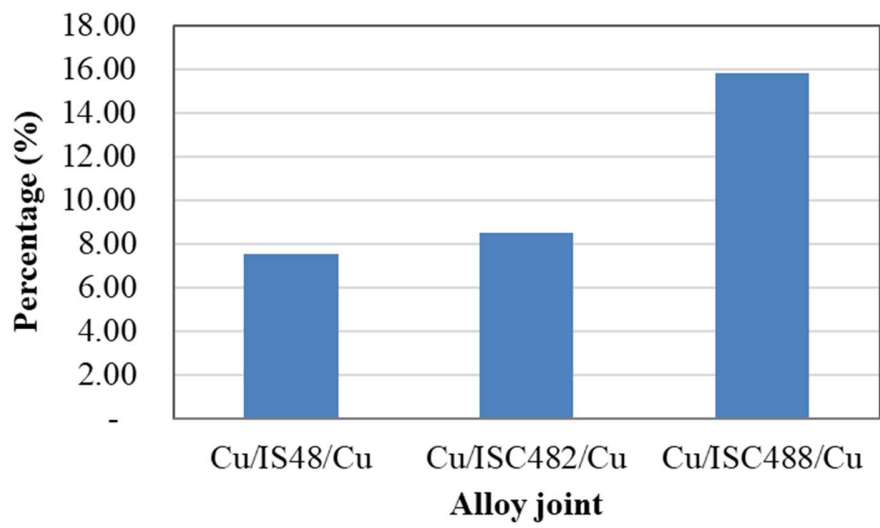
Figure 5.23 The percentage of void on fractured surface of shear test samples after ageing.
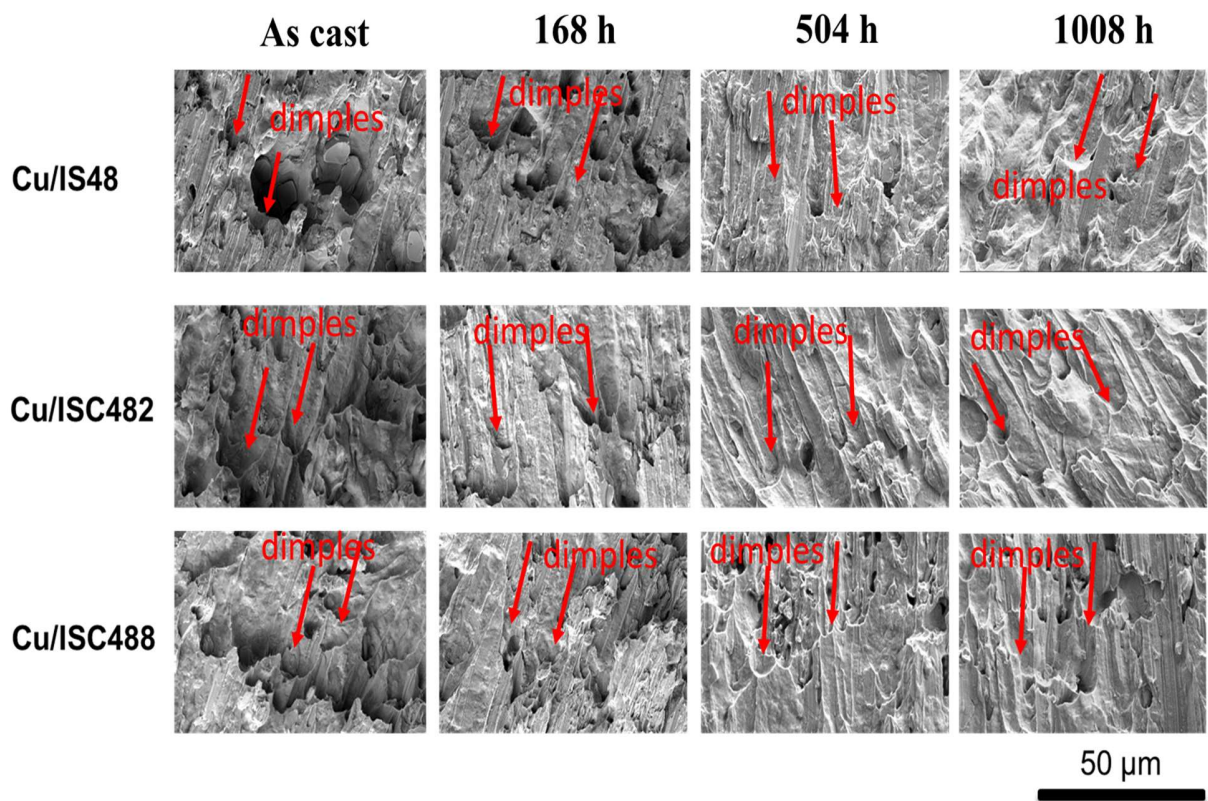
Figure 5.24 Fractured surface of alloy joints before and after ageing.

5.4 Conclusion

In this chapter, the addition of Cu has been shown to affect microstructural coarsening of the IS48 alloy during thermal ageing, thereby improving the strength of both the alloy and the alloy on a Cu substrate with ageing. The conclusions are set out below:

For bulk alloys:

- After isothermal ageing from 168-1008 h, the ISC482 and ISC488 alloys have a stable and finer microstructure than the IS48 alloy. After 1008 h of ageing, the IS48 alloy exhibited the greatest increase in microstructure size; specifically, the average size of the β phase increased by 41%. The ISC482 and ISC488 alloys had a more stable microstructure, with the average size of the β phase increasing slightly by 20% and 16%, respectively.

- The stability of the microstructure combined with the amount of IMC appearing in the alloy matrix improves the mechanical properties of ISC482 and ISC488 after ageing. Specifically, the tensile strength of ISC488 after 1008 h of ageing was 14.5 MPa (13% reduction), which is still higher than that of IS48 before ageing (~11.0 MPa).

- On the other hand, the change in microstructure leads to a change in the β/γ ratio. After ageing, the β/γ ratio in all alloys increases, leading to an increase in elongation of the alloys. Specifically, the ISC482 alloy has the largest β/γ ratio (1.6-1.8), leading to it having the greatest elongation (~70%) after 1008 h of ageing. The value is lower for the IS48 and ISC488 alloys (β/γ = 1.2-1.4), with elongation of approximately 44%. As a result, both alloys exhibit ductile fracture behaviour in the tensile test.

For alloy joints:

- After ageing, the alloy matrix of the Cu/IS48/Cu joint exhibits faster microstructural coarsening than the matrix of the Cu/ISC482/Cu and Cu/ISC488/Cu joints. After 1008 h of ageing, the eutectic spacing of the β phase in the alloy matrix of the Cu/IS48/Cu joint increased significantly (41%) compared to the Cu/ISC482/Cu and

Cu/ISC488/Cu joints (20% and 16%, respectively). The result leads to a greater decrease in the average shear strength of the Cu/IS48/Cu joint (34%) compared to the Cu/ISC488/Cu joint (25%).

- The interfacial layer of Cu/alloys includes the plate-like $Cu_6(In,Sn)_5$ IMC layer next to the Cu substrate and the $Cu(In,Sn)_2$ IMC layer with irregular morphology on the solder side. The thickness of the $Cu_6(In,Sn)_5$ IMC layer and total IMC [$Cu_6(In,Sn)_5$ + $Cu(In,Sn)_2$] thickness increases linearly with the square root of ageing time, and growth is faster with a longer ageing time. The time exponent n=0.1-0.4 confirms that the interfacial IMC layer growth during isothermal ageing follows the parabolic law, and is grain boundary diffusion-controlled. Here, the $Cu_6(In,Sn)_5$ IMC layer grows more slowly than the $Cu(In,Sn)_2$ IMC layer under isothermal ageing at 60°C for 168-1008 h.

- All the alloy joints are destroyed in the alloy matrix, which proves that the strength of the solder joint is determined mainly by the mechanical properties of the solder matrix. The (Cu,In,Sn) IMCs in the solder matrix not only contribute to the stabilisation of the microstructure during ageing but also participate in strengthening the alloy matrix. Therefore, the Cu/ISC482 and Cu/ISC488 joints are stronger than the Cu/IS48 joint after ageing.

Reference

1. Evans, J.W. *A Guide to Lead-free Solders - Physical Metallurgy and Reliability*; Engelmaier, W., Ed.; Springer London, 2007; ISBN 9781846283093.

2. Seyyedi, J. Thermal Fatigue Behaviour of Low Melting Point Solder Joints. *Solder. Surf. Mt. Technol.* **1993**, *5*, 26–32, doi:10.1108/eb037812.

3. Li, Y.; Lim, A.B.Y.; Luo, K.; Chen, Z.; Wu, F.; Chan, Y.C. Phase segregation, interfacial intermetallic growth and electromigration-induced failure in Cu/In-48Sn/Cu solder interconnects under current stressing. *J. Alloys Compd.* 2016, *673*, 372–382.

4. Ding, Y.; Wang, C.; Tian, Y.; Li, M. Influence of aging treatment on deformation behavior of 96.5Sn3.5Ag lead-free solder alloy during in situ tensile tests. *J. Alloys Compd.* **2007**, *428*, 274–285, doi:10.1016/j.jallcom.2006.02.069.

5. Shu, Y.; Ando, T.; Yin, Q.; Zhou, G.; Gu, Z. Phase diagram and structural evolution of tin/indium (Sn/In) nanosolder particles: From a non-equilibrium state to an equilibrium state. *Nanoscale* **2017**, *9*, 12398–12408, doi:10.1039/c7nr01402c.

6. Goldstein, J.L.F.; Morris, J.W. The Effect of Substrate on the Microstructure and Mechanical Behavior of Eutectic Indium-Tin. *MRS Proc.* **1994**, *323*, doi:10.1557/proc-323-159.

7. Le Han, D.; Shen, Y.A.; Jin, S.; Nishikawa, H. Microstructure and mechanical properties of the In–48Sn–xAg low-temperature alloy. *J. Mater. Sci.* **2020**, *55*, 10824–10832, doi:10.1007/s10853-020-04691-7.

8. Zhou, S.; Mokhtari, O.; Rafique, M.G.; Shunmugasamy, V.C.; Mansoor, B.; Nishikawa, H. Improvement in the mechanical properties of eutectic Sn58Bi alloy by 0.5 and 1 wt% Zn addition before and after thermal aging. *J. Alloys Compd.* **2018**, *765*, 1243–1252, doi:10.1016/j.jallcom.2018.06.121.

9. Sayyadi, R.; Naffakh-m, H. The Role of Intermetallic Compounds in Controlling the Microstructural , Physical and Mechanical Properties of Cu- [Sn- Ag-Cu-Bi] -Cu Solder Joints. **2019**, *3*, 1–20, doi:10.1038/s41598-019-44758-3.

10. Ye, D.; Du, C.; Wu, M.; Lai, Z. Microstructure and mechanical properties of Sn–xBi solder alloy. *J. Mater. Sci. Mater. Electron.* **2015**, *26*, 3629–3637, doi:10.1007/s10854-015-2880-z.

11. Zhou, S.; Yang, C. han; Lin, S. kang; AlHazaa, A.N.; Mokhtari, O.; Liu, X.; Nishikawa, H. Effects of Ti addition on the microstructure, mechanical properties and electrical resistivity of eutectic Sn58Bi alloy. *Mater. Sci. Eng. A* **2019**, *744*, 560–569, doi:10.1016/j.msea.2018.12.012.

12. Jiang, N.; Zhang, L.; Gao, L.-L.; Song, X.-G.; He, P. Recent advances on SnBi low-temperature solder for electronic interconnections. *J. Mater. Sci. Mater. Electron.* **2021**, *32*, 22731–22759, doi:10.1007/s10854-021-06820-7.

13. Ramos De Debiaggi, S.; Deluque Toro, C.; Cabeza, G.F.; Fernández Guillermet, A. Ab initio comparative study of the Cu-In and Cu-Sn intermetallic phases in Cu-In-Sn alloys. *J. Alloys Compd.* **2012**, *542*, 280–292, doi:10.1016/j.jallcom.2012.06.138.

14. Kim, D.-G.; Jung, S.-B. Interfacial reactions and growth kinetics for intermetallic compound layer between In–48Sn solder and bare Cu substrate. *J. Alloys Compd.* **2005**, *386*, 151–156.

15. Zhao, N.; Zhong, Y.; Huang, M.L.; Ma, H.T.; Dong, W. Growth kinetics of Cu6 Sn5 intermetallic compound at liquid-solid interfaces in Cu/Sn/Cu interconnects under temperature gradient. *Sci. Rep.* **2015**, *5*, 1–12, doi:10.1038/srep13491.

16. Jeong, G.; Yu, D.-Y.; Baek, S.; Kim, J.; Ko, Y.-H. Interfacial Reactions and Mechanical Properties of Sn–58Bi Solder Joints with Ag Nanoparticles Prepared Using Ultra-Fast Laser Bonding.

Materials (Basel). **2021**, *14*, 1–16, doi:https://doi.org/10.3390/ma14020335.

17. Gusak, A.M.; Tu, K.N. Kinetic theory of flux-driven ripening. *Phys. Rev. B - Condens. Matter Mater. Phys.* **2002**, *66*, 1154031–11540314, doi:10.1103/physrevb.66.115403.

18. Kim, D.; Yoon, J.; Lee, C.; Jung, S. Reaction Diffusion and Formation of Cu11In9 and In27Ni10 Phases in the Couple of Indium-Substrates. **2003**, *44*, 72–77.

19. Shang, P.J.; Liu, Z.Q.; Li, D.X.; Shang, J.K. Phase identification of intermetallic compounds formed during in-48Sn/Cu soldering reactions. *2009 Int. Conf. Electron. Packag. Technol. High Density Packag. ICEPT-HDP 2009* **2009**, *3*, 597–600, doi:10.1109/ICEPT.2009.5270680.

Chapter 6

Conclusions and future work

6.1 Summary

In this research, the author developed several new solder alloys by alloying 0.5-1.5 wt.% of Ag and 1.0-8.0 wt.% of Cu into a eutectic In52Sn48 alloy. The motivation was to overcome issues with the eutectic In52Sn48 alloy, including microstructural coarsening and low tensile strength. The author studied the microstructure and mechanical properties of In52Sn48 (IS48), In52Sn48-0.5Ag (ISA4805), In52Sn48-1.0Ag (ISA4810), In52Sn48-1.5Ag (ISA4815), In52Sn48-1.0Cu (ISC481), In52Sn48-2.0Cu (ISC482), In52Sn48-8.0Cu (ISC488) alloys; the effect of the addition of Cu on the microstructure and mechanical properties of the eutectic IS48, ISC482, and ISC488 alloys during isothermal aging; and the shear properties, microstructure evolution, interfacial reaction, and fracture surface of Cu/IS48/Cu, Cu/ISC482/Cu, Cu/ISC488/Cu joints before and after thermal aging. The main findings and conclusions in each chapter as follows:

Chapter 1 described the inevitable trend of flexible electronics, as well as the problems faced by soldering technology and solder materials when joining electronic components on plastic materials with low melting point temperature. Briefs on lead-free solder and low-temperature solder are also included, thereby highlighting the weaknesses of low-temperature solders and the motivation to improve them.

Chapter 2 investigated the effect of 0.5-1.5 wt. % Ag addition on the melting temperature, microstructure, and mechanical properties of IS48 eutectic alloy. Due to the ternary eutectic reaction, the fusion start temperature of all the ISA alloys is around 113°C, which is lower than that of the eutectic In52Sn48 alloy (117°C). The ε-AgIn$_2$ forms in the β-In$_3$Sn phases and near β-In$_3$Sn/γ-InSn$_4$ boundaries in the ISA alloys following the addition of Ag, which reduces the average area of both β-In$_3$Sn phases and γ-InSn$_4$ phases; these smaller phases enhance tensile strength and alter the fractured mode. ISA4815, with the smallest phases, is the strongest of the alloys, with a tensile strength of 12.5 MPa; this alloy fractures in transgranular mode, as commonly seen in crystals with small grains. In addition, all the ISA alloys exhibit better elongation than the eutectic In52Sn48 alloy, which is attributable to smaller hard γ-InSn$_4$ regions. Among the alloys, ISA4805, with the highest

soft-β-In$_3$Sn/hard-γ-InSn$_4$ ratio and devoid of very small phase sizes, is the softest, with an elongation of 64%.

Chapter 3 demonstrated the effects of various Cu concentrations (1.0 wt. %, 2.0 wt. %, and 8.0 wt. %) on the melting behaviour, microstructure, tensile strength, and elongation of the eutectic In52Sn48 alloy. Owing to the ternary eutectic reaction, the initial fusion temperatures of the ISC alloys are all approximately 115ºC, which is close to that of the eutectic In52Sn48 alloy. The ISC481 alloy with the highest dominant β-In$_3$Sn phase fraction and comparatively smaller IMC fraction displays the greatest elongation and lowest tensile strength, while the ISC488 alloy with the largest total amount of the η-Cu$_6$(In,Sn)$_5$ + τ- Cu(In,Sn)$_2$ IMC phases exhibits enhancement of mechanical properties with a tensile strength of approximately 17.0 MPa. All the ISC alloys fracture in transgranular mode, as is commonly observed in ductile materials. These results confirm that the addition of Cu has a significant effect on the microstructure, tensile strength, and elongation of the eutectic In52Sn48 alloy.

Chapter 4 studied the effect of Cu addition on the wettability, microstructure evolution, interfacial reactions, and shear strength of the In–Sn–xCu/Cu joints (x = 2.0 and 8.0 wt. %). The addition of Cu increases the contact angle of the In-Sn-xCu alloys on the Cu substrate because of the higher viscosity of liquid Cu than In and Sn. However, both the ISC alloys exhibit acceptable wettability, as indicated by the formation of a continuous Cu$_6$(In,Sn)$_5$ + Cu$_($In,Sn)$_2$ IMC layer at the In-Sn-xCu/Cu interface. The In-Sn-2.0Cu/Cu joint exhibits a fine microstructure with small numbers of voids and (Cu,In,Sn)-IMC in the alloy matrix. It also has the smoothest and thinnest IMC layer at the interface; this enhances the shear strength of the alloy joint (16.5 MPa) when compared to the In-Sn/Cu joint (14.5 MPa). Conversely, the In-Sn-8.0Cu/Cu joint has the highest number of voids in the alloy matrix and has a thick and rough IMC layer at the interface, which reduces the shear strength of the alloy joint (14.3 MPa).

Chapter 5 evaluated the change of the microstructures and mechanical properties after isothermal aging test on IS48, ISC482, and ISC488 bulk alloys and their joints on a Cu substrate. The results indicated that:

For bulk alloys:

After isothermal ageing from 168-1008 h, the ISC482 and ISC488 alloys have a stable and finer microstructure than the IS48 alloy. After 1008 h of ageing, the IS48 alloy exhibited the greatest increase in microstructure size; specifically, the average size of the β phase increased by 41%. The ISC482 and ISC488 alloys had a more stable microstructure, with the average size of the β phase increasing slightly by 20% and 16%, respectively. The stability of the microstructure combined with the amount of IMC appearing in the alloy matrix improves the mechanical properties of ISC482 and ISC488 after ageing. Specifically, the tensile strength of ISC488 after 1008 h of ageing was 14.5 MPa (13% reduction), which is still higher than that of IS48 before ageing (~11.0 MPa). On the other hand, the change in microstructure leads to a change in the β/γ ratio. After ageing, the β/γ ratio in all alloys increases, leading to an increase in elongation of the alloys. Specifically, the ISC482 alloy has the largest β/γ ratio (1.6-1.8), leading to it having the greatest elongation (~70%) after 1008 h of ageing. The value is lower for the IS48 and ISC488 alloys (β/γ = 1.2-1.4), with elongation of approximately 44%. As a result, both alloys exhibit ductile fracture behaviour in the tensile test.

For alloy joints:

After ageing, the alloy matrix of the Cu/IS48/Cu joint exhibits faster microstructural coarsening than the matrix of the Cu/ISC482/Cu and Cu/ISC488/Cu joints. After 1008 h of ageing, the eutectic spacing of the β phase in the alloy matrix of the Cu/IS48/Cu joint increased significantly (41%) compared to the Cu/ISC482/Cu and Cu/ISC488/Cu joints (20% and 16%, respectively). The result leads to a greater decrease in the average shear strength of the Cu/IS48/Cu joint (34%) compared to the Cu/ISC488/Cu joint (25%). The interfacial layer of Cu/alloys includes the plate-like $Cu_6(In,Sn)_5$ IMC layer next to the Cu substrate and the $Cu(In,Sn)_2$ IMC layer with irregular morphology on the solder side. The thickness of the $Cu_6(In,Sn)_5$ IMC layer and total IMC [$Cu_6(In,Sn)_5 + Cu(In,Sn)_2$] thickness increases linearly with the square root of ageing time, and growth is faster with a longer ageing time. The time exponent n=0.1-0.4 confirms that the interfacial IMC layer growth during isothermal ageing follows the parabolic law, and is grain boundary diffusion-

controlled. Here, the $Cu_6(In,Sn)_5$ IMC layer grows more slowly than the $Cu(In,Sn)_2$ IMC layer under isothermal ageing at 60°C for 168-1008 h. All the alloy joints are destroyed in the alloy matrix, which proves that the strength of the solder joint is determined mainly by the mechanical properties of the solder matrix. The (Cu,In,Sn) IMCs in the solder matrix not only contribute to the stabilisation of the microstructure during ageing but also participate in strengthening the alloy matrix. Therefore, the Cu/ISC482 and Cu/ISC488 joints are stronger than the Cu/IS48 joint after ageing.

The initial goal of the research was to overcome the weaknesses of alloy IS48. The results show that the addition of Ag (0.5-1.5 wt.%) had a greater effect on reducing the melting temperature of IS48 than the addition of Cu (1.0-8.0 wt.%). However, both Ag and Cu help maintain the low temperature range of the In52Sn48 alloy, which is an advantage that makes this alloy suitable in coupling applications for flexible devices using low melting temperature substrate materials. In addition, All developed alloys have better elongation than In60Bi40 alloy, and ISC488 alloy has a higher tensile strength (17 MPa) than that of In60Bi40 alloy. Specifically, a small addition of 0.5-1.0 wt.% Ag and 1.0-2.0 wt.% Cu can increase the elongation of the In52Sn48 alloy; Cu has a greater effect than Ag. With 1.0 wt.% Ag added to the IS48 alloy, In is consumed to form $AgIn_2$ IMC, thereby reducing the ratio of the In-rich phase of ISA4810 alloy ($\beta/\gamma = 1.59$). With 1.0 wt.% Cu added to the IS48 alloy, both Sn and In are consumed to form Cu6(In,Sn)5 IMC, and so the ratio of the In-rich phase in alloy ISC481 ($\beta/\gamma = 1.7$) is larger than that in alloy ISA4810. As a result, the ISC481 alloy has greater average elongation (74%) than the ISA4810 alloy (52%). The addition of 1.5 wt.% Ag and 2.0 wt.% and 8.0 wt.% Cu increases tensile strength and elongation, while ISC488 with the addition of 8 wt.% Cu exhibits significantly increased tensile strength compared to the IS48 alloy. The isothermal aging test demonstrates that the addition of 2.0 and 8.0 wt.% Cu helps to refine the microstructure and minimize phase coarsening of the IS48 alloy under the influence of temperature. As a result, the new ISC482 and ISC488 alloys are good candidates to replace IS48 in applications such as flexible electronics, where low-temperature solder is required.

6.2 Life-cycle impact assessment on various solder alloys

Life-cycle impact assessment (LCIA) was used to evaluate the environmental impact of each of five major life-cycle stages: raw materials extraction/acquisition, materials processing, product manufacture, product use, and final disposal/end-of-life [1‑3]. **Figure 6.1** briefly describes each of these stages for a solder product system, and 16 impact categories, and a description of how each is calculated is presented in **Table 6.1** [4]. Lead-free solders are expected to have a reduced toxic impact on the environment [4]. However, energy consumption and other related effects, such as global warming due to emissions generated during manufacturing [1], need to be taken into account.

Inputs	Life-cycle stages	Outputs
	Raw materials extraction/ acquisition (upstream) Activities related to the acquisition of natural resources, including mining non-renewable material, harvesting biomass, and transporting raw materials to processing facilities.	
Materials →	**Materials processing** (Upstream) Processing natural resource by reaction, separation, purification, and alteration steps in preparation for the manufacturing stage; and transporting processed materials to product manufacturing facilities.	→ Wastes
Energy →	**Product manufacture** Processing materials into solder and solder alternatives	
Resources →	**Product use** (use/ application) Application of solders onto printed wiring boards, which are then incorporated into various electronics products.	→ Products
	Final disposition (end-of-life) At the end of their useful lives, the solders, which are part of another product that is produced in the use stage, are retired. If reuse and recycle of the solder is feasible, the product can be transported to an appropriate facility and disassembled or de-manufactured for materials recovery. Materials that are not recoverable are then transported to appropriate facilities and treated and/ or disposed of.	

Figure 6.1 Life-cycle stages for solder alternatives [4].

Table 6.1 Impact Categories [4].

Impact category	Inventory type		Description
	Input	**Output**	
NATURAL RESOURCE IMPACTS			
Non-renewable resource use/depletion	Material, fuel	-	Materials, such as metals or fossil fuels that are not regenerated naturally.
Renewable resource use	Materials, water	-	Materials found in nature that are replenished through natural processes.
Energy use	Electric, fuel	-	The amount of energy consumed. The impacts associated with energy are included under other impact categories.
Landfill space use	-	Solid/hazardous/radioactive waste to landfill	The volume of landfill space required for solid/hazardous/radioactive waste.
ABIOTIC ENOSYSTEM IMPACTS			
Global warming	-	Air	The mass of greenhouse gases emitted (chemical amounts are weighted according to their potency relative to carbon dioxide).
Stratospheric ozone depletion	-	Air	The mass of ozone depleting chemicals emitted (chemical amounts are weighted according to their potency relative to CFC-11).
Photochemical smog	-	Air	The mass of smog-producing chemicals emitted (chemical amounts are weighted according to their potency relative to ethane).
Acidification	-	Air	The mass of acidifying chemicals emitted (chemical amounts are weighted according to their potency relative to sulfur dioxide).
Air particulates	-	Air	The mas of particulates emitted that have an aerodynamic diameter less than 10 micrometers. Note: also use TSP/dust only when PM_{10}[a] is not available.
Water eutrophication (nutrient enrichment)	-	Water	The mass of eutrophication chemicals released (chemical amounts are weighted according to their potency relative to phosphate).
HUMAN HEALTH AND ECOTOXICITY			
Chronic, non-carcinogenic human health effects-occupational	Material	-	Weighted score based on the amount and toxicity of non-carcinogenic releases affecting workers.
Carcinogenic human health effects-occupational	Material	-	
Carcinogenic non-carcinogenic human health effects-public (and terrestrial ecotoxicity)	-	-	Weighted score based on the amount and toxicity of carcinogenic releases affecting the general public.
Carcinogenic human health effects-public	-	Air, soil, water	
Aquatic ecotoxicity	-	Water	Weighted score based on the amount and toxicity of releases affecting fish.
[a] Acronyms: particulate matter with average aerodynamic diameter less than 10 micrometers (PM_{10}); total suspended particulates (TPS); biological oxygen demand (BOD); total suspended solids (TSS).			

On this basis, the low-temperature In52Sn48-based solder alloys are considered environmentally friendly given the associated energy savings in mass production. Compared to conventional solders, such as SnPb, Sn-Ag-Cu (SAC), Bi-Sn-Ag (BSA), In52Sn48 (IS48) with its lower melting temperature exhibits the lowest power consumption during the reflow process. Based on the results of the report in [4], the energy usage of SnPb, SAC and SnBi alloys is 23.3 kW, 25.2 kW, and 15.7 kW, respectively [4]. The relationship between energy consumption (E) and the melting temperature (t) of the solder alloy was analysed using the line fitting function of OriginPro software, as shown in **Figure 6.2**. The estimated energy consumption for the IS48 alloy is 13.7 kW, which is 41.0% and 45% energy saving compared to SnPb and SAC alloys, respectively. Through the reduction in energy consumption, the trend to use low melting point solder materials, the average reduction of CO_2 emission, and the cost savings when using In52Sn48-based alloys compared to commercial SAC solder are shown in **Figure 6.3**. Calculations are conducted according to a report by the Tamura Corporation [5], where the average reduction in electricity consumption is based on 300 working days per year and 18 working hours per day. Calculation of the average reduction in CO_2 emissions is based on the average emission coefficient of 0.401 kg-CO2/kWh [6]. The annual saving is calculated according to the electricity price of 17 yen/kWh [7].
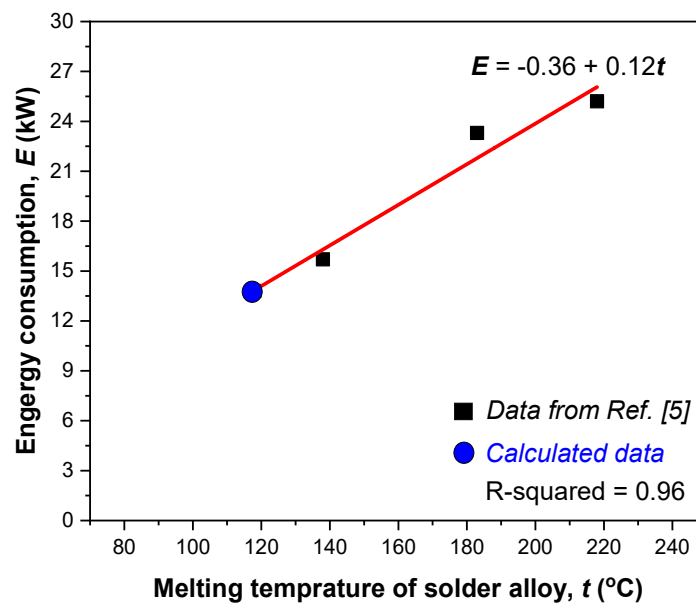

Figure 6.2 The relationship between energy consumption and melting temperature of solder alloy.
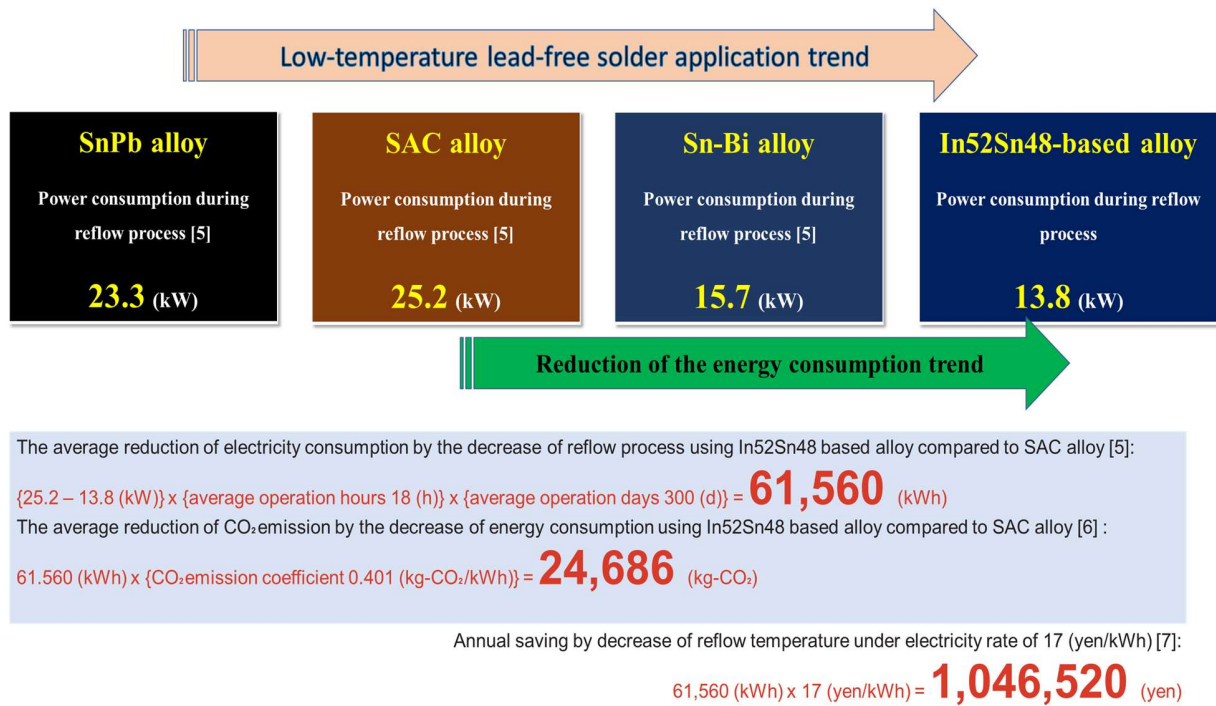
Figure 6.3 Calculating the average reduction of CO_2 emission and the annual saving by decrease of reflow temperature by using In52Sn-based alloy [5–7].

6.3 Future work

The work in this thesis can be further enhanced and extended by the following investigations:

1. Experiments with actual PET/PEN flexible substrate to evaluate joint reliability.
2. A small amount of Ag can enhance the elongation and reduced melting temperature of IS48, and a larger amount of Cu can enhance tensile strength. Further study could focus on the effect of combining a small amount of Ag (ex. 0.1-0.5 wt.%) with a larger amount of Cu (ex. 3.0-7.0 wt.%) on the properties of the IS48 alloy.
3. The addition of 2.0-8.0 wt.% Cu has a significant effect on the properties of the IS48 alloy. However, joint strength was affected by void formation. Therefore, further studies of the mechanism for void formation and the optimising reflow process to reduce the voids in solder would be valuable.

Reference

1. Itsubo, N.; Noh, J.; Inaba, A. Life cycle impact assessment of lead-free solder considering the differences of waste stages. *Electron. Goes Green 2004* **2004**, *45*, 439–443.

2. Boyd, S.B. *Life-cycle assessment of semiconductors*; **2012**; Vol. 9781441999887; ISBN 9781441999887.

3. Schileo, G.; Grancini, G. Lead or no lead? Availability, toxicity, sustainability and environmental impact of lead-free perovskite solar cells. *J. Mater. Chem. C* **2020**, *9*, 67–76, doi:10.1039/d0tc04552g.

4. (EPA), U.S.E.P.A. *Solder in electronics: a life-cycle assessment summary*; **2005**;

5. TamuraCorporation *Environmental report*; **2006**;

6. Administration, U.S.E.I. *U . S . Energy-Related Carbon Dioxide Emissions*; **2019**;

7. Energy, I.M. of E.T. and; And, A. for N.R. *Japan's energy*; **2020**;

Research achievements

I. Paper related doctoral thesis

1. **Microstructure and mechanical properties of the In– 48Sn–xAg low-temperature alloy (published).**
   Journal of Material Science (2020) 55:10824–10832
   <u>Duy Le Han</u>[*], Yu-An Shen, Sanghun Jin, Hiroshi Nishikawa

2. **Effect of Cu addition on the microstructure and mechanical properties of In–Sn-based low-temperature alloy (published).**
   Materials Science & Engineering A 804 (2021) 140785
   <u>Duy Le Han</u>[*], Yu-An Shen, Siliang He, Hiroshi Nishikawa

3. **Microstructure evolution and shear strength of tin-indium-xCu/Cu joints (published)**
   Metals 2022, 12(1), 33
   <u>Duy Le Han</u>, Yu-An Shen, Fupeng Huo, Hiroshi Nishikawa**

II. Conference

1. **Effect of 4.0 mass % Cu addition on microstructure and mechanical properties of In-48Sn alloy (published).**
   International Conference on Electronics Packaging (ICEP 2021)
   <u>Duy Le Han</u>, Byungho Park, Hiroshi Nishikawa

Acknowledgements

First of all, I would like to thank my supervisor Professor Hiroshi Nishikawa for giving me the opportunity to do research, and his valuable suggestions, guidance throughout my doctoral study course. His dynamism, vision, kindness, and motivation have deeply inspired me. It was a great privilege and honor to work and study under his guidance.

Besides my adviser, I thank the rest of my thesis committee: Professor Fukumoto Shinji and Associate Professor Iwata Yoshiharu for their insightful comments and helpful discussion for this dissertation.

In addition, I thank the technical support from Mr. Kenji Asano, Mr. Yoshiro Abe, Mr. Takeshi Murakami, Mr. Takuya Ogura, and Ms. Kunisuke Uehara for their irreplaceable guidance.

I would like to express the appreciation to members and alumni of Nishikawa Laboratory, Associate Professor Hiroaki Tatsumi, Dr. Yu-An Shen, Dr. Siliang He, Dr. Sanghun Jin, Mr. Jin Zhi, Mr. Fupeng Huo, Mr. Jiahui Li, Mr. Byungho Park, Ms. Aiko Yonezawa, Ms. Sachiko Sakata, Mr. Ichizo Sakamoto, Mr. Takuya Naoe, and other lab' members for their helpful advice and support on my research. Thanks, are also extended to all my friends in DG Company and colleagues in my department for all their helps and supports during my stay at Osaka. Special thanks to my friends in CF foundation for their warm encouragement and invaluable friendship.

I would like to thank my parents, my grandfather, my father-in-law, mother-in-law, my sibling, my brothers & sister-in-law for their continuous encouragement and support all the time. In particular, I would like to express my special thanks to my gentle wife and two daughters for their efforts and hardships during my time away from home. I love you so much. Without them, I would not pursue my dream. Thank you very much.

Finally, I would like to thank the Japanese government scholarship (Monbukagakusho: MEXT) for the financial support during my PhD course.

HAN LE DUY